

Time Resolved and Time Integrated VUV LIBS for the Detection of Carbon in Steel

A thesis submitted for the degree of
Doctor of Philosophy

Dublin City University (DCU)

University of Padova (UNIPD)

**School of Physical Sciences
National Centre for Plasma Science and
Technology (NCPST)**

Department of Information Engineering



Syedah Sadaf Zehra

B.Sc., M.Sc.

Supervisors

Prof. John. T Costello

Prof. Piergiorgio Nicolosi

Dr. Patrick Hayden

January 10, 2022

Time Resolved and Time Integrated VUV LIBS for the Detection of Carbon in Steel

Thesis presented by
Syedah Sadaf Zehra
B.Sc., M.Sc.

(Promoter)
Prof. John Costello

(Co-Promoter)
Prof. Piergiorgio Nicolosi

(Co-Promoter)
Dr Patrick Hayden

Doctoral studies Panel Membership:
Prof. John Costello
Prof. Piergiorgio Nicolosi
Dr. Patrick Hayden



Declaration of Authorship

I hereby certify that this material, which I now submit for assessment on the programme of study leading to the award of Doctor of Philosophy is entirely my own work, that I have exercised reasonable care to ensure that the work is original and does not to the best of my knowledge breach any law of copyright, and has not been taken from the work of others save and to the extent that such work has been cited and acknowledged within the text of my work.

Signed:  _____

Date: 10-01-2022 _____

ID No: 15210052 _____

Acknowledgments

Firstly, I would like to thank my supervisor Prof. John Costello for his continuous support and encouragement over the years. Without his guidance the completion of this work would not have been possible. I would also like to thank Prof. Piergiorgio Nicolosi for help and support during my mobility. I am also grateful to Dr Paddy Hayden for all his help during all my studies.

Thanks to the EXTATIC program secretary Irene and school secretary Lisa for taking care of paperwork associated with my studies and also Ray Murphy, Des Lavelle, and Alan Hughes for IT and technical support. Thanks to the entire staff and faculty of the School of Physical Sciences and the NCPST.

I am also thankful to all my group fellows in the NCPST, Steve, Ben, Nicky, Ares, Hu Lu and Muhammad for their help and support throughout this period of PhD. I would also like to say thanks to my best friend Inam for his care, help and support during the difficult times.

Finally, I would like to say special thanks to my family. First to my mom for her motivation in tough times and my dad for his continuous support since my childhood, without his help I would be unable to reach this point in my life. My loving friend and sister Saima for her love and care. Special thanks to my brother and my childhood friend Ahson for always being very supportive. I am also thankful to my brother Ali. At last, I would like to pay my special thanks to Afie for all his help, love and care that keeps me motivated in tough times.

To my Family (especially Afie)

List of Figures	10
List of Tables.....	17
List of Abbreviations.....	19
Abstract	20
Chapter 1 – Introduction, Motivation and Thesis Structure	21
1.1 LIBS in Brief.....	22
1.2 Motivation	26
1.3 Literature Review	28
1.3.1 History of LIBS.....	28
1.3.2 Recent Studies on LIBS	30
1.3.3 Progress in LIBS for Steel Analysis	32
1.4 Thesis Organization.....	34
References	36
Chapter 2 – Theoretical Background	41
2.1 Plasma Definition	41
2.2 Laser Produced Plasma Formation.....	44
2.2.1 Laser-Matter Interaction	46
2.2.2 Laser-Plasma Interaction	48
2.2.3 Plasma Expansion	49
2.3 Atomic Processes in Laser Induced Plasmas	50
2.3.1 Bound-Bound Processes	51
2.3.2 Free Bound Processes	53
2.3.3 Free-Free Processes	55
2.4 Equilibrium in Plasmas	57
2.4.1 Local Thermal Equilibrium.....	58
2.4.2 Coronal Equilibrium (CE).....	59
2.4.3 Collisional Radiative Equilibrium (CRE).....	59
2.5 Quantitative Spectroscopy Using Laser Plasmas	60
2.5.1 Number Density of the Species Under Analysis.....	61
2.5.2 Line Intensity and Transition Probability for Optically Thin Plasmas	61
2.5.3 Spectral Line Intensities – Radiative Transfer.....	63
2.5.4 Analytical Calibration Function and Curve:	65
2.5.5 Emission from Steel Plasmas in the VUV Spectroscopy.....	66

2.6	Analytical Figures of Merit	66
	Summary	68
	References	70
Chapter 3 – Experimental System Overview		72
3.1	Introduction	72
3.2	Laser System	74
3.2.1.	Brief Description of Continuum Surelite III-10 Laser System.....	74
3.2.2	Nd: YAG Laser Fundamentals.	75
3.2.3.	Continuum Surelite III-10 Optical Layout and Operation.....	77
3.2.4.	Synchronisation of the Continuum Surelite III-10 Laser with the Andor (DV420-BN) CCD Camera.....	79
3.3	Vacuum System and Target Chamber	81
3.3.1	Vacuum Pumps	81
3.3.2	Target Chamber and Targets.....	81
3.3.3	Glass Capillary Array (GCA)	84
3.4	Spectrometer.....	85
3.4.1	VM521 1m Normal Incidence Spectrometer	86
3.5	Signal Detection and Recording System	89
3.5.1	Time Integrated Detector	89
3.5.2	Time Resolved Detector	93
	Summary	96
	References	97
Chapter 4 – Limit of Detection (LoD) Optimization for Carbon in Steel: Point Plasma LIBS		99
4.1	Introduction	99
4.2	Space Resolved VUV LIBS - Principle	100
4.3	Choice of Laser Pulse Energy	104
4.4	Time Integrated Space Resolved VUV LIBS System.....	106
4.2.1	Time Integrated VUV LIBS (Target 2 mm from the Optic axis of the Spectrometer)	111
4.2.2	Time Integrated VUV LIBS (Target 4 mm from the Optic axis of the Spectrometer)	115
4.5	Time Resolved VUV LIBS	118
4.6	Calibration Curves from TI-SR and Time Resolved Spectra.....	124

4.4.1 Time Integrated Space Resolved (TISR) LIBS Calibration Curves	124
4.4.2 Time Resolved (TR) VUV LIBS - Calibration Curves	126
4.7 Limit of Detection Determination	128
Summary	132
References	134
Chapter 5 – Limit of Detection (LoD) Optimization for Carbon in Steel: Line Plasma LIBS	136
5.1 Introduction	136
5.2 Effect of Laser Focus and Target Position	137
5.3 TI-SR VUV LIBS Spectra for Optimum SBR	153
5.4 Calibration Curve	158
5.5 Limit of Detection (LoD) and Limit of Quantification (LoQ)	159
Summary	161
References	163
Chapter 6 – Conclusions and Future Work	165
6.1 Introduction	165
6.2 Summary and Conclusions	165
6.3 Future Work	169
References	171
Appendices	172
Appendix A	172
LIBS Application for Thin Metallic Films	172
A1. Introduction	172
A2. Experimental Procedure	173
A3. Laser Ablation at Low Power Density	175
A4. Laser Ablation at a High-Power Density	178
A5 Depth Profiling	181
A5.1 Crater Analysis using Optical Microscopy	181
A5.2 Crater Analysis Using a Light Tight Test	182
Summary	183
References	183
Appendix B	184
Multivariate Analysis of UV LIBS Spectra of Scrap Metals and Non-Metals	184
B1. Introduction	184

B2. Experimental Procedure	185
B 2.1 Quantel ‘Brilliant b’ Laser	186
B2.2 Spectrometer and Detector	187
B2.3 Samples	187
B3. Methodology	188
B4. LIBS Analysis of Different Materials	191
B4.1 UV-Vis Spectra for Metallic and Semiconducting Samples.....	191
Carbon	192
Tantalum.....	193
Silicon.....	193
Silicon Carbide (SiC)	194
Lead (Pb)	194
Molybdenum	195
Silver (Ag).....	195
Zinc (Zn)	196
Tungsten (W).....	196
B 5. Classification of Metals and Semiconductors using Multivariate Analysis.	197
B 5.1 Principal Component Analysis Applied to Scrap Metal Spectra	197
B.5.2 Principal Component Analysis for the Identification of Elements	200
Summary	203
References:	204
Appendix C	204
List of Publications and Research Outputs	204

List of Figures

Figure 2. 1 Laser produced plasma formation and expansion <i>in vacuo</i> , illustrating the different evolutionary stages from the plasma formation to late phase plume condensation which can yield clusters for materials growth.	45
Figure 2. 2 Schematic of electron impact collisional excitation and de-excitation occurring in a laser produced plasma where the upper bound state has energy E_2 and lower bound state has energy E_1	52
Figure 2. 3 Pure radiative processes, namely photoabsorption and photoemission of line radiation arising from bound to bound transitions	53
Figure 2. 4 Bound-free processes taking place within a laser produced plasma. (a) The left hand side figure represents the electron collisional processes (impact ionization and 3-body recombination). a) Shows the radiative processes of photoionization and radiative recombination. The blue dots represent the ionizing and recombining electrons in each panel.	54
Figure 2. 5 Bremsstrahlung and inverse-bremsstrahlung taking place within the produced plasma. The upper and lower continuum states are designated ϵ and ϵ' , with $\epsilon > \epsilon'$. E_1 and E_2 refer to two typical bound states of the atom or ion.	56
Figure 2. 6 Criteria for the validity of different thermodynamic equilibrium models as a function of electron temperature and density [15] .The critical density for CO ₂ and Nd:YAG laser produced plasmas is also marked by the horizontal lines.	57
Figure 2. 7 Transition probabilities in a two-level energy system (E_i and E_k) where $E_i < E_k$ with a population density of n_i and n_k respectively.	62
Figure 3. 1 Schematic diagram showing the VUV LIBS set up for the time integrated spectroscopy of point and line plasmas.	73
Figure 3. 2 Schematic diagram showing the time resolved VUV LIBS monochromator set up. The CCD detector is replaced by time resolved detector.	74

Figure 3. 3 Simplified energy level scheme for a 4 level laser system.	76
Figure 3. 4 Schematic diagram of the Q switched Surelite Nd YAG laser system.	78
Figure 3. 5 Schematic diagram for the synchronization of the laser system and CCD.	80
Figure 3. 6 Target chamber along with its associated vacuum and optical components.	82
Figure 3. 7 A Glass capillary array (GCA) with 5 micron diameter pores [10].	85
Figure 3. 8 Top view(a) and side view (b) of the spectrometer and target chamber.	86
Figure 3. 9 Illustration of the Rowland circle showing entrance and exit slit locations along with the grating.	87
Figure 3. 10 Schematic of a MOS capacitor structure.	89
Figure 3. 11 Basic design of a CCD chip [9].	90
Figure 3. 12 a) Schematic diagram of time resolved detector, showing the plastic scintillator and photomultiplier tube, b) scintillation process combined with the light detection by photomultiplier tube [16].	93
Figure 3. 13 The fluorescence spectrum of the EJ-212 scintillator [17].	94
Figure 3. 14 Side view of the Hamamatsu PMT model number R1450 [19].	95
 Figure 4. 1 Schematic of the TISR principle and observing position of plasma 's' (b) emission signal recorded at 2 mm (c) and 4mm target distance from the optic axis [1,7].	101
Figure 4. 2 (a) Variation in the 97.7 nm line intensity with $\frac{1}{2}$ -wave plate angular setting. (b) Variation in the laser pulse energy with $\frac{1}{2}$ -wave plate angular setting. The pulse energy was controlled by the combination of a $\frac{1}{2}$ -wave plate and polariser, the latter set orthogonal to the laser polarisation direction. (c) Examples of C-Steel spectra taken for different pulse energies.	105
Figure 4. 3 Spectrum obtained with CCD in full vertical binned (FVB) mode.	108

Figure 4. 4 Part of the spectrum in figure 4.3 following pixel to wavelength conversion. ... 108

Figure 4. 5 Spectrum obtained with a pure graphite target containing a distance of 2 mm from the spectrometer optic axis. Red (vertical) bars – the 11 pixels integrated around the C III $1s^2 2s 2p$ (1P_1) to $1s^2 2s^2$ (1S_0) line at 97.7 nm. Black (vertical bars)– the background was obtained by integrating 11 pixel values around 104.4 nm. 112

Figure 4. 6 Spectrum obtained for the reference C/Fe target (IARM 268 B) with a carbon concentration of 870 ppm placed located 2 mm from the spectrometer optic axis. Red bars – the 11 pixels integrated around the C III $1s^2 2s 2p$ (1P_1) to $1s^2 2s^2$ (1S_0) line at 97.7 nm. Black bars – the background was obtained by integrating 11 pixel values around 104.4 nm. 113

Figure 4. 7 Spectrum obtained for the reference C/Fe target (1522 BS 2932) with a carbon concentration of 2080 ppm located 2 mm from the spectrometer optic axis. Red bars – the 11 pixels integrated around the C III $1s^2 2s 2p$ (1P_1) to $1s^2 2s^2$ (1S_0) line at 97.7 nm. Black bars – the background was obtained by integrating 11 pixel values around 104.4 nm. 113

Figure 4. 8 Spectrum obtained for the reference C/Fe target (12 M BS XCCV) with a carbon concentration 4400 ppm located 2 mm distance from the spectrometer optic axis. Red bars – the 11 pixels integrated around the C III $1s^2 2s 2p$ (1P_1) to $1s^2 2s^2$ (1S_0) line at 97.7 nm. Black bars – the background was obtained by integrating 11 pixel values around 104.4 nm. 114

Figure 4. 9 Spectrum obtained for the reference C/Fe target (CRM 12 A 215/3) with a carbon concentration of 9100 ppm located 2 mm from the spectrometer optic axis. Red bars – the 11 pixels integrated around the C III $1s^2 2s 2p$ (1P_1) to $1s^2 2s^2$ (1S_0) line at 97.7 nm. Black bars – the background was obtained by integrating 11 pixel values around 104.4 nm at 2 mm. 114

Figure 4. 10 Spectrum obtained for the reference C/Fe target (IARM 268 B) with a carbon concentration of 870 ppm at 4 mm distance from the spectrometer optic axis. Red bars – the 11 pixels integrated around the C III $1s^2 2s 2p$ (1P_1) to $1s^2 2s^2$ (1S_0) line at 97.7 nm. Black bars – the background was obtained by integrating 11 pixel values around 104.4 nm. 116

Figure 4. 11 Spectrum obtained for the reference C/Fe target (1522 BS 2932) with a carbon concentration of 2080 ppm located 4 mm from the spectrometer optic axis. Red bars – the 11 pixels integrated around the C III $1s^2 2s 2p$ (1P_1) to $1s^2 2s^2$ (1S_0) line at 97.7 nm. Black bars – the background was obtained by integrating 11 pixel values around 104.4 nm. 116

Figure 4. 12 Spectrum obtained for the reference C/Fe target (12 M BS XCCV) with a carbon concentration of 4400 ppm at 4 mm distance from the spectrometer optic axis. Red bars – the 11 pixels integrated around the C III $1s^22s2p$ (1P_1) to $1s^22s^2$ (1S_0) line at 97.7 nm. Black bars – the background was obtained by integrating 11 pixel values around 104.4 nm. 117

Figure 4. 13 Spectrum obtained for the reference C/Fe target (CRM 12 A 215/3) with a carbon concentration of 9100 ppm at 4 mm distance from the spectrometer optic axis. Red bars – the 11 pixels integrated around the C III $1s^22s2p$ (1P_1) to $1s^22s^2$ (1S_0) line at 97.7 nm. Black bars – the background was obtained by integrating 11 pixel values around 104.4 nm. 117

Figure 4. 14 Time resolved plasma emission at 97.7 nm for the steel target with a carbon concentration of 870 ppm located 2mm from the monochromator optic axis. 120

Figure 4. 15 Time resolved plasma emission at 97.7 nm for the target with a carbon concentration 2080 ppm. 121

Figure 4. 16 Time resolved plasma emission for the target with a carbon concentration of 4400 ppm. 121

Figure 4. 17 Time resolved plasma emission at 97.7 nm for the steel target with a carbon concentration of 9100 ppm. 122

Figure 4. 18 (a-d) shows the time resolved continuum emission signal for a target with a carbon concentration of 870, 2800, 4400, 9100 ppm (respectively) obtained at a monochromator wavelength of 104.4 nm. 122

Figure 4. 19 Integral of the line and continuum signals for targets with carbon concentrations of (a) 870 ppm, (b) 2080 ppm, (c) 4400 ppm and (d) 9100 ppm. 123

Figure 4. 20 Time integrated VUV LIBS calibration curve for spectra recorded with the target located 2 mm from spectrometer optic axis. 125

Figure 4. 21 Time integrated VUV LIBS calibration curve for spectra recorded with the target 4 mm from spectrometer optic axis. 126

Figure 4. 22 Time resolved VUV LIBS calibration curve for spectra recorded with the target located 2 mm from spectrometer optic axis. 127

Figure 5. 1 TISR LIBS setup with plano-convex cylindrical lens (focusing in the vertical direction).....	138
Figure 5. 2 TI-SR VUV LIBS spectra for different locations of the target surface relative to the optic axis of the spectrometer. The C(III) line at 97.7 nm occupies the pixel range from 467 to 475 while the pixel range 637 to 645 was chosen to estimate the background intensity. The cylindrical lens was defocused by 5 mm (above the target).	140
Figure 5. 3 TI-SR VUV LIBS spectra for different locations of the target surface relative to the optic axis of the spectrometer. The C(III) line at 97.7 nm occupies the pixel range from 467 to 475 while the pixel range 637 to 645 was chosen to estimate the background intensity. The cylindrical lens was defocused by 10 mm (above the target).	141
Figure 5. 4 TI-SR VUV LIBS spectra for different locations of the target surface relative to the optic axis of the spectrometer. The C(III) line at 97.7 nm occupies the pixel range from 467 to 475 while the pixel range 637 to 645 was chosen to estimate the background intensity. The cylindrical lens was defocused by 20 mm (above the target).	141
Figure 5. 5 TI-SR VUV LIBS spectra for a displacement of the target surface, relative to the optic axis of the spectrometer, of 8.5 mm. The C(III) line at 97.7 nm occupies the pixel range from 467 to 475 while the pixel range 637 to 645 was chosen to estimate the background intensity. The cylindrical lens focus was varied from 16.5 mm to 20.5 mm in increments of 0.5 mm (above the target).	142
Figure 5. 6 Intensity of the background (at ca. 104.4 nm) obtained at four different target positions ranging from 8.0 to 9.5 mm and lens positions ranging from 5 mm to 25 mm.....	143
Figure 5. 7 Intensity of the 97.7 nm line obtained at four different target positions ranging from 8.0 mm to 9.5 mm and lens positions from 5 mm to 25 mm.	145
Figure 5. 8 Background subtracted, peak intensity of the 97.7 nm line at four different target positions ranging from 8.0 mm to 9.5 mm and lens positions from 5.0 mm to 25 mm.....	145

Figure 5. 9 Standard deviation of the background intensity (at ca. 104.4 nm) obtained at four different target positions ranging from 8.0 to 9.5 mm and lens positions from 5 mm to 25 mm.	147
Figure 5. 10 Line (97.7 nm) and background intensities obtained at four different target positions ranging from 8.0 mm to 9.5 mm. The lens position was fixed at 16.5 mm. Using the raw data shown in panel (a), the signal to background ratio (SBR) and standard deviation of the background (SBR) at ca. 104.4 nm are obtained and shown in panel (b).	150
Figure 5. 11 Line (97.7 nm) and background (ca. 104.4 nm) intensities obtained at lens positions ranging from 5.0 mm to 25 mm when lens was fixed at 8.5 mm. (a) Using the raw data show in panel, (b) the signal to background ratio (SBR) and standard deviation of the background (SDB) are obtained and shown in panel.	152
Figure 5. 12 Spectrum obtained with the reference target CRM Fe 1/1 (carbon concentration of 50 ppm). Red bars – the 11 pixels integrated around the C III $1s^22s2p$ (1P_1) to $1s^22s^2$ (1S_0) line at 97.7 nm. Black bars – the background was obtained by integrating 11 pixel values around 104.4 nm.	154
Figure 5. 13 Spectrum obtained with the reference target 11 CM 5078 (carbon concentration of 180 ppm). Red bars – the 11 pixels integrated around the C III $1s^22s2p$ (1P_1) to $1s^22s^2$ (1S_0) line at 97.7 nm. Black bars – the background was obtained by integrating 11 pixel values around 104.4 nm.	155
Figure 5. 14 Spectrum obtained with the reference target 1008 BS XAAS (carbon concentration of 410 ppm). Red bars – the 11 pixels integrated around the C III $1s^22s2p$ (1P_1) to $1s^22s^2$ (1S_0) line at 97.7 nm. Black bars – the background was obtained by integrating 11 pixel values around 104.4 nm.	155
Figure 5. 15 Spectrum obtained with the reference target CRM 12 B 1767 (carbon concentration of 520 ppm). Red bars – the 11 pixels integrated around the C III $1s^22s2p$ (1P_1) to $1s^22s^2$ (1S_0) line at 97.7 nm. Black bars – the background was obtained by integrating 11 pixel values around 104.4 nm.	156
Figure 5. 16 Spectrum obtained with the target CRM 14 MI 206A (carbon concentration of 680 ppm). Red bars – the 11 pixels integrated around the C III $1s^22s2p$ (1P_1) to $1s^22s^2$ (1S_0)	

line at 97.7 nm. Black bars – the background was obtained by integrating 11 pixel values around 104.4 nm. 156

Figure 5. 17 Spectrum obtained with the target CRM 12 X 15252P with a carbon concentration of 940 ppm. Red bars – the 11 pixels integrated around the C III $1s^22s2p$ (1P_1) to $1s^22s^2$ (1S_0) line at 97.7 nm. Black bars – the background was obtained by integrating 11-pixel values around 104.4 nm. 157

Figure 5. 18 Carbon in steel intensity calibration curve. Six different samples with carbon concentrations of 50 ppm to 940 ppm (cf. Table 5.1) were used to construct the curve. 158

List of Tables

Table 1. 1 Comparison of topics selected for talks at a number of EMS LIBS conferences covering the period from 2008 to 2019.....	30
Table 2. 1 Primary atomic processes that occur within a laser produced plasma where B refers to bound, and F refers to free, electron processes.....	51
Table 3. 1 Specifications of the Continuum Surelite III-10 Q-switched laser system.....	75
Table 3. 2 Concentration of carbon in the various samples used.....	84
Table 3. 3 Specifications of the GCA used for VUV LIBS.....	85
Table 4. 1 Carbon and iron lines, wavelength, configuration and transition probability	109
Table 4. 2 Line intensity values for the different steel samples with concentrations of 870 ppm to 9100 ppm – target located 2 mm from the optic axis	115
Table 4. 3 Line intensity values for the different steel samples with concentrations of 870 ppm to 9100 ppm – target located 4 mm from the optic axis	118
Table 4. 4 Line intensity values for the different steel samples with concentrations of 870 ppm to 9100 ppm – target located 2 mm from the optic axis	127
Table 4. 5 Comparison of the analytical quality of three VUV LIBS methods used for carbon in steel	129
Table 4. 6 Comparison of time resolved system with respect to time integrated LIBS system	130
Table 4. 7 Comparison of limit of detection with the literature.....	132

Table 5. 1 Steel samples and the respective carbon concentrations	139
Table 5. 2 Parameter for experiments on calibration curves and limit-of-detection for C in steel	153
Table 5. 3 CIII 97.7 nm line intensity (background subtracted), and signal to background ratio (SBR) obtained from different samples of steel having different carbon concentrations.....	157
Table 5. 4 LoD improvement for line plasma-based VUV LIBS over point plasma-based VUV LIBS	160
Table 5. 5 Comparison of limit of detection with the literature	161
Table 6. 1 Comparison of limit of detection and signal to background ratio of TISR (point plasma, line plasma) and TR (point plasma) for VUV LIBS	167

List of Abbreviations

VUV	Vacuum Ultraviolet, page 1
LIBS	Laser Induced Breakdown Spectroscopy, page 1
UV-Vis	Ultraviolet Visible, page 17
LoD	Limit of detection, page 17
TISR	Time Integrated Space Resolved, page 17
TR	Time Resolved, page 17
CCD	Charged- Coupled Device, page 17
PCA	Principal Component Analysis, page 17
LoQ	Limit of Quantification, page 17
Nd:YAG	Neodymium-Doped Yttrium Aluminium Garnet, page 23
B-B	Bound-Bound, page 51
B-F	Bound- Free, page 51
F-F	Free-Free, page 51
CTE	Complete Thermodynamic Equilibrium, page 56
LTE	Local Thermal Equilibrium, page 58
CE	Coronal Equilibrium, page 58
CRE	Collisional Radiative Equilibrium, page 58
FWHM	Full Width at Half Maximum, page 74
PC	Pockel Cell, page 76
KDP	Potassium Diphosphate, page 78
NIST	National Institute of Standards and Technology, page 105
CMOS	Complementary Metal-Oxide- Semiconductor, page 89
PMT	Photomultiplier Tube, page 91
GCA	Glass Capillary Array, page 73
SBR	Signal to Background Ratio, page 21

Abstract

Laser Induced Breakdown Spectroscopy (LIBS) is an analytical technique used to classify and potentially quantify elements in complex hosts (or matrices). Vacuum Ultraviolet Laser Induced Breakdown Spectroscopy (VUV LIBS) offers measurable improvements over traditional visible region LIBS, due to the presence of strong resonance and well spectrally isolated transitions at these shorter wavelengths. This extends the ability of LIBS to discriminate between emission lines from different elements, particularly light elements such as carbon, nitrogen, oxygen, sulphur, etc. In addition, as with visible LIBS, the precision obtainable can be limited by the continuum emission at the early stage of the plasma lifetime and greater performance can be achieved by moving to a time resolved detection system, reducing the contribution from the continuum. Hence, a (single channel) time resolved VUV LIBS system has been designed by replacing a back illuminated CCD with a combination of a plastic scintillator and a photomultiplier tube on an existing LIBS system. In this research, the performance of time integrated and time resolved VUV LIBS for the determination of the carbon content in steel samples is compared. The results demonstrated an improved limit of detection (LOD) for time resolved VUV LIBS over time integrated VUV LIBS for traditional point plasmas.

In addition, VUV emission from plasma plumes created at a line (laser) focus was also studied for the same steel samples and the limit of detection was optimised and compared the limit for conventional point plasmas. The results demonstrate that the line focused plasma source in multichannel time integrated space resolved (TISR) mode and the single channel time resolved VUV mode yield comparable LoD values of 50 and 56 ppm respectively. It also showed that both were significantly better than TISR VUV LIBS with point plasma VUV sources which exhibited a poorer LoD of 316 ppm.

In addition, two ultraviolet-visible (UV-Vis) LIBS studies were carried out in University of Padova. One of these focused on exploring the potential of conventional LIBS for depth profiling of thin films. The other focused on the classification and sorting of scrap metal samples using multivariate analysis, in particular using principal component analysis (PCA).

Chapter 1 – Introduction, Motivation and Thesis Structure

Since the early days of laser plasma spectroscopy, it became clear that the technique could be useful for the identification, and perhaps even quantification, of the elemental composition of matter in all of its phases, solid, liquid and gas [1]. Very quickly the domain of LIBS or Laser Induced Breakdown Spectroscopy was born [2], and it has undergone continuous development over the past three to four decades, focused mainly on the ultraviolet (UV), visible (Vis) and near infrared (NIR) portions of the electromagnetic spectrum. The impetus for UV-Vis-NIR LIBS comes from its relative simplicity of implementation [3] and the large volume of spectroscopic data available [4]. In recent years, new developments in multi-pulse LIBS [5], compact hand-held systems [5, 6] and improved detection [6,7] have received significant focus. What has not developed at the same rate is LIBS outside the UV-Vis-NIR spectral range. There are a few reports [8,9,10] focused on the vacuum-UV spectral range, despite some key advantages, especially the access to strong emission lines (resonant, connected to the ion ground state) and concomitant signal-to-background ratio (SBR) improvements. Of course, remote/field-based LIBS is not possible due to high vacuum requirements, however for materials that can be analysed in laboratory environments the case for VUV LIBS appears to be strong. In order to demonstrate the unique high precision material characterisation capabilities of LIBS in the VUV range, one focus of the Dublin City University (DCU) laser plasma group has been the detection and quantification of light elements in steel, mainly carbon, sulphur and phosphorous using its inhouse VUV Laser Induced Breakdown Spectroscopy (LIBS) system [11,12]. However, to date, the main emphasis has been on point-like plasmas using the time integrated LIBS system for the determination of limit-of-detection

(LoD) of trace elements like C, S, and P [11,12]. As noted in the literature, for the first time (to my knowledge), this doctoral thesis investigated time resolved VUV LIBS measurements in focus on the optimization of the limit of detection for carbon contents in steel in vacuum. Separately, in order to determine its efficacy in the domain of VUV-LIBS, the combination of a laser plasma formed at the focus of a cylindrical lens with the existing time integrated (TI) VUV LIBS detection system was studied, with the aim of obtaining a further improvement of the limit-of-detection (LoD) for carbon in steel.

Separately an application of LIBS was also investigated to initial exploration, namely the measurement of the laser ablation rate of thin aluminium films on solid substrates during depth profiling, as the laser drilled down through the film and onto the substrate. Also, UV-Vis-NIR LIBS combined with multivariate data analysis was explored for its potential in the recycling of the waste materials including metals and semiconductors, work performed at the Institute of Photonics and Nanotechnology (IFN) and the University of Padua (Università degli Studi di Padova - UniPD).

In what follows a brief introduction to LIBS, the motivation behind this work, and a literature review, based on the history of LIBS, is given. The organization of thesis, based on the aims of the research, is also briefly presented in this chapter.

1.1 LIBS in Brief

Laser Induced Breakdown Spectroscopy (LIBS) is an analytical technique used to classify and potentially quantify chemical elements in complex hosts or matrices [13,14]. A high-power laser is used to ablate the surface of the sample forming a plasma plume of ions, atoms and potentially molecules, molecular ions and clusters, above the surface of the sample depending on the laser fluence and ablated (plasma) plume conditions [13,14]. The threshold value of laser ablation for a solid target generally lies between 10^8 W/cm^2 to 10^{10} W/cm^2 [14,15]. During

the earliest phases of the pulsed laser interaction with the target surface, and at sufficiently high intensity, some seed electrons are produced due to photoionization (including multiphoton ionization) along with a range of possible laser assisted photoabsorption/photoionization processes. The result is a weakly ionized plasma formed very early on, typically within less than 100 ps. These seed electrons absorb laser radiation by the process of inverse Bremsstrahlung (IB) which increases their kinetic energy. The increased energy means that they can cause further ionization via collisions with the target surface and/or the plasma plume as it grows and increases in density. The process is regenerative in the sense that the higher the electron density the greater the IB rate and vice versa, which results in avalanche ionization. Gradually the plasma becomes opaque to the laser pulse and the target surface is protected from the laser radiation. The plasma density at which the plasma becomes opaque to the incoming laser light is termed the critical density (n_{ec}) and can be calculated using the following equation [14]:

$$n_{ec} = \frac{m_e \omega^2}{4\pi e^2} \cong \left(\frac{10^{21}}{\lambda^2} \right) / \text{cm}^3 \quad \text{eq. (1.1)}$$

where m_e is the electron mass, ω represents the frequency of the laser radiation, e is the electron charge and λ is the laser wavelength, measured in μm .

The value of plasma critical density for Nd:YAG laser radiation with a fundamental wavelength of 1064 nm is approximately 10^{21} cm^{-3} . After reaching the critical value of the plasma density, the major portion of incident laser energy is reflected by the plasma and at this stage the plasma starts to expand. As it expands, the plasma density decreases, thus the plasma frequency decreases and once again the laser radiation is able to reach the target surface where it causes further ionization, as well as further ionizing the plume as it passes through it, on its way to the target. This cyclical process continues until the termination of the laser pulse.

Collisions between energetic free electrons and atoms (or ions) within the plasma cause bound electrons to move to higher energy states, both bound and free, in these species. For excited bound states, when the corresponding electrons decay to lower energy states, discrete line radiations are emitted. The wavelength of these emission lines depends on the difference in energy between the initial and final electronic states of the transitions concerned ($\lambda = hc/E_f - E_i$). The intensity of an emission line in turn depends on the dipole matrix element connecting the initial $|i\rangle$ and final $|f\rangle$ states, i.e., $\langle i|r|f\rangle$, where r is the dipole operator. The emitted radiation is dispersed by a spectrometer, detected and displayed in the form of an intensity versus wavelength spectrum. Each ionized element emits a characteristic spectrum which acts as the ‘elemental fingerprint’ by which it can be identified. In principle each element can be represented by a particular, usually well isolated, emission line (from a corresponding atom or ion in the plasma) and the line intensity can be related to the concentration of that element within the original target sample. On that basis the elemental characterization of a target sample, at least at the level of the identification of the elements present, and in some cases, their concentration, becomes possible.

However, the possibility that spectral lines from different trace elements overlap with each other and/or with lines emitted by the host matrix exists. This is especially the case in the visible spectral region which can have a very high density of close lying lines from both the elements of interest and the matrix, e.g., elements like C, N, etc. in a steel host matrix [1,9]. The supernumerary lines arise from the multitude of possible transitions between excited states of atoms, ions and possibly even molecules or molecular ions present in the hot plasma plume. In contrast, the VUV spectral range tends to be less cluttered as usually it is only resonance transitions in neutral and lowly ionized atoms that give rise to strong emission lines in this region [16]. Also, as the lines that are connected to the ground state, they tend to be more intense than those arising from transitions between excited states in ions that typically appear

in the UV and visible regions of the spectrum. Hence VUV LIBS can offer potential improvements over traditional LIBS in the visible region, due to the abundance of well separated resonance transitions at these shorter wavelengths [17]. This extends the ability to discriminate between the spectral distribution of the emission from different elements, particularly light elements such as lithium, beryllium, carbon, sulphur, etc.

The early phase of a laser produced plasma usually contains a strong continuum emission component, which is caused mainly by ion-electron radiative recombination and bremsstrahlung [13]. Therefore, early plasma continuum emission will overlap and interfere with the useful line emission. Methods which decrease the continuum's effect on the line emission will thus lead to an improvement in the limit-of-detection (LoD) for LIBS. Fortunately, the continuum emission has a shorter lifetime in comparison with emission from excited ionic and neutral species. By eliminating the early emission, it is possible to reduce the contribution from the continuum and focus on useful line dominated radiation from later stages in the plasma lifetime [11]. In LIBS this is usually achieved by utilising the gating controls on the ICCD camera image intensifier. Combined with a delay/gate generator the exposure time (gate width) and time delay can be set so that a so-called 'gate-delay' is introduced in which the opening of the 'camera shutter' happens at a predetermined time after plasma ignition. This is usually some hundreds of nanoseconds after the laser pulse arrives on target. The exposure time is set by the gate width (opening time for the shutter) and is usually set in the range of hundreds of nanoseconds to a few microseconds. This control is achieved, in practice, by modulating the bias voltage applied to the microchannel plate intensifier of the ICCD camera [17].

1.2 Motivation

Steel, the material focused on in this thesis, is widely used in different industries such as construction, transport, aerospace, automobiles, machinery and tooling, healthcare, domestic appliances and electrical equipment [18]. There are various steel alloys developed on the basis of the presence of different metallic and non-metallic elements which include C, Cr, Mn, Mo, Ni, Si, Sn, Ti and V [19]. These variants are used in industry for their specific properties, e.g., light elements including carbon, sulphur, phosphorous and nitrogen play an important role in achieving specific mechanical and physical properties in different types of steel. The concentration of these trace elements should not exceed a certain level (up to a few parts per million (ppm)) in order to retain the unique characteristics of steel for specific applications such as construction [19], automotive [20] and aerospace [21].

The accurate determination of the amount of trace elements in steel alloys is one of the challenges faced by the metals industry. It is difficult to detect light elements in steel using LIBS in the UV, NIR, and VIS regions due to its poor performance for trace elements in these spectral regions. This limitation is mainly due to the richness of Fe plasma spectra leading to blending of emission lines from the trace elements of interest with Fe lines. In order to address this challenge, specially designed VUV LIBS systems have been, and are being, developed and used to determine the concentrations of trace elements. In comparison to many of the conventional spectroscopic techniques such as spark discharge optical emission spectroscopy (SD-OES), X-ray fluorescence (XRF), atomic absorption spectroscopy (AAS) and laser ablation inductively coupled plasma optical emission spectroscopy (LA-ICP-OES), LIBS has many advantages including no or minimum sample preparation, it is almost non-destructive, the use of optical energy for the excitation of the sample (avoiding ionisation radiation) and the capability to characterize solid samples directly [16]. Moreover, it can be used remotely [22] and for in-situ applications which involve harsh and abrasive environments [23]. Among

all these techniques, SD-OES and XRF are considered to be the closest competitors to LIBS, especially SD-OES which is the standard method for steel analysis in industry due to its powerful performance in terms of limit of detection (LoD), particularly for trace elements [16]. However, SD-OES requires a series of long and arduous sample preparation steps for steel samples and cannot be used online. In order to achieve quality assurance while meeting the needs of process control as demanded by industry, the LIBS technique has been undergoing continuous development for some time. LIBS is being applied for the identification of metal alloys in industry, specifically steel for more than two decades. Different LIBS techniques are being explored for the optimization of limit-of-detection (LoD) for the steel industry along with various other techniques. However, continuous improvements in the quantification of light elements in metals, by means of LIBS, remains one of the challenges to significantly wider industry adoption [24], despite the many other technical and economic advantages that the technique could confer on the associated materials and manufacturing sectors.

In order to address this issue, a number of research groups working in the general area of laser induced plasma spectroscopy (LIPS) and LIBS, including at the NCPST (DCU), have worked on the determination, to include variously the identification, classification and quantification, of light elements in metals, specifically carbon, sulphur, phosphorus in steel [11,12,24,25]. These groups have focused on improving the limit-of-detection (LoD) by exploring variants on the basic LIBS technique. However, there remains room for improvement in the accuracy, dynamic range, and potentially other features related to the determination of the trace elements like carbon in steel.

In this doctoral thesis, VUV LIBS is explored using three different experimental setups, firstly, by using the already well explored time integrated, space resolved (TI-SR) experimental setup, using a point plasma VUV emitter, with which a number of studies have already been undertaken and reported in both single [11,12] and double pulse [12] modes. For the second

set of experiments, the existing setup was modified to operate in monochromator mode and the back illuminated CCD detector was replaced by a single channel scintillator to convert VUV photons to visible light. The visible light was delivered to a fast response photomultiplier tube to result in a single (wavelength) channel providing time resolution on a nanosecond timescale. Thirdly, ‘line plasma’ LIBS experiments were performed, in which plasmas were formed by focusing each laser pulse onto the steel surface using a cylindrical lens. The resulting line focus created a plasma plume. The line plasma was aligned vertically, along the same direction as the fore-slit and the entrance slit of the spectrometer. The limit of detection (LoD) for carbon in steel was determined for this configuration and compared with the LoD obtained using the more usual point focus to create the plasma plume.

UV-Vis LIBS was also explored in experiments at UniPD which were focused on potential applications in characterisation of thin film and sorting of scrap metals with assistance of advanced statistical tool, multivariate analysis. Firstly, depth profiling of thin films for different laser irradiance values was undertaken to explore the relationship between laser ablation rate and the depth of thin films with a view to applying LIBS for the combination of depth profiling (determination of thin film composition) with thickness measurements. At UniPD, UV-Vis LIBS was undertaken and combined with multivariate analysis of the spectral data for potential application to the recycling industry for different metals and semiconductors. Another application was the use of multivariate analysis of LIBS spectra in the scrap metal industry.

1.3 Literature Review

1.3.1 History of LIBS

Laser Induced Breakdown spectroscopy (LIBS) can trace its origins back to 1963, when the first spectrochemical analysis of surfaces was published by Debras-Guedon and Liodec [27].

LIBS experiments can be conducted on matter in all of its three stable states, namely solid, liquid and gas, which became one of the major reasons for the rapid and continuing development of corresponding instruments and methods to advance the technique over many decades [17]. In the early 1970s, as more advanced LIBS instruments began to become available, time resolved spectroscopic analysis of laser produced plasmas advanced significantly, allowing users to monitor the plasma formation and evolution which helped to discriminate the early phase continuum background from the line emission, thereby improving the line to background intensity ratio [2]. Innovative studies on spectral recording and imaging systems in those years are described by various groups including Schroeder et al [28] and Menzies et al.[29]. These studies largely focused on the different detection systems that were used to obtain temporally resolved spectra. With the development of new detectors, gated intensified charge coupled device (ICCD) cameras became the preferred method for time resolved LIBS measurements. In the 1980s, the lasers and other LIBS components became more compact and user friendly so that the in-situ advantages of LIBS became more evident, resulting in the growth of time resolved LIBS studies and broadening of the research field to encompass many different materials and sectors [29]. The most prominent studies regarding LIBS analysis during this period include physical and chemical matrix effects on elemental analysis [30], plasmas in water [31], spatio-temporal plasma evolution [32], LIBS on aerosols [33] and functional materials [34]. Advancement in the understanding of laser plasma fundamentals and techniques has enabled LIBS instruments to investigate more challenging topics such as detection of toxic dust in air and on filters [35] and hazardous gases [33].

From 1990-2000 there was a rapid development in fundamental studies as well as in applications. There was a continuous improvement in LIBS quantitative analysis [36,37]. Quantitative LIBS was optimised for aerosol analysis [38,39], ores [40,41], artworks [42] and also remote LIBS [43,44], amongst others. The development of remote LIBS started in the

1980s and grew rapidly in 1990s. Studies included remote elemental analysis [43] including the use of fibre optic probes in remote applications [44]. In the same era, the application of LIBS for planetary exploration began, which includes a series of key works by Knight et al. [45] and A.W Stroupe [46].

1.3.2 Recent Studies on LIBS

By exploring the development and advancement of LIBS since 2000 to the recent Euro Mediterranean Symposium of LIBS in 2019 (see table 1.1), it is evident that LIBS has gradually developed into a powerful and versatile analytical technique. Its maturity was marked by its usage in the Mission to Mars for planetary geology in 2009. Its technical expansion includes a number of developments including its extension to the VUV region of the spectrum, whereas in applications its usage has expanded to biological studies on human teeth, bones and tissues, surface mapping and imaging (scanning LIBS) [47,48] along with commercial instrumentation and customized advanced statistical techniques to increase the efficiency and reliability of LIBS analysis.

Table 1. 1 Comparison of topics selected for talks at a number of EMS LIBS conferences covering the period from 2008 to 2019

Year	2008	2010	2017	2019
Topics	Number of talks			
Fundamentals	14	5	19	11
Modelling and Calibration	5	7		7
Industrial Applications	6	6	12	25
Remote and Environmental	11	4	10	4
Culture and Heritage	3	2	2	
Instrumentation	4	4	5	5
Biomedical		3	8	4

Multivariate Analysis [49] turned out to be an important addition to traditional LIBS due to its ability to handle more than one statistical variable at a time. Multivariate analysis, a branch of chemometrics, has widened the analytical scope of LIBS, and has allowed it to be widely applied to the analysis of mineral ores, sea water, aerosols, biological and organic samples [50,51]. In order to further optimise LIBS, efforts have been made to modernise some traditional spectroscopy-based methods with the addition of up to date lasers, optics and spectrometers [52]. A greater emphasis on commercialization and the development of more compact and portable LIBS systems was a feature of the 2010 (and subsequent) conferences. Portable and hand-held LIBS is particularly attractive for deployment in security and forensics [53].

It is evident from the increasing number of contributions in more recent conferences, e.g., EMSLIBS 2019, that LIBS has turned into a robust technique with unique specifications and possesses a great diversity of applications along with continuing work on the underpinning fundamentals. Its growing acceptance and applications in the medical, clinical and pharmaceutical domains are testament to its maturity as an analytical technique. There has been a continuous improvement in the analytical capabilities of LIBS over the years, by combining LIBS with other new or developed techniques or by advancements in the analytical procedures. For example, LIBS-DLIFS (diode laser-induced fluorescence) and LIBS-DLAAS (diode laser atomic absorption spectroscopy) are relatively newly developed techniques. Maeng et. al developed LIBS with timed ablation to optimize detection efficiency [54]. From the LIBS timeline trend throughout its history, and observing the continuous development of LIBS, one can easily predict and foresee the future of LIBS as a powerful analytical tool for many areas.

1.3.3 Progress in LIBS for Steel Analysis

Strum et al. [55] used the time resolved LIBS technique for the elemental analysis of steel for the first time in 2000. For the first time a limit of detection below 10 $\mu\text{g/g}$ was achieved for the light elements carbon, sulphur and phosphorus in steel. This work formed the basis for the online application of LIBS in the steel industry since then. In 2002, Khater et al. [56] noted that the strongest spectral lines of light elements are emitted in the VUV region and so VUV LIBS could be useful there. However, spectra in this range can only be obtained by evacuating the target chamber and spectrometer, or by purging it with low pressures of inert gases like helium or argon. If these experiments are performed in air, at even modestly high pressure, VUV Light will be absorbed due to the large N_2 and O_2 absorption cross sections in the VUV [17].

There are various types of spectrometer designs that are used for LIBS including Czerny-Turner [57, 58, 59,62], Paschen-Runge [60,61], Echelle [62] and Normal Incidence [11,12]. The Czerny Turner spectrometer was used for the detection of carbon in steel in both solid and liquid phases using an intensified photodiode array (IPDA) based on a microchannel plate (MCP) coupled to a photodiode array (PDA) [58, 59]. It resulted in a limit of detection (LoD) of about 65 $\mu\text{g/g}$ and 250 $\mu\text{g/g}$ using the C 193.09 nm spectral line for solid and liquid phases respectively. The spectrometer used possessed a focal length of 0.5 m with a high resolution of about 0.02 nm [63].

Echelle based spectrometers provide high spectral resolution (e.g., down to 0.005 nm in a compact system). Multiplexed versions (e.g., the Andor Technology Mechelle [64]), additionally provide wide spectral range and compatibility with detectors like MCP-PDA (IPDA) or MCP-CCD (ICCD) [65]. There are very few publications on LIBS in the VUV range below 120 nm. Some groups have worked on the deep ultraviolet region for the detection

of light elements. A visible-ultraviolet multiplexed version of an Echelle spectrometric system was specially designed for the detection of light elements like C, S, and P in steel using the wavelength range of 178-200 nm. This system can record a continuous spectral range between 150 and 300 nm [66]. The Paschen-Runge system captures a broad wavelength range and as an example a system with a spectral resolution of 0.02 nm at about 460 nm has been reported [57]. Spectrometers based on the Paschen-Runge optical configuration are widely used in steel analysis in VUV and far UV ranges due to high dispersion capacity. In one of the studies a LoD of below 10 μ g/g was set for the far UV spectral range of 178 to 194 nm [55,57]. The near normal incidence concave grating spectrograph can also be used in the VUV range from 40 - 120 nm and was used in the studies presented in this thesis. The particular spectrometer used here, Acton Research Corporation Model VM521, is fitted with a 1200 grooves/mm reflective concave grating with a back illuminated CCD or BI-CCD detector manufactured by Andor Technology [11,12].

It is well known that the experimental conditions (geometrical arrangement of the laser, laser wavelength, irradiance, focusing optics, target/sample placement, shape, etc.) influence the plasma characteristics such as plasma temperature and density, and consequently observables like atomic emission intensities and mass of the ablated material. The laser can be focused by a spherical or cylindrical lens (or even a sphero-cylindrical lens) depending upon the size (and shape) of plasma required for investigation. Without proper focusing (or defocusing) of the laser radiation, an inhomogeneous plasma may be produced which may result in reduced sensitivity and poor reproducibility. To set the laser radiation focus correctly on the sample, the geometry of the experimental setup is determined by lens type (cylindrical or spherical), the focal length of the lens used for the study, the distance between the lens and the sample, and the angle of laser incidence [1,9]. There are various studies performed using the cylindrical lens and line focused plasmas [1,9,67,68], for different applications. Rodolfa

and Cremers [69] used cylindrical optics to create a linear spark for spatial surface mapping and Mateo et.al used it for fast atomic mapping of heterogeneous surfaces [68].

1.4 Thesis Organization

This doctoral dissertation is organized in a manner designed to make clear the research carried out during the project and to present it in a progressive way by addressing the problems to be solved and their relevance in the introductory chapters, followed by materials and methods used to carry out the experiments. The detailed presentation of the equipment used for the laboratory work and experimental setup design is followed by chapters presenting the results and their discussion. Summary of each chapter is presented to outline the important points. Overall project conclusions and future perspectives are presented in the last chapter.

Briefly, the contents of each chapter are:

Chapter 1 - The first chapter describes the motivation, aims and objectives of the work performed in this doctoral project. An introduction to LIBS, covering history and related recent studies is presented.

Chapter 2 - This chapter includes salient aspects of the theoretical background related to laser produced plasmas. Topics including plasma formation, plasma properties and atomic processes are presented. The concepts underlying the experimental techniques and evaluation of spectra are also discussed.

Chapter 3 - The experimental setups implemented for the research work are described in this chapter. Details on the range of diagnostic techniques are presented in this chapter. These techniques were used to perform various experiments on limit of detection (LoD) optimization of carbon in steel.

Chapter 4 - This chapter presents the results arising from research performed to detect carbon in steel samples using vacuum ultraviolet (VUV) LIBS. A comparison of the results obtained with the time resolved VUV LIBS system to those obtained with the time integrated LIBS system is presented.

Chapter 5 - This chapter shows results obtained from studies performed on laser produced line focus plasmas of carbon in steel samples. Results and a discussion of the optimisation of limit of detection (LoD) and comparison with the value obtained using a conventional point plasma VUV LIBS are presented.

Chapter 6 - The final chapter highlights the important findings and presents the overall discussion and concluding remarks for all the work performed in this doctoral project. A future perspective on VUV LIBS for applications in material characterisation is also provided.

Appendices

Appendix 1 – Results and a discussion on depth profiling applied to aluminium thin films deposited on silicon substrates are presented in this appendix. Details on ablation rates and crater size using optical and 3D microscopy are discussed.

Appendix 2 – This appendix presents results on multivariate analysis for the classification and identification of different metals and semiconducting material samples. The results from the application of Principal Component Analysis (PCA) to the measured spectra are included in this appendix. Moreover, the preliminary results for the material identification by calculating Euclidean distance between the respective principal components are also included in this appendix.

References

- [1] Hahn D.W, Omenetto N. 2010 Appl. Spectrosc. **64** pp 335A-366A.
- [2] Radziemski L, Cremers D. 2013 Spectrochim. Acta - Part B At. Spectrosc. **87** pp 3-10.
- [3] Vetter W, Schreiner M.A. 2014 Adv. Chem. Sci. **3** pp 7-14.
- [4] Bricklemyer R, Brown D, Turk P, Clegg S. 2018 Soil Sci. Soc. Am. J. **82** pp 1482-1496.
- [5] Singh J.P, Yueh F.Y, Bhatt C.R. 2020 Chapter 25 Laser Induced Breakdown Spectroscopy (Second Edition) Elsevier pp 581-590 (ISBN 978-0-12-818829-3)
- [6] Senesi G.S, Harmon R.S, Hark R.R. 2020 Chapter 23 Laser Induced Breakdown Spectroscopy (Second Edition) Elsevier pp 537-560 (ISBN 978-0-12-818829-3).
- [7] Day D.R, Derman K, Egan J.F, Soucy P.E, 2018 United States patent US 9,952 100.
- [8] Veis P, Marín-Roldán A, Krištof J. 2018 Plasma Sources Sci. Technol. **27** Art. No. 095001 pp 1-18.
- [9] Hahn D.W, Omenetto N. 2012 Appl. Spectrosc. **66** pp 347-419.
- [10] Fabre C. 2020 Spectrochim. Acta. Part B At. Spectrosc. **166** Art. No.105799 pp 1-16.
- [11] Jiang X, Hayden P, Costello J.T, Kennedy E.T. 2014 Spectrochim. Acta - Part B At. Spectrosc. **101** pp 106-113.
- [12] Khater M.A, Van Kampen P, Costello J.T, Mosnier J.P, Kennedy E.T. 2000 J. Phys. D Appl. Phys. **33**, pp 2252-22662.
- [13] Carroll P.K, Kennedy E.T. 1981 Contemp. Phys. **22** pp 61-96.
- [14] Eliezer S. 2003 The Interaction of High-Power Lasers with Plasmas (ISBN 9780750307475).
- [15] Morozov AI. 2012 Introduction to Plasma Dynamics. CRC Press (ISBN

9781439881323).

- [16] Khater M.A. 2013 Spectrochim. Acta - Part B At. Spectrosc. **81** pp 1-10.
- [17] Cremers D.A, Radziemski L.J. 2013 Handbook of Laser-Induced Breakdown Spectroscopy (ISBN 9781119971122).
- [18] Pasquini C, Cortez J, Silva L.M.C and Gonzaga F.C. 2007, J. Braz. Chem. Soc. **18** pp 463-512.
- [19] Baddoo N.R. 2008 J Constr. Steel Res. **64** pp 1199-1206.
- [20] Rombach G and Bauerschlag N. 2019 Light Metals 2019 pp 1351-1357.
- [21] W. M. Garrison 1990 JOM (Journal of The Minerals, Metals & Materials Society) **42** pp 20–24.
- [22] Balzer H, Hölter S, Sturm V, Noll R. 2006 Anal. Bioanal. Chem. **385** pp 234-239.
- [23] Semerok A and Grisolia C 2013. Nucl. Instrum. Methods Phys. Res. **720** pp 31-35.
- [24] Li C M, Zou Z.M, Yang X.Y, Hao Z.Q, Guo L.B, Li X.Y, Lua Y.F, Zeng X.Y. J. Anal. At. Spectrom. 2014 **29** pp 1432-1437.
- [25] Michaud D.D, Rollosso L.M, Ytsma C.R, Dyar M.D. 2019 50th Lunar and Planetary Conf. **2132** Art. No. 1079.
- [26] Cho M, Park S, Kwon E, Jeong S, Park K. 2019 IEEE 28th International Symposium on Industrial Electronics pp 451-454.
- [27] Debras-Guédon J, Liodec N. 1963 C. R. Acad. Sci. **257** p3336.
- [28] Schroeder W.W, Van Niekerk J.J, Dicks L, Strasheim A, Piepen H. 1971 Spectrochim. Acta - Part B At. Spectrosc. **26** pp 331-340.
- [29] Grant W.B and Menzies R.T 1983. J Air Waste. Manag. Assoc. **33** pp 187-194.

- [30] Marich K.W, Carr P.W, Treytl W.J, Glick D. 1970 Anal. Chem. **42** pp 1775-1779.
- [31] Lauterborn W. 1972 Appl. Phys. Lett. **21** pp 27-29.
- [32] Fujimoto J.G, Lin W.Z, Ippen E.P, Puliafito C.A, Steinert R.F. 1985 Invest. Ophthalmol. Vis. Sci. **26** pp 1771-1777.
- [33] Radziemski L.J, Loree T. R, Cremers D.A, Hoffman N.M. 1983. Anal. Chem. **55** pp 1246-1252.
- [34] Girault C, Damiani D, Aubreton J, Catherinot A. 1989 Appl. Phys. Lett. **55** pp 182-184.
- [35] Xu L, Bulatov V, Gridin V.V, Schechter I. 1997. Anal. Chem. 69, pp 2103-2108.
- [36] Davies C.M, Telle H.H, Montgomery D.J, Corbett R.E. 1995 Spectrochim. Acta - Part B At. Spectrosc. **50** pp 1059-1075.
- [37] Rosenwasser S, Asimellis G, Bromley B, Hazlett R, Martin J, Pearce T, Zigler A. 2001 Spectrochim. Acta - Part B At. Spectrosc. **56** pp 707-714.
- [38] Carranza J.E, Hahn D.W. 2002 Spectrochim. Acta - Part B At. Spectrosc. **57** pp 779-790.
- [39] Carranza J.E, Hahn D.W. 2002 Anal. Chem. **74** pp 5450-5454.
- [40] Yalçın Ş, Crosley D.R, Smith G.P, Faris G.W. 1996 Env. Engg. Sci. Hazard. Waste Hazard. Mat.13 pp 51-61.
- [41] Grant K.J, Paul G.L, O'Neill J.A. 1990 Appl. Spectrosc. **44** pp 1711-1714.
- [42] Scholten J.H, Teule J.M, Zafirooulos V, Heeren R.M. 2000 J. Cult. Herit. **1** pp S215-S220.
- [43] Davies C.M, Telle H.H, Montgomery D.J, Corbett R.E. 1995 Spectrochim. Acta - Part B At. Spectrosc. **50** pp 1059-1075.

- [44] Cremers D.A, Barefield J.E, Koskelo A.C. 1995 Appl. Spectrosc. **49** pp 857-860.
- [45] Knight A.K, Scherbarth N.L, Cremers D.A, Ferris M.J. 2000. Appl. Spec. **54** pp 331-340.
- [46] Stroupe, A.W. 1999. Icebreaker Scientific Package: A Proposed Scientific Instrument Suite for a Lunar Polar Mission. Carnegie Mellon University, the Robotics Institute.
- [47] Gaudio R, Melikechi N, Abdel-Salam Z.A, Harith M.A, Palleschi V, Motto-Ros V, Busser B. 2019 Spectrochim. Acta - Part B At. Spectrosc. **152** pp 123-148.
- [48] Rehse S.J. 2014 Biomedical Applications of LIBS. In: Musazzi S., Perini U. (eds) Laser-Induced Breakdown Spectroscopy. Springer Series in Optical Sciences, **182**. Springer, Berlin, Heidelberg (ISBN 978-3-642-45085-3).
- [49] Aguirre M.Á, Hidalgo M, Canals A, Nóbrega J.A, Pereira-Filho ER. 2013 Talanta **117** pp 419-424.
- [50] Pořízka P, Demidov A, Kaiser J, Keivanian J, Gornushkin I, Panne U, Riedel J. 2014 Spectrochim. Acta Part B At. Spectrosc. **101** pp 155-163.
- [51] Pagnin L, Brunnbauer L, Wiesinger R, Limbeck A, Schreiner M. 2020 Anal. Bioanal. Chem. **412** pp 3187–3198.
- [52] Sturm V, Erben B, Fleige R, Wirz W. 2019 Opt. Express. **27** pp 36855-36863.
- [53] Cremers, D.A, Beddingfield A, Smithwick R, Chinni R.C, Jones C.R, Beardsley B, Karch L. 2012. Appl. Spec. **66** pp 250-261.
- [54] Maeng H, Chae H, Lee H, Kim G, Lee H, Kim K, Kwak J, Cho G, Park K. 2017 Aerosol Sci. Technol. **51** pp 1009-1015.
- [55] Sturm V, Peter L, Noll R. 2000 Appl. Spectrosc. **54** pp 1275-1278.
- [56] Khater M.A, Costello J.T, Kennedy E.T. 2002 Appl. Spectrosc. **56** pp 970-983.

- [57] R. Noll. 2012 Laser-Induced Breakdown Spectroscopy: Fundamentals and Applications, 1st Edition. Springer-Verlag, Berlin, (ISBN 978-3-642-20667-2).
- [58] Aragon C, Aguilera J.A, Penalba F. 1999 Appl. Spectrosc. **53** pp 1259-1267.
- [59] Gruber J, Heitz J, Arnold N, Bäuerle D, Ramaseder N, Meyer W, Hochörtler J, Koch F. 2004 Appl. Spectrosc. **58** pp 457-462.
- [60] Sturm V, Vrenegor J, Noll R, Hemmerlin M. 2004 J. Anal. At. Spectrom. **19** pp 451-456.
- [61] Werheit P, Fricke-Begemann C, Gesing M, Noll R. 2011 J. Anal. At. Spec. **26** pp 2166-2174.
- [62] Zhu X, Xu T, Lin Q, Liang L, Niu G, Lai H, Xu M, Wang X, Li H, Duan Y. 2014 Spectrochim. Acta Part B At. Spectrosc. **93** pp 8-13.
- [63] Aguilera J.A, Aragon C, Campos J. 1992 Appl. Spectrosc. **46** pp 1382-1387.
- [64] Andor Technology Inc. <https://andor.oxinst.com/products/spectrographs-solutions>
- [65] Miziolek A.W, Palleschi V, Schechter I, Editors. Laser Induced Breakdown Spectroscopy. Cambridge university press; 2006 (ISBN 9780521852746).
- [66] Harvey P.D. 1982 Engineering Properties of Steel, American Society for Metals, Michigan (ISBN 9780871701442).
- [67] Eppler A.S, Cremers D.A, Hickmott D.D, Ferris M.J, Koskelo A.C. 1996 Appl. Spectrosc. **50** pp 1175-1181.
- [68] Mateo M.P, Palanco S, Vadillo J.M, Laserna J.J. 2000 Appl. Spectrosc. **54** pp 1429-1434.
- [69] Rodolfa K.T, Cremers D.A. 2004 Appl. Spectrosc. **58** pp 367-375.

Chapter 2 – Theoretical Background

2.1 Plasma Definition

Plasma, generally known as fourth state of matter, is simply an ionized gas. An external source of energy is required to both create and sustain a plasma [1]. More precisely, a plasma is a local assembly of atoms and/or molecules, ions and free electrons with an overall neutral electric charge. Equation (2.1) below describes mathematically the relationship between the electron number density n_e and the density of ions in the charge state z , designated n_z . It represents one key criterion in the definition of a plasma, i.e., overall charge neutrality [3].

$$n_e = \sum_z n_z z \quad \text{eq. (2.1)}$$

This electric charge neutrality arises from the strong and long range Coulombic force within the plasma which is in contrast with the weak and short range interactions between the constituents of neutral gas, e.g., the van der Waals force between atoms or molecules which ultimately lead to condensation into a liquid or even a solid at high pressure [2,3].

The long range Coulombic order within a plasma is responsible for its ‘collective response’ to external perturbations such as an applied electric field, where each particle can interact with its neighbours, and with the perturbing force, in a concerted fashion [2]. For example, electrons, coupling to an oscillating field, will themselves oscillate collectively giving rise to the concept of a plasma wave. The ions can also behave collectively, giving rise to ion waves, but, due to their greater mass, they will have a much lower frequency. If there is a displacement of electrons within the plasma these electrons will tend to return to their

equilibrium positions. The plasma frequency, ω_p comes from the oscillatory solution to the equation of the motion of these electrons [2] and is given by the expression:

$$\omega_p = \left(\frac{n_e e^2}{m_e \epsilon_0} \right)^{\frac{1}{2}} \quad \text{eq. (2.2)}$$

where n_e is the electron density, e is the charge on an electron, m_e is the mass of an electron and ϵ_0 is the permittivity of free space. An electromagnetic wave, propagating through a plasma, will undergo dispersion. Equation 2.3 shows the mathematical relationship between the plasma and wave parameters for an electromagnetic wave travelling through a plasma, namely:

$$\omega^2 = \omega_p^2 + c^2 k^2 \quad \text{eq. (2.3)}$$

where ω_p is the plasma frequency, ω is the angular frequency of the propagating wave, c the speed of light, and k the propagation constant given by [2]:

$$k = \frac{2\pi}{\lambda} \quad \text{eq. (2.4)}$$

If $\omega > \omega_p$, k will be real, and wave propagates through the plasma. Conversely if $\omega < \omega_p$, k will have an imaginary value and the wave will not propagate. In this case the plasma becomes reflective, much like a metal mirror due to high density of free electrons at its surface.

Plasma reflectivity is an important phenomenon in the generation of laser produced plasmas since, as the electron density increases, the plasma reflectivity increases, and the laser radiation will start to be shielded from the target surface. In the case of a fully reflective plasma, the incident laser pulse cannot be absorbed. The electron density at which this occurs is designated as the critical electron density, or simply the critical density, and is given by:

$$n_c = \frac{\epsilon_0 m_e \omega^2}{e^2} \approx \frac{10^{21}}{\lambda^2} \quad \text{eq. (2.5)}$$

The ‘shielding effect’ of electrons on ions in a plasma is another important plasma phenomenon. Electrons in the plasma will naturally tend to surround the positively charged ions whereas ions of like charges will exhibit the natural tendency to separate from each other. Therefore, these electron ‘barriers’ shield the area surrounding a charged ion. Thus the influence that each individual charge can exert on its neighbours is shielded up to a characteristic distance known as the Debye length λ_D [2-5], which is given by the following expression:

$$\lambda_D = \left(\frac{\epsilon_0 k_B T_e}{n_e e^2} \right)^{\frac{1}{2}} \quad \text{eq. (2.6)}$$

where ϵ_0 is the permittivity of free space, k_B is the Boltzmann constant, T_e is the electron temperature of the plasma (in kelvin), and e is the charge on the electron. Thus, there are a number of criteria which an ionized gas must satisfy in order to be considered as a plasma. The first two criteria confirm that the plasma exhibits collective behaviour, while the third ensures that ionized gas acts like a plasma rather than a neutral gas [6].

One more characteristic property of a plasma is that the plasma dimensions L should be larger than the Debye length λ_D [2-5], i.e.

$$L \gg \lambda_D \quad \text{eq. (2.7)}$$

When the Debye length is smaller than the dimension of the plasma the collective response of a plasma becomes of primary importance, while below the Debye length, effects from individual charged particles can be felt. This shielding effect of the plasma becomes effective up to a threshold density of electrons based on the concept of the ‘Debye sphere’. This density designated the plasma parameter N_D which requires that the number of electrons n_e in any given sphere with a radius equal to the Debye length should be greater than unity [2-4], namely:

$$N_D > 1 \quad \text{eq. (2.8)}$$

The parameter N_D is essentially equal to the number of particles within the Debye sphere to ensure the statistical validation of plasma shielding.

$$N_D = \frac{4}{3}\pi n_e \lambda_D^3 \quad \text{eq. (2.9)}$$

Yet another criterion relates to the electron-neutral collision frequency, which should be lower than the plasma frequency.

$$\omega_{e_n} < \omega_p \quad \text{eq. (2.10)}$$

Typically if the plasma oscillation frequency is ω and τ is the time between collisions with neutral atoms, then the product of these two numbers should be greater than unity [6], i.e.,

$$\omega\tau > 1 \quad \text{eq. (2.11)}$$

2.2 Laser Produced Plasma Formation

A laser produced plasma is formed when a high-power laser pulse is focused onto a (usually solid) target material, with an irradiance above the material threshold, which is typically in the range of $10^8 - 10^{10} \text{ W/cm}^2$ [4]. The detailed laser-target and laser-plasma interactions will be described below but in summary the formation process begins with single or multiphoton photoabsorption at the target surface with subsequent phase changes, solid – liquid – vapour – plasma in the host material. For some materials, the liquid phase may be omitted, or at least very short lived, if they undergo sublimation [5].

In the initial phase of laser matter interaction, material is ablated to form a dilute vapour and seed electrons are formed by photoionization in the intense laser field. Within picoseconds, electrons are raised to higher kinetic energy due to the process of inverse bremsstrahlung (IB) and ionize both the vapour and target to cause further ionization and ablation [4-6]. The on-target irradiance (in W/cm^2) and the laser wavelength determine the plasma parameters like temperature and density and are hence responsible for the degree of ionization of the plasma

plume formed in the interaction. Once the plasma has been formed, the remaining laser energy is absorbed by the expanding plasma via inverse bremsstrahlung and may also reach the target to cause further ionization there. This process takes place when the electron density of the plasma is below the critical density. Since the process is regenerative, i.e., the more laser radiation is absorbed by inverse bremsstrahlung, the higher the electron density becomes and hence the more efficient is the IB process so that this becomes an avalanche process. Once the plasma reaches the critical density, the laser radiation can no longer penetrate the plasma plume and the IB process ceases, restarting after the plume expands somewhat to reduce the plasma density so that the laser radiation can once again propagate into the plasma plume. The process continues cyclically throughout the laser pulse duration. Figure 2.1 below shows the approximate time scales for the different epochs of formation and evolution of plasma [7].

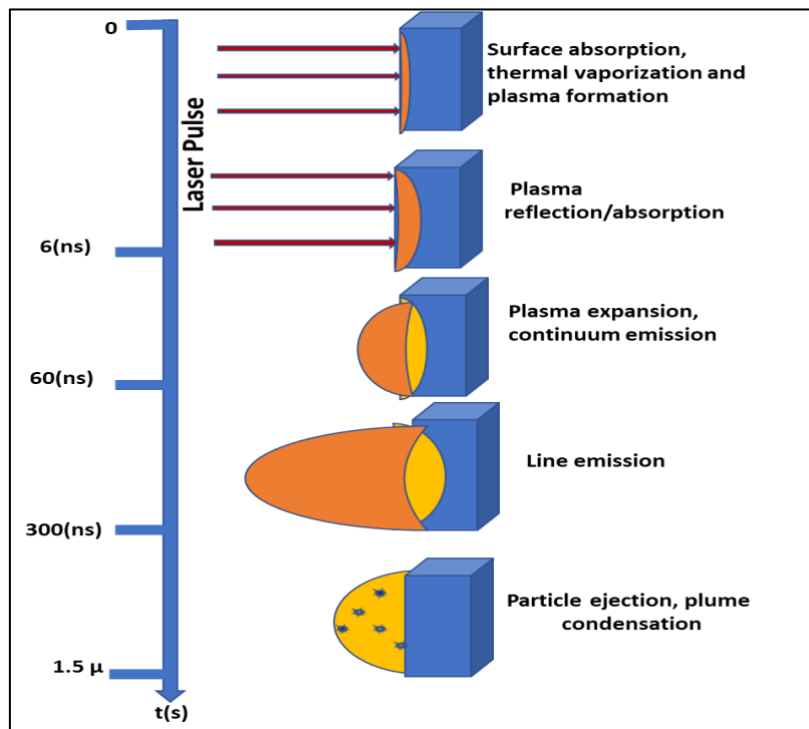


Figure 2. 1 Laser produced plasma formation and expansion *in vacuo*, illustrating the different evolutionary stages from the plasma formation to late phase plume condensation which can yield clusters for materials growth.

Referring to that figure, the formation and evolution of a laser produced plasma can be divided into three key stages [8], namely:

1. Laser-matter interaction – occurs when laser pulse interacts with the target material.
2. Laser-plasma interaction – occurs when laser pulse interacts with the plasma formed in stage 1.
3. Plasma expansion – The expansion (often adiabatic) of the ablated plume into the surrounding medium (vacuum or gas) after the laser pulse has terminated.

The three stages above are described in additional detail in the following three subsections.

2.2.1 Laser-Matter Interaction

Laser-matter interaction phase refers to the direct laser surface interaction and the initial removal of matter into a vapour cloud via laser ablation. When a laser pulse is incident on the target surface some of the radiation is reflected from the surface while a portion of it penetrates the surface. The skin depth δ is a measure of the penetration distance and is typically a fraction of the incident radiation wavelength. It is given by the expression:

$$\delta = \left(\frac{2}{\omega \mu \sigma} \right)^{\frac{1}{2}} \quad \text{eq. (2.12)}$$

Where ω is the angular frequency of the incident laser radiation, μ the magnetic permeability of free-space, and σ the conductivity of the target material [9]. Electrons absorb the radiation from the incident laser field and these free electrons can transfer energy into the bulk material to a heat penetration depth L_{th} given by [9]:

$$L_{th} \approx (2D\tau_L)^{\frac{1}{2}} \quad \text{eq. (2.13)}$$

where τ_L is the duration of the laser pulse and D is the heat diffusion coefficient given by $D=k/\rho C$, where k is the thermal conductivity, ρ is the mass density, C the specific heat capacity.

The heat penetration depth for nanosecond lasers incident on metal targets is on the order of $\sim 1 \mu m$, significantly larger than the laser optical field penetration depth [9], i.e.,

$$L_{th} \gg \delta \quad \text{eq. (2.14)}$$

So, the energy that is absorbed at the material surface and down to a dimension equal to the skin depth is transferred thermally in the bulk and hence the target material can undergo phase changes from solid to liquid to vapour states. During these induced phase changes, which occur as a result of irradiation by a laser pulse on the nanosecond timescale, vaporization usually requires much more energy deposition than melting. Evaporation will take place when the degree of heat penetration depth into the bulk material is such that it exceeds the latent heat of evaporation per unit volume.

The ablation depth ΔZ_v depends on the A_s , the surface absorption coefficient, F_L the laser fluence, F_{th} the threshold fluence and L_v the latent heat of vaporization and is given by the following equation [10].

$$\Delta Z_v \approx \frac{A_s(F_L - F_{th})}{\rho L_v} \quad \text{eq. (2.15)}$$

The minimum energy at which adequate ablation takes place is usually specified as a threshold fluence and is typically the value needed to yield ablation of material to a depth equal to the heat penetration depth, i.e., L_{th} which is, in turn, approximated as [10]:

$$F_{th} \approx \frac{\rho C \Delta T_m L_{th}}{A_s} \quad \text{eq. (2.16)}$$

where ΔT_m is the difference between the melting temperature of the material and its initial temperature and c is the specific heat capacity of the material.

The threshold fluence depends on the material's thermal and optical properties and a related parameter, known as the 'breakdown threshold' which is given in terms of laser power density or irradiance with units of Wcm^{-2} . It is obtained by dividing the threshold fluence (in

Jcm^{-2}) by the laser pulse duration. In typical LIBS experiments, the breakdown thresholds of solid targets are found to lie in the range of $10^8 - 10^{10} W cm^{-2}$ [3]. For a pulse of fundamental wavelength 1064 nm with 6ns pulse duration and pulse energy between 600 to 800 mJ, focused to the spot diameter of around 100 μm , the calculated power density is approximately $10^{12} Wcm^{-2}$ well above the breakdown threshold.

2.2.2 Laser-Plasma Interaction

After the formation of initial or pre-plasma by single and/or multiphoton ionization of the vapour above the target surface, laser radiation is absorbed by the free electrons through the process of inverse bremsstrahlung. Since the photon energy for visible and infrared lasers is generally less than the work function for most metals, the formation of the dilute pre-plasma usually occurs through multiphoton ionization or MPI.

Inverse bremsstrahlung (IB) is the process in which free electrons absorb the incident radiation within the vicinity of an ion. The latter is needed to satisfy conservation of momentum, with the ion balancing the momentum gained by the electron in this photon absorption process. Very quickly the MPI rate is overtaken by the IB rate which goes on to dominate the laser radiation absorption process. At this point it is electron collisional ionization of the plume constituents, along with target surface ionization by energetic electrons transported into the deflagration zone, that dominates. As this process continues more free electrons are produced so that the electron density continues to rise, and hence the IB rate increases, so that more of the laser energy is absorbed by more electrons which cause even further ionization and concomitantly, an even higher electron density. This interplay between the increasing electron density, leading to an increasing IB rate, leading to a high electron-ion collisional ionization rate, leading to an even higher electron density, results in an avalanche

ionization process which terminates only when the plasma reaches the critical density n_c (section 2.1).

At this point the plasma becomes opaque to the incident laser radiation which is reflected from the critical density layer. However, subsequently the plasma plume will expand, thereby reducing the electron density. When it becomes low enough, the laser can once again penetrate the plasma plume which will be able to absorb laser radiation. Hence this cyclical process of the absorption of laser radiation, leading to an increase in both free electron energy and electron impact ionization rate, leading in turn to an increase in electron density up to the point where it reaches the critical density followed by expansion repeats right throughout the duration of the laser pulse, i.e., typically for a period of nanoseconds. In this phase the expansion of the plasma is isothermal as the expansion time is significantly greater than heating time and therefore one can consider the plume to have a constant plasma temperature.

2.2.3 Plasma Expansion

The plasma is assumed to be a high temperature and high-pressure gas which expands isothermally during the temporal interval of the laser pulse. In this case thermal energy acquired via inverse bremsstrahlung and collisional excitation is balanced by the rate of heat loss to the surroundings by radiative processes. On the other hand, after the termination of the laser pulse, expansion of the plasma causes it to cool as thermal energy is rapidly converted into kinetic energy. At this point plume expansion can be described as adiabatic and the three dimensional (3D) expansion model developed by Singh and Narayan [8], can be applied to it. In this model the plasma is assumed to be an ideal gas at high pressure, temperature and fixed volume, which expands abruptly into vacuum, having been confined to a small volume before being allowed to expand. The expansion of the plasma into vacuum is given by following equation:

$$X(t) \left[\frac{d^2 X}{dt^2} \right] = Y(t) \left[\frac{d^2 Y}{dt^2} \right] = Z(t) \left[\frac{d^2 Z}{dt^2} \right] = \frac{k_B T_0}{m} \left[\frac{X_0 Y_0 Z_0}{X(t) Y(t) Z(t)} \right]^{\gamma-1} \quad \text{eq. (2.17)}$$

where X_0 , Y_0 , Z_0 , are the initial (orthogonal) edges of the plasma and T_0 is the plasma temperature, once the laser pulse has terminated. K_B is Boltzmann's constant, m is the mass of the atomic species and γ is the ratio of the specific heat capacities at constant pressure and volume [8]. This model does not differentiate between the motion of different species (e.g., ions of different charge) present in the plasma, rather it considers the expansion of the plasma plume as a single fluid.

It is evident from the equation 2.17 that expansion velocities are dependent on the initial dimensions of the plasma, with the highest velocities in the direction of smallest starting dimension. Initial dimensions of the plasma will be smaller in the direction normal to the target, where it will be typically a few μm , whereas along the target surface it will be larger by an order of magnitude or so due to the spot size 100 to 200 μm . Therefore, normal to the target surface the expansion velocity will be greater, leading to anisotropic expansion of the plasma, creating the elongated laser plasma shape [8].

As the expansion velocity for each plasma plume constituent is dependent on the mass of that species, one would expect the lighter and faster electrons expand at a faster rate than the heavier ions. Hence one would expect to observe a charge separation between the leading electrons and the following ions creating a so-called 'ambipolar field'. The charge separation is of course limited by the Coulombic restoring force of the ions on the electrons at the front of the plasma plume to typically less than the Debye length [11].

2.3 Atomic Processes in Laser Induced Plasmas

There are many processes that takes place within a laser produced plasma which facilitate the absorption, propagation and emission of radiation. Atomic processes are categorised into three main groupings or classes based on initial and final states of the electrons involved; namely bound-bound, free-bound, and free-free transitions (Table 2.1). There are two different

mechanisms of energy transfer that underlie these processes, namely radiative and collisional. Radiative processes concern the energy transfer between photons (electromagnetic radiation) and species with the plasma whereas collisional processes are related to the transfer of energy between electrons, atoms, molecules and ions within the plasma [12,13].

Table 2. 1 Primary atomic processes that occur within a laser produced plasma where B refers to bound, and F refers to free, electron processes

Process	Excitation	De-excitation	Type
B-B	Impact Excitation	Impact Deexcitation	Collisional
B-B	Photoabsorption	Spontaneous Decay	Radiative
B-F	Impact Ionization	3-Body Recombination	Collisional
B-F	Photoionization	Radiative Recombination	Radiative
F-F	Bremsstrahlung	-	Collisional
F-F	-	Inverse Bremsstrahlung	Radiative

2.3.1 Bound-Bound Processes

There are four bound-bound processes, two collisional and two radiative. These bound-bound processes describe the transitions of electrons between discrete electronic states of an atom or ion.

i. Collisional Processes

When a free electron collides with an atom or ion it may gain or lose energy. If the free electron transfers energy to the atom, the bound electron is promoted to a higher energy state. This

process is referred as electron impact excitation (figure 2.2). The inverse situation is known as electron impact deexcitation, where a bound electron is induced to drop down to a lower energy state, emitting the excess energy in the form of a photon. Equation 2.18 describes the collisional excitation processes [15]:

$$A + e(\epsilon_1) \rightarrow A^* + e(\epsilon_2) \quad \text{where}(\epsilon_2 < \epsilon_1) \quad \text{eq. (2.18)}$$

while equation 2.19 describes the collisional deexcitation process:

$$A^* + e(\epsilon_1) \rightarrow A + h\nu + e(\epsilon_2) \quad \text{where}(\epsilon_2 = \epsilon_1) \quad \text{eq. (2.19)}$$

Where A is an atom or ion in its ground state, A* is the same atom/ion in an excited state. ϵ_1 and ϵ_2 are the kinetic energies of the free electron before and after the collision.

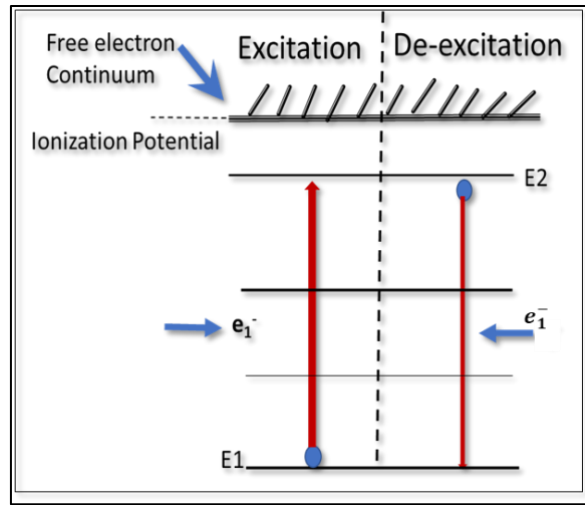


Figure 2. 2 Schematic of electron impact collisional excitation and de-excitation occurring in a laser produced plasma where the upper bound state has energy E2 and lower bound state has energy E1

When an electron is excited to a higher energy state by the absorption of photon the process is known as photoabsorption. In the inverse situation when the electron drops stochastically to a lower energy state by the emission of a photon the process is known as

spontaneous decay. Both processes are illustrated in figure 2.3 and described by equation 2.20 below.

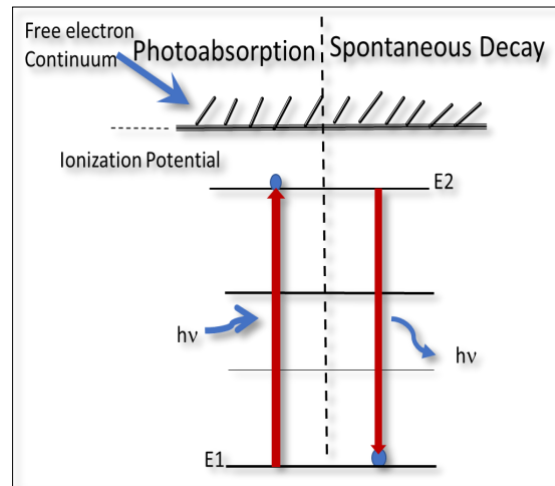


Figure 2. 3 Pure radiative processes, namely photoabsorption and photoemission of line radiation arising from bound to bound transitions

2.3.2 Free Bound Processes

i. Collisional Processes

When a free electron collides with a bound electron in an atom or ion and transfers enough energy to promote the bound electron into a continuum state, this process is known as electron impact ionization and it results in the ionization of target atom. 3-body recombination is its inverse process, and it takes place in relatively high-density plasmas where there is a high probability of finding two free electrons entering into the Debye sphere of an ion. The ion captures the first electron whereas the second electron absorbs the surplus energy in the form of a gain in kinetic energy. Since an ion, and two free electrons are involved in this process it is termed “3-body” recombination. These two processes are illustrated in figure 2.4 (a) described by the following balance equation:

$$A^z + e_1(\epsilon_1) \rightleftharpoons A^{z+1} + e'_1(\epsilon'_1) + e_2(\epsilon_2) \quad \epsilon_1 > \epsilon'_1 \quad \text{eq. (2.21)}$$

where z is the charge state, ϵ_1 represents the energy of the incoming electron, ϵ'_1 is its post interaction energy whereas ϵ_2 is the liberated free electron energy. The forward equation illustrates the ionization step whereas the reverse represents the 3-body recombination process. The two processes are illustrated in figure 2.4(a).

ii. Radiative Processes

When a photon of energy greater than binding energy of the atom is absorbed by a bound electron, the electron is freed from the atom, i.e., it is promoted into a continuum (free electron) state and the parent atom is ionized. This phenomenon is known as photoionization and is illustrated in figure 2.4(b). When there is a very high photon energy more than one electron may be liberated, which is known as single photon, multielectron ionization. This process is only possible when strong electron-electron correlation prevails [15].

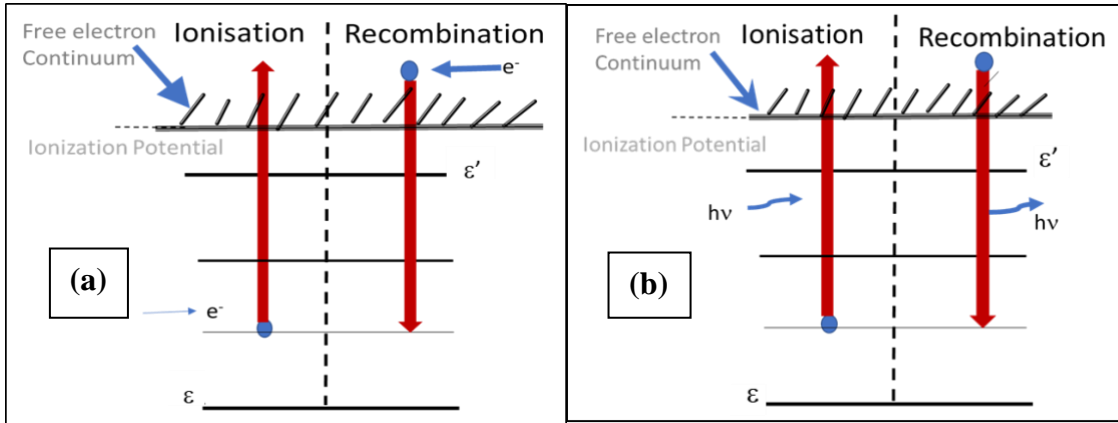


Figure 2. 4 Bound-free processes taking place within a laser produced plasma. (a) The left hand side figure represents the electron collisional processes (impact ionization and 3-body recombination). a) Shows the radiative processes of photoionization and radiative recombination. The blue dots represent the ionizing and recombining electrons in each panel.

In the inverse process, a free electron is captured by an ion into an excited bound state of that ion. It therefore emits a photon with an energy equal to the sum of the free electron (kinetic) energy and the binding energy of the state into which the electron has been captured. The process is known as radiative recombination. Since free electrons in a laser produced plasma will have a continuum of kinetic energies, the radiative recombination spectrum will be continuous in wavelength or frequency. Equation 2.22 illustrates these processes with photoionization going from left to right and radiative recombination is the opposite direction.

$$A^Z + h\nu \rightleftharpoons A^{Z+1} + e \quad \text{eq. (2.22)}$$

2.3.3 Free-Free Processes

The free-free processes occurring in a plasma are designated bremsstrahlung and inverse bremsstrahlung (IB) respectively and are illustrated in figure 2.5 below. The importance of IB in the formation and heating of laser produced plasmas has already been noted above in Section 2.2. Bremsstrahlung is dominant in the early stage of plasma evolution, typically for times less than 100 ns. Bremsstrahlung is caused by the collisions between free electrons and ions or neutrals as expressed in equation 2.23. Due to these collisions, electrons lose kinetic energy which is converted into continuum radiation. This type of broadband radiation is one of the most characteristic signatures of laser produced plasma.

iii. Collisional Processes

When an electron passes within the vicinity of an ion, it will sense its Columbic field and may decelerate resulting in the emission of photon. Since the radiation is produced by deceleration of the free electron it is referred as “braking radiation” or bremsstrahlung and is usually observed in the early stages of laser produced plasma formation and evolution. Once again, as

free electrons in a thermal plasma, like a LIBS plasma, possess a continuous distribution of kinetic energies, bremsstrahlung exhibits a continuum spectrum [15].

iv. Radiation Processes

When a free electron passes close to an ion, it can absorb a photon thereby increasing its kinetic energy. This process is only possible when the electron is in the vicinity of an ion so that the momentum gained by the electron can be transferred to the heavier ion to ensure momentum conservation. The two free- free pathways are described in the equation 2.23, where forward direction represents Bremsstrahlung, whereas IB is vice-versa.

$$A^Z + e(\epsilon) \rightleftharpoons A^Z + e'(\epsilon') + h\nu \quad \epsilon > \epsilon' \quad 2.23$$

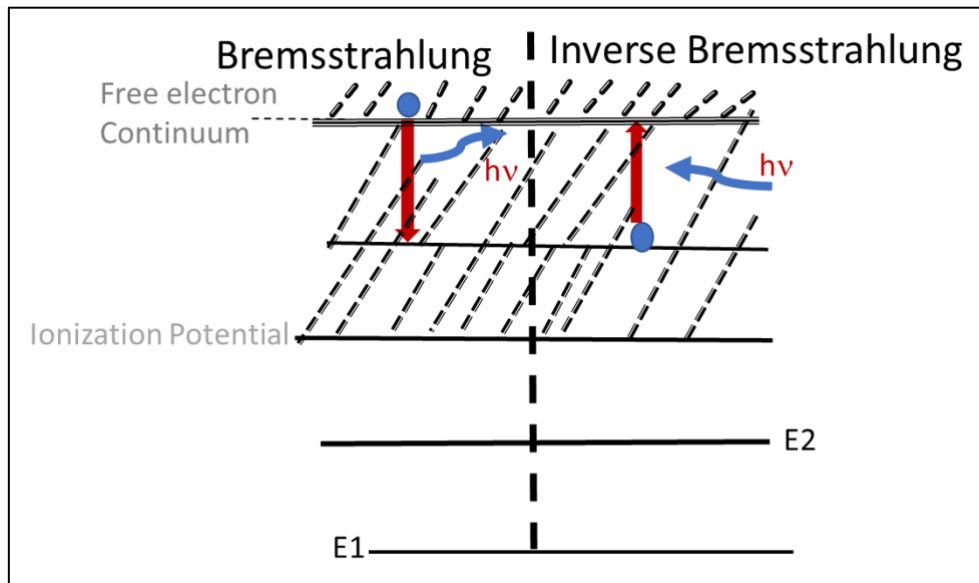


Figure 2. 5 Bremsstrahlung and inverse-bremsstrahlung taking place within the produced plasma. The upper and lower continuum states are designated ϵ and ϵ' , with $\epsilon > \epsilon'$. E1 and E2 refer to two typical bound states of the atom or ion.

2.4 Equilibrium in Plasmas

Figure 2.6 illustrates the limits density and temperature limits pertaining to the different equilibria which can exist in a plasma. Any plasma which exists in a complete thermodynamic equilibrium (LTE) state must meet following criteria [2,14-18];

- All plasma species i.e., electrons, ions and neutrals must exhibit a Maxwell velocity distribution
- The Boltzmann formula describes the population distributions over states of any atom or ion (excitation balance)
- There must be ionization balance, as described by the Saha equation (which relates the number density of ions with charge z to those of charge $(z-1)$)
- The Planck radiation distribution function describes the intensity distribution of emitted radiation

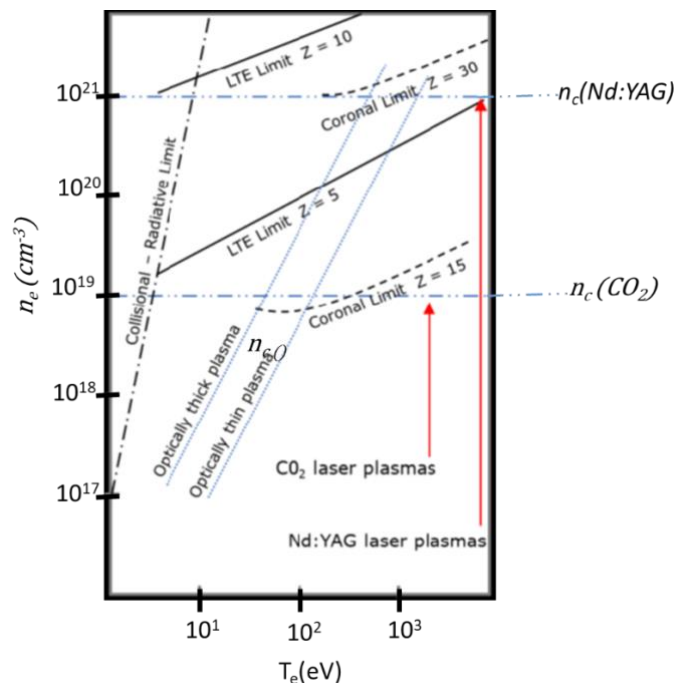


Figure 2. 6 Criteria for the validity of different thermodynamic equilibrium models as a function of electron temperature and density [15] .The critical density for CO₂ and Nd:YAG laser produced plasmas is also marked by the horizontal lines.

Plasmas in complete thermodynamic equilibrium (CTE) exhibit a detailed balance between each atomic excitation and ionization process, collisional and radiative. Although, it is not possible in laboratory plasmas due to energy losses through emission of radiation, there are three thermodynamic models which can be used, in limited circumstances, to describe laboratory plasmas:

1. Local Thermodynamic Equilibrium (LTE)
2. Coronal Equilibrium (CE)
3. Collisional Radiative Equilibrium (CRE)

These three models are explained in detail below.

2.4.1 Local Thermal Equilibrium

A system which is dominated by the collisional excitation and deexcitation is said to exist in local thermodynamic equilibrium (LTE). This model is valid for a plasma when there is a high electron density, so that the collision frequency between plasma species is high. The processes of electron impact excitation and ionization must be equal to the rate of collisional de-excitation and three body recombination in the plasma for this model to be valid. There should be a greater probability for an ion returning to the ground state through collisional de-excitation compared to spontaneous emission and therefore a critical value of electron density is required for LTE to hold in a plasma. This condition puts a lower limit on the electron density n_e for LTE to hold true, which is given by the McWhiter criterion[18]:

$$n_e \geq 1.6 \times 10^{12} T_e^{\frac{1}{2}} \chi^3 \text{ cm}^{-3} \quad \text{eq. (2.24)}$$

where T_e is the electron temperature and χ is the excitation energy of the transition under consideration, in units of electron volts (eV).

It is clear that the threshold electron density scales very strongly with (to the third power of) the transition energy. Griem et.al [19] provided the example of a hydrogen plasma where his analysis suggested that at temperature of 1eV ($\sim 11000\text{K}$) and atmospheric pressure, an electron density of $10^{17}/\text{cm}^3$ would confirm the predominance of LTE. This implies that LTE can be achieved in a LIBS plasma generated by an irradiance of $> 10^8\text{W}/\text{cm}^2$.

2.4.2 Coronal Equilibrium (CE)

The CE model is valid for optically thin plasmas with low density which are typically found in solar coronas. In this case electron collisions are the main cause of excitation and ionization, both of which are balanced by deexcitation and radiative recombination processes [2,16,17,19]. Due to the low electron density the collisional excitation rates are low and hence excited electrons will have enough time to relax to the ground state before another collisional excitation event takes place. Therefore, most ions in the plasma are in their respective ground states. In a plasma that exists in CE, the radiation emitted by the species within the plasma is not reabsorbed as it travels through it, which implies that both photoexcitation and photoabsorption are negligible. Hence, in this model collisional processes excite the atoms and ions but, due to low electron density, collisional de-excitation is rare.

2.4.3 Collisional Radiative Equilibrium (CRE)

The Collisional Radiative model defines an intermediate equilibrium between the Coronal and the LTE models. The CRE model tends to the Coronal model at low density and to the LTE model at high density. In this model both collisional and radiative processes have to be considered. The applicability of the CRE model is based on the conditions mentioned by Colombant and Tonon [17]:

- Only collisions involving electrons, which are more efficient than collisions between heavy particles are taken into account, and the process of autoionization and its inverse process, i.e., dielectric recombination are neglected
- The velocity distribution of electrons is considered to be Maxwellian; this condition is fulfilled when the electron-electron relaxation time is smaller than electron heating time. At high electron density the electron relaxation time is the smallest time characteristic in the plasma
- The population density of ions of charge $z + 1$ must not change intensely when the quasi-steady-state population of ions of charge z is being formed
- The plasma must be optically thin to its own radiation therefore the photon-ion interactions can be neglected

This model is appropriate for electron densities in the range between 10^{19} cm^{-3} to 10^{21} cm^{-3} .

2.5 Quantitative Spectroscopy Using Laser Plasmas

Quantitative spectroscopy is based on the use of the emission from the laser produced plasmas which is intrinsically dependent upon the quantity of the elements present in the complex host sample. Two main methodologies are applied to study laser produced plasmas namely, atomic absorption spectroscopy (AAS) and atomic emission spectroscopy (AES). The basic principle of AAS is that atomic and molecular species in various different states of ionization will absorb photons at discrete wavelengths. This absorbance is dependent on the electronic structure of the atom or ion under study. AES uses opposite mechanism where a hot plasma is used as an excitation source which emits both line and continuum radiation. Both radiation types can be used to diagnose conditions (e.g., temperature and/or electron density) within a plasma. The line radiation is characteristic of the element or elements in the plasma and can be used to identify and sometimes quantify those elements.

2.5.1 Number Density of the Species Under Analysis

For quantitative spectroscopic studies of laser produced plasmas we can state very simply that ‘more atoms mean more emission’. Therefore, when the concentration of the element changes there is a corresponding change in the integrated intensity of the emitted spectral line due to the change in the number of species in the upper energy level, designated ‘k’ in equation 2.25 below, of the observed transition, with lower energy state designated ‘i’ (Fig. 2.7). The number density of species in the upper state, designated n_k , is given by:

$$n_k = \frac{n_0 g_k e^{\frac{-E_k}{kT}}}{Q} \quad \text{eq. (2.25)}$$

where n_0 is the total number density of the species in the same ionisation state, g_k is the degeneracy of the state ‘k’. E_k is the energy of that excited state relative to the ground state of the species (in the same state of ionisation) and T is the plasma temperature.

Q in the equation 2.25 describes the canonical partition function, representing the range of degrees of freedom of an atomic species in a particular state and is summed over all permitted energy states ‘s’. It is expressed as:

$$Q = \sum_s g_s e^{E_s/kT} \quad \text{eq. (2.26)}$$

2.5.2 Line Intensity and Transition Probability for Optically Thin Plasmas

Where the number density of an element in a plasma is low, the plasma is optically thin to the radiation emitted by that element, even for transitions where the lower level is the ground state of the atom or ion under study. This is the case for the steel samples studies in this thesis where the carbon concentration is very low relative to the iron concentration. Therefore, for this work

optically thin plasmas are studied and the expression for the intensity of a line can be written in the following form:

$$I = \frac{h\nu_o X A_{ki} g_k n_0 e^{-E_k/kT}}{Q} \quad \text{eq. (2.27)}$$

In equation 2.27, A_{ki} is the (spontaneous) radiative transition probability from an upper level k to a lower level i and g_k is the degeneracy of the upper level (k) of the transition in the path length X . Figure 2.7 shows the relative transition probabilities and their relationship to the energy levels [21].

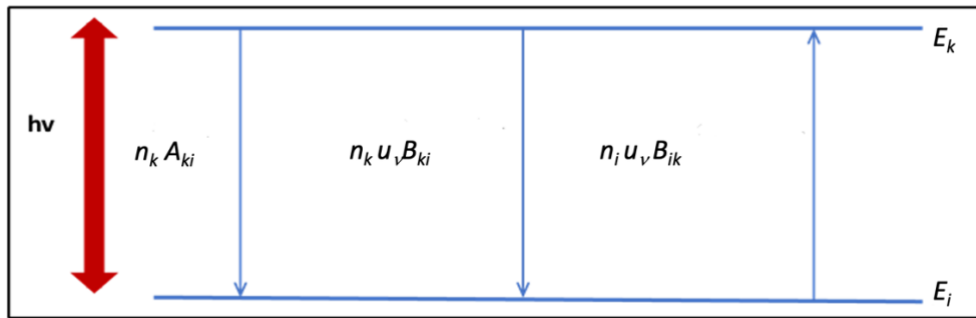


Figure 2. 7 Transition probabilities in a two-level system with lower state designated ‘i’ and upper designated ‘k’, possessing energies E_i and E_k , where $E_i < E_k$. The populations (number densities) of each state are designated as n_i and n_k respectively and have units of m^{-3} .

The frequency ‘ ν ’ associated with this transition is given by $h\nu = E_k - E_i$. Three processes are illustrated in figure 2.7, namely spontaneous emission, stimulated emission and absorption. The transition probability for each of these processes depends on their respective Einstein coefficients where A_{ki} represents spontaneous emission, B_{ki} is the Einstein coefficient for stimulated emission and B_{ik} is the Einstein coefficient for absorption. A_{ki} is a probability or rate and has units of s^{-1} . The B coefficients have units of $\text{m}^3 \text{J}^{-1} \text{s}^{-2}$. The number of absorption processes per second per m^3 , under the influence of a radiation field with a spectral (radiant) energy density u_ν is given by $N_{ik} = n_i u_\nu B_{ik}$ [19], where u_ν has units of J.s.m^{-3} or more commonly $\text{J.m}^{-3}.\text{Hz}^{-1}$. On the other hand, the number of emission events per

second per m³ is comprises both stimulated and spontaneous processes and is given by $N_{ki} = n_k u_\nu B_{ki} + n_k A_{ki}$.

2.5.3 Spectral Line Intensities – Radiative Transfer

For a laser produced plasma in local thermal equilibrium (LTE) the ‘spectral radiance’, I_ν , more commonly specified as ‘the intensity of a spectral line’ at a frequency ‘ ν ’ is defined as the energy emitted from the plasma per unit time, surface area, solid angle and frequency in units of J.s⁻¹.m⁻².sr⁻¹.Hz⁻¹ or W.m⁻².sr⁻¹.Hz⁻¹. The equation of radiative transfer can be used to express the change in the intensity of a spectral line or spectral radiance along a specific direction [20]. It can be derived by considering a beam of radiation, contained in a small solid angle $d\Omega$ [20], passing through a slice of plasma extending position ‘ x ’ to position ‘ $x + dx$ ’.

One can write that:

$$N_{ik} = B_{ik}u_\nu = B_{ik}^I I_\nu \quad \text{eq. (2.28)}$$

where N_{ik} is number of absorption process per second per cm³ and i and k are the lower and upper energy levels of the transition under consideration. Here we define B^I as the intensity form of the B coefficient such that it satisfies the equality in equation 2.28. I_ν is defined as the spectral radiance and the spectral radiant energy density u_ν of a given radiation field are related by:

$$I_\nu = \frac{c}{4\pi} u_\nu$$

We express now the change in the radiation intensity at frequency between ν and $\nu + d\nu$ between x and $x + dx$, in a cylinder of cross section dS , for a time interval dt :

$$(I_\nu(x + dx) - I_\nu(x)) dS d\nu d\Omega dt = \frac{dI_\nu(x)}{dx} dx dS d\nu d\Omega dt \quad \text{eq. (2.29)}$$

This quantity corresponds to the difference between the energy emitted and the energy absorbed during the same time interval dt . Considering a transition between two energy levels i and k , with $E_i < E_k$, the energy emitted either by spontaneous or stimulated emission from level k can be written as:

$$E_{emitted} = h\nu n_k A_{ki} g_\nu dS d\nu dx dt \frac{d\Omega}{4\pi} + h\nu n_k B_{ki}^I g_\nu dS d\nu dx dt \frac{d\Omega}{4\pi} I_\nu \quad \text{eq. (2.30)}$$

If n_i is the population density of level i then:

$$E_{absorbed} = h\nu n_i B_{ik}^I g_\nu dS d\nu dx dt \frac{d\Omega}{4\pi} I_\nu \quad \text{eq. (2.31)}$$

The function g_ν is the line shape function for the transition of interest. It must be introduced since the Einstein coefficients are frequency averaged and if transition rates induced by monochromatic light are needed the Einstein coefficients have to be multiplied by the appropriate normalised line shape function.

The equation of radiative transfer relates the difference in intensity between x and $x + dx$, to the difference between the energy absorbed and emitted, and it can be written as:

$$\frac{dI_\nu}{dx} = \frac{h\nu}{4\pi} \left(A_{ki} n_k + (B_{ki}^I n_k - B_{ik}^I n_i) I_\nu \right) g_\nu \quad \text{eq. (2.32)}$$

or

$$\frac{dI_\nu}{dx} = \varepsilon_\nu - K_\nu I_\nu \quad \text{eq. (2.33)}$$

where ε_ν is the volume emission coefficient and K_ν is the volume absorption coefficient defined by:

$$\varepsilon_{\nu} = \frac{h\nu}{4\pi} A_{ki} n_k g_{\nu} \quad \text{eq. (2.34)}$$

and

$$K_{\nu} = \frac{h\nu}{4\pi} B'_{ik} n_i \left(1 - \frac{g_i n_k}{g_k n_i} \right) g_{\nu} \quad \text{eq. (2.35)}$$

With the change in the elemental concentration there is a corresponding change in the integrated intensity of the emitted spectral lines because of the change in the number density n_l . The number density indicates the number of the particular excited species with electrons populating the upper energy level 'k' of the observed transition and is contained in the optical density parameter $K_{\nu}X$, where 'X' is length of the plasma in our case.

2.5.4 Analytical Calibration Function and Curve:

Equation 2.31 is the fundamental equation for emission spectroscopy, which can be used to determine the population density of relevant species (atoms or ions) for an element in the plasma from a measurement of the absolute line intensity of the corresponding transition and knowledge of excitation constants and other atomic constants. However, it is not possible to derive a theoretical expression relating number density n_0 in equation 2.31 to the absolute concentration of that element in the original solid sample or target. Hence, in practice an empirical relationship between observed line intensity and its corresponding concentration is used instead. This relationship is known as analytical calibration function, expressed in the equation:

$$I = f(C) \quad \text{eq. (2.36)}$$

Plots of this intensity versus the concentration of the element under analysis in the target material are known as analytical calibration curves and are considered as basis of experimental analytical spectroscopy.

2.5.5 Emission from Steel Plasmas in the VUV Spectroscopy

Laser produced plasmas emit both continuum and line emission within the VUV wavelength range, typically from 35 to 180 nm [17]. During the early stages of the plasma lifetime, typically between 0 to 150 ns, the plasma is hot and dense. Therefore, free-free and free-bound atomic processes tend to be present, and so both bremsstrahlung and radiative recombination continuum or broadband emission is observed. When the plasma starts cooling, during mid to late plasma lifetimes, excited atoms decay to lower energy states. At this stage line emission arises from bound-bound processes which contains useful information not only about the atomic species present but also about the plasma conditions such as plasma temperature and density.

The steel spectra of interest for this study lie within the wavelength range of 92 nm to 108 nm which contains several emission lines from a number of species present in the target sample including carbon as a trace element (in particular the C^{2+} line at 97.7 nm) and also lines from the steel matrix (in particular the Fe^{2+} lines at 98.12 and 98.4 nm). The C^{2+} line at 97.7 nm is the most sensitive carbon line in terms of signal to noise ratio and limit of detection with respect to any other lines present in the vacuum-UV range of 40 nm to 160 nm. Hence it is the most suitable for performing quantitative composition analyses of metals and alloys for their carbon content [21]. The line corresponds to the $1s^22s^2 (^1S_0) - 1s^22s2p (^1P_1)$ transition.

2.6 Analytical Figures of Merit

The Limit-of-Detection (LoD) is one of the most important figures used in analytical spectroscopy and in chemometrics. The International Union of Pure and Applied Chemistry

(IUPAC) has defined limit-of-detection as the smallest concentration of analyte in the sample that can be reliably distinguished from zero concentration. It should also be stated that, according to Association of Analytical Communities (AOAC), “the limit of detection is defined as the lowest content that can be measured with reasonable static certainty” [22]. The limit-of-detection depends on the statistical distribution of data points in a spectrum.

The gaussian distribution is used as a function to distribute the data points within the spectrum, which is mainly defined by the standard deviation σ and mean μ of the data. In terms of quantitative spectroscopic analysis, the general expression for a gaussian distribution is integrated and normalised to unity:

$$\int_{-\infty}^{+\infty} P(x, \mu, \sigma) dx = 1 \quad \text{eq. (2.37)}$$

The probability (P) of a data point lying within the integrated area is obtained by changing the limits of the integral to the values of σ , therefore by subtracting probability (P) from unity (1-P) the probability of datapoints lying outside the integrated area can also be calculated. Hence, if the standard deviation and mean from the background signal is calculated in a spectrum, the probability that a data point lies outside the normal distribution ($-\sigma \leq x \leq \sigma$) can be estimated.

The limit of confidence set by IUPAC for a particular analyte is 3σ , giving confidence level of 99.87% that the data point is the signal and not the part of background. For a typical calibration curve the intensity of the line is plotted versus the concentration of analyte. The limit of detection is given by the following:

$$LoD = \frac{3\sigma_B}{s} \quad \text{eq. (2.38)}$$

σ_B is the standard deviation of the background intensity of the sample of lowest concentration of analyte whereas s is the slope of the calibration curve.

The Limit of Quantification (LoQ) is another analytical parameter used in chemometrics and analytical spectroscopy. According to Association of Analytical Communities AOAC “the limit of quantification is the lowest amount of analyte in a sample, which can be quantitatively determined with precision and accuracy according to analyte and matrix considered” [22]. It can be computed using the equation 2.39, namely:

$$LoQ = \frac{10\sigma_B}{s} \quad \text{eq. (2.39)}$$

where σ_B is the standard deviation of the background intensity of the sample of lowest concentration of analyte whereas s is the slope of the calibration curve.

Summary

This chapter includes the basic theory and principles of laser plasmas required for the discussion of the results in this thesis. First of all, plasma definition; according to which plasma is a local assembly of atoms and/or molecules, ions and free electrons with an overall neutral electric charge. Its detailed explanation includes three essential criteria required to generate plasma.

A basic description of the main processes involved in laser ablation of matter has been given. The laser-matter interaction phase refers to the direct laser surface and the initial removal of matter into a vapour cloud via laser ablation. Various other processes involved in this phase including the laser absorption by the target material, laser plasma expansion and processes involved in atomic emission spectroscopy have been defined and outlined.

There are many processes that takes place within a laser produced plasma which facilitate the absorption, propagation and emission of radiation. Atomic processes are categorised into three main groupings or classes based on initial and final states of the electrons involved; namely bound-bound, free-bound, and free-free transitions. There are two different

mechanisms of energy transfer that underlie these processes, namely radiative and collisional. Radiative processes concern the energy transfer between photons (electromagnetic radiation) and species with the plasma whereas collisional processes are related to the transfer of energy between species within the plasma. Plasmas in complete thermodynamic equilibrium (CTE) exhibit a detailed balance between each atomic excitation and ionization process, collisional and radiative. Three essential criteria for the plasma to be in CTE are also explained in detail.

The main atomic processes, plasma parameters and equilibrium models were also discussed along with a description of the formation and expansion of laser plasmas. The techniques involved in spectral analysis are also discussed. Along with the theory, various underlying concepts of the different diagnostic techniques were also included in this chapter.

Two main methodologies are also discussed which are used to study laser produced plasmas namely, atomic absorption spectroscopy (AAS) and atomic emission spectroscopy (AES). The basic principle of AAS is that atomic and molecular species in various different states of ionization will absorb photons at discrete wavelengths. AES uses opposite mechanism where hot plasma is used as an excitation source which is essentially cooled down and then it is changed from the continuum dominated emission state to a line dominated emission state i.e. from continuum dominated state to radiative de-excitation dominated state

The limit-of-detection (LoD) is one of the most important figures used in analytical spectroscopy and in chemometrics. The International Union of Pure and Applied Chemistry (IUPAC) has defined limit-of-detection as the smallest concentration of analyte in the sample that can be reliably distinguished from zero concentration.

References

- [1] Morozov A.I. 2012. Introduction to Plasma Dynamics. CRC Press.
(ISBN:1439881332)
- [2] Carroll P.K, Kennedy E.T. 1981. Contemp. Phys. **22** pp 61-96.
- [3] Eliezer S. 2003. The Interaction of High-Power Lasers with Plasmas. (ISBN: 1420033387)
- [4] Goldston R.J, Paul H.P. 1995. Introduction to Plasma Physics, London. Inst. Phys.
(ISBN: 07503 03255)
- [5] Bittencourt J.A. 2013. Fundamentals of Plasma Physics. Springer, New York. (ISBN: 1475740301)
- [6] Chen F.F. 2012. Introduction to Plasma Physics. Springer, New York.
(ISBN:1475704594)
- [7] Russo. R. E. 1995. Appl. Spectrosc. **49** pp 14A–28A.
- [8] Singh R.K, Narayan J. 1990. Phys. Rev. B.**41** pp 8843-8859.
- [9] Scott R.H, Strasheim A. 1970. Spectrochim. Acta. Part B: At. Spect. pp 311-332.
- [10] Amoruso S, Bruzzese R, Spinelli N, Velotta R. 1999. J. Phys. B. At. Mol. Opt. Phys. **32** pp R131-R172.
- [11] Hough P, McLoughlin C, Harilal S.S, Mosnier J.P, Costello, J.T. 2010. Jour. of App. Phys. **107** Art. No. 024904 pp 1-6.
- [12] Sahai A.A. 2014. Phys. Plas. **21** Art. No. 056707.

- [13] Salzmänn D. 1998. Atomic Physics in Hot Plasmas. Oxford University Press. (ISBN: 1108318010)
- [14] Suzuki N. 2016. J. Phys. B At. Mol. Opt. Phys. **49** Art. No. 145002.
- [15] Luna H, Dardis J, Doria D, Costello J.T. 2007. Braz. J. Phys. **37** pp 1301-1305.
- [16] Chung H.K, Lee R.W, Chen M.H, Ralchenko Y. 2005. High Energy Density Phys. **1** pp 3-12
- [17] Colombant D, Tonon G.F. 1973. J. Appl. Phys. **44** pp 3524-3537.
- [18] Huddleston R. H. 1965. Plasma Diagnostic Techniques. New York, Acad. Press. (ISBN 0123591503 9780123591500).
- [19] Griem H.R. 1997. Principles of Plasma Spectroscopy. Cambridge University Press (ISBN 13: 9780521619417).
- [20] Hirsch J.S. 2003. Vacuum-UV Photoabsorption Imaging of Laser Produced Plasmas. PhD Thesis, Dublin City University, Dublin..
- [21] Lochte-Holtgreven W. 2008. Plasma Diagnostics New York: AIP (ISBN 1563963884 9781563963889).
- [22] Shrivastava A, Gupta V.B. 2011. Chron. Young Sci. **2** pp 21-25.

Chapter 3 – Experimental System Overview

3.1 Introduction

This chapter describes the experimental setups and procedures used during this doctoral project. The experimental design requirements for Vacuum Ultraviolet (VUV) LIBS are more complex than those for visible (Vis) and near infrared (NIR) LIBS. As air is a strong absorber of VUV light, a closed vacuum system is required for LIBS in VUV range [1]. In this doctoral project, a specially designed vacuum target chamber was used to hold and manipulate the target. The spectrometer (supplied by the Acton Research Corporation) and the charged coupled device (CCD) array detector (Andor Technology Ltd., Model No. DV420-BN) were also vacuum compatible [2]. In the initial course of the study, a comparison of single channel time resolved, and multichannel time integrated VUV LIBS outcomes was performed to investigate and compare the limit of detection for each case. For both time resolved and time integrated VUV LIBS, the same experimental setup and experimental conditions were used. Experiments online plasmas, created at the laser beam focus formed by a cylindrical lens, were performed with the same experimental setup. For all time integrated and time resolved VUV LIBS experiments, a Continuum Surelite model III-10 Q-switched Nd:YAG laser was used to form the plasmas.

The experimental setups for time integrated using point and line plasmas are presented in figure 3.1. Figure 3.2 shows schematic of the time resolved VUV LIBS monochromator set up. The vacuum target chamber was a simple hollow aluminium cube. Two slits were used in tandem to enable spatially resolved spectroscopy, namely a fore-slit of adjustable width which was combined with the spectrometer entrance slit [1-4]. For the experiments performed using

this experimental setup, the fore-slit was set to a measured width of 250 μm and was placed between the target and the entrance slit of the spectrometer, with which it was aligned. The spectrometer used was a vacuum compatible, 1-m normal incidence instrument, model number VM521, supplied by the Acton Research Corporation [5]. It covered the spectral range from 30 nm to 325 nm. For all time integrated measurements, a back-illuminated VUV-sensitive CCD camera was used as a multichannel detector. Each spectral slice or window captured by the full width of the CCD had a width of approximately 20 nm. For the time resolved measurements, a combination of a plastic scintillator (EJ-212) and a photomultiplier tube (R-1450) was employed as shown in figure 3.2. The detector has a time resolution of a few nanoseconds.

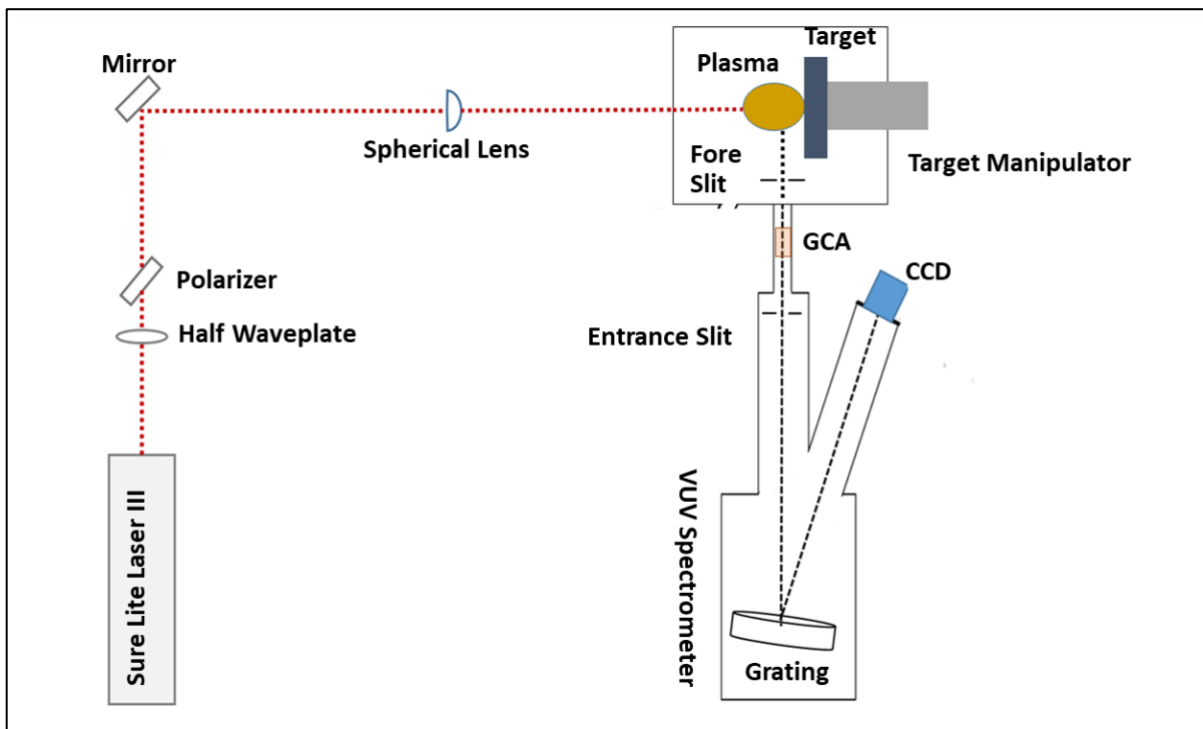


Figure 3. 1 Schematic diagram showing the VUV LIBS set up for the time integrated spectroscopy of point and line plasmas.

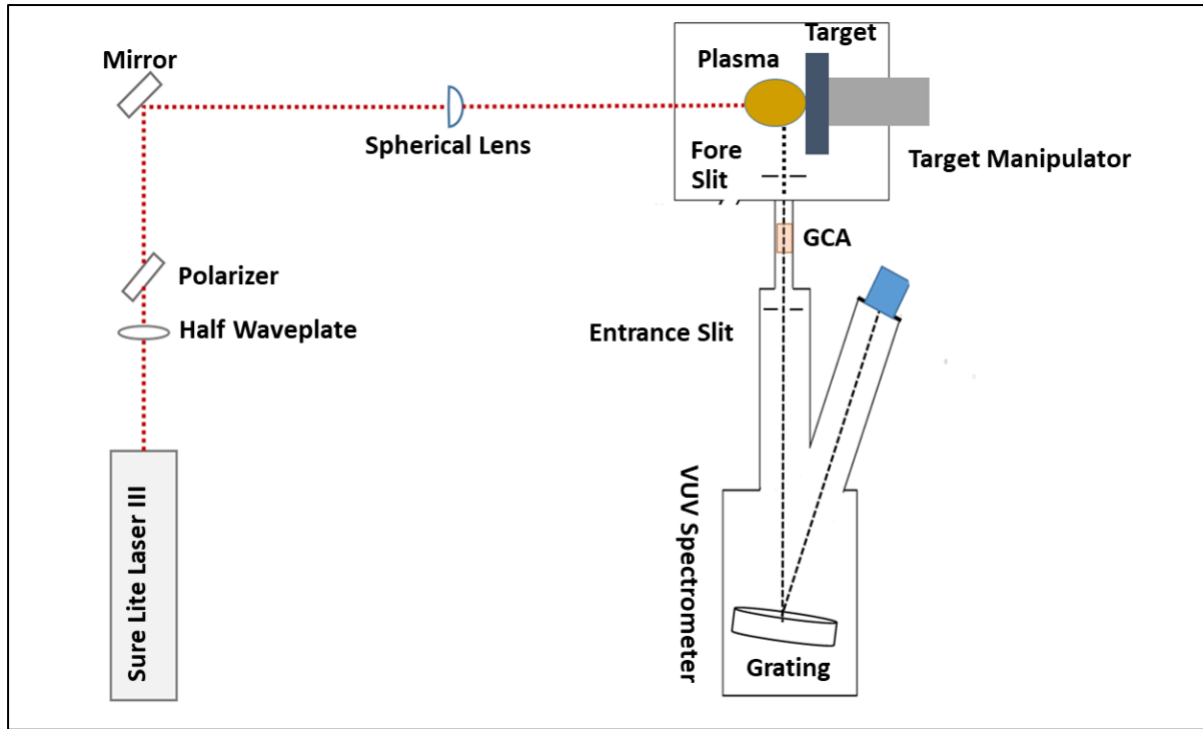


Figure 3. 2 Schematic diagram showing the time resolved VUV LIBS monochromator set up. The CCD detector is replaced by time resolved detector.

Detailed descriptions of the main sections of the VUV LIBS experimental setups are given below. These include details on the laser, target chamber, spectrometer and detectors used.

3.2 Laser System

3.2.1. Brief Description of Continuum Surelite III-10 Laser System

Plasmas were formed by focusing the output pulses from a commercial Continuum Surelite Model. III-10 Nd: YAG laser onto solid targets. It is a Class IV, Q switched laser producing linearly polarised pulses with a temporal duration of 4-6 ns (FWHM) [6]. This laser system utilises two linear flashlamps which are gas (xenon) filled in a close coupled configuration to pump the Nd: YAG laser rod. It can attain high pulse energies, of up to 650 mJ, when working at maximum output power with a 5% variation ($\pm 2.5\%$, shot-to-shot) in output pulse energy. The host laser medium is a rod (of length 115 mm and 9 mm diameter) of crystalline yttrium

aluminium garnet ($Y_2Al_2O_3$) doped with neodymium ions (Nd^{3+}), abbreviated to Nd: YAG, which gives a fundamental wavelength of 1064 nm. The laser can also operate at the 2nd, 3rd and 4th harmonic wavelengths of 532nm, 355nm and 266nm, if desired. Table 3.1 contains the main specifications of the laser system used [6].

Table 3. 1 Specifications of the Continuum Surelite III-10 Q-switched laser system

Wavelength (nm)	1064
Energy (mJ)	650 mJ (max)
FWMH (ns)	4 - 6
Repetition Rate (Hz)	From Single Shot to 10 Hz
External Trigger Jitter (ns)	≤ 1

3.2.2 Nd: YAG Laser Fundamentals.

Population inversion refers to the point in the lasing mechanism where the number of atoms of the lasing host materials in the upper lasing state exceed those in the lower lasing state. The energy level scheme for a 4 level laser system, as is the case for the Nd:YAG laser, is shown in figure 3.3. At room temperature most of the population of Nd ions resides in the ground state (E1). Intense optical pumping via one or more flashlamps (or a bank of laser diodes) excites the system from state E1 to state E4.

E4 is a short-lived state and decays rapidly to the state E3, which is the upper lasing level. This state is metastable (with a lifetime of ca. 100 μ s) and so it becomes heavily populated during the optical pumping cycle. State E2 is the lower lasing level and can decay

rapidly to state E1, thus facilitating the inversion between E3 and E2. In the absence of a Q-switch each time the population inversion reaches a value where the laser gain exceeds the optical loss (due to e.g., absorption, scattering, etc.) the laser produces a pulse (typically of duration 100 μ s or so). For pulsed operation (say 10 Hz lamps as here the output looks like a train of long pulses (duration 100 μ s or so). This is called ‘Fixed Q’ operation.

4 Level System

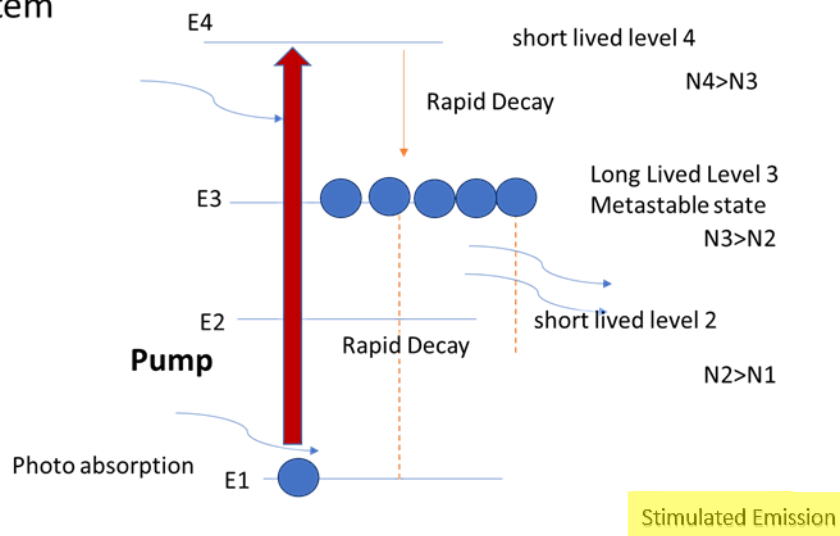


Figure 3. 3 Simplified energy level scheme for a 4 level laser system.

The principle of the Q-switched laser is that an electro-optic shutter is positioned within the laser cavity to prevent stimulated emission from occurring along the laser rod, which in turn leads to the generation of a substantial population inversion between upper and lower levels of the lasing transition. The combination of a linear polariser, Pockels cell (PC) and quarter-waveplate is known as a Q-switch figure (3.4) and effectively acts as a rapidly opening (ca. 1 ns timescale) optical shutter. The Pockels cell can change the polarisation state of light by the application of a voltage. The $\frac{1}{4}$ wave voltage converts linearly to circularly polarised light. The purpose of the Q-switch is to maintain high losses, and hence prevent laser action,

by degrading the Q factor of the resonator during the initial pumping cycles. In this way the population inversion and hence the optical gain of the lasing medium (here a Nd:YAG rod) can reach a very high value.

The Q factor is basically the quality factor of the laser cavity which is defined by the ratio of the energy stored in the cavity to the energy lost per optical cycle. When the population inversion reaches its peak, the Q factor is switched abruptly by suddenly opening the optical shutter. A few photons, generated by spontaneous emission from the Nd:YAG rod, are enough to trigger the process of stimulated emission. The population inversion is now so large that the laser gain exceeds the new (much lower) loss by a huge factor and the stored optical energy is depleted in a few passes of the optical cavity to generate a short (few nanoseconds) pulse carrying an energy of mJ's to J's (depending on the size of the laser rod and degree of optical pumping). Q switching can occur in either active or passive modes. In active mode the electro-optic gate is used whereas passive switching is achieved by means of a saturable absorber [8].

3.2.3. Continuum Surelite III-10 Optical Layout and Operation.

Referring to figure 3.4 which illustrates the Continuum Surelite optical layout, the Pockels cell is triggered when the gain saturation (maximum population inversion) has occurred in the medium. Initially no bias is applied to the Pockels cell. So, light from the laser rod will be linearly polarised by the dielectric polariser (in the horizontal plane). It passes through the quarter-waveplate where it changes to being circularly polarised and on through the Pockels cell, unaffected, to be reflected off the back mirror. The returning beam passes (unaffected) through the Pockels cell and gets another $\frac{1}{4}$ wave phase shift at the quarter-waveplate for a full $\frac{1}{2}$ wave phase shift so that it is now vertically polarised and is hence rejected by the dielectric polariser (now acting as an analyser). When a high voltage (the $\frac{1}{4}$ wave voltage, here 3600 V) is applied to the Pockels cell, horizontally polarised light, exiting the dielectric polariser will

experience $4 \times \frac{1}{4}$ wave phase shifts, so that it can pass freely up and down the full cavity, with laser light leaking out from the output coupler. Hence the Q of the cavity is switched to a high value and laser action depletes the energy stored in the laser rod rapidly to produce a so-called giant pulse (here up to 650 mJ in a pulse of duration 4 – 6 ns) at the fundamental wavelength of 1064 nm.

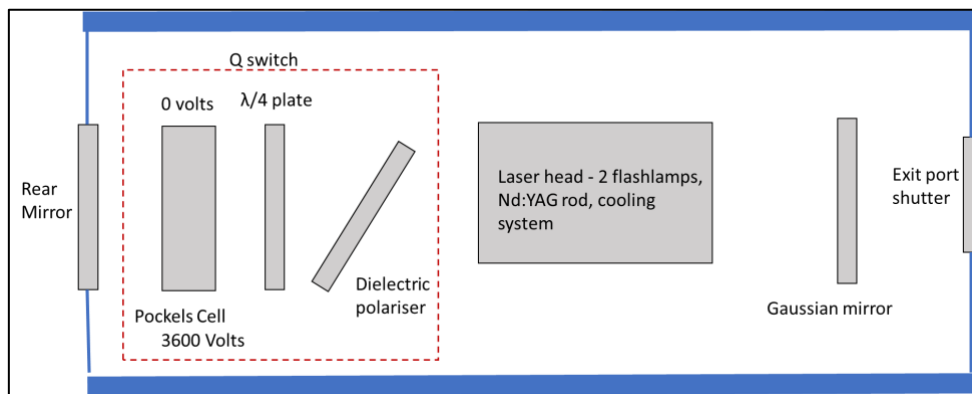


Figure 3. 4 Schematic diagram of the Q switched Surelite Nd YAG laser system.

The optical resonator or cavity is supported by graphite rods to ensure both thermal and mechanical stability. The pumping chamber houses the Nd:YAG laser rod, of length 11.5 cm and diameter 0.9 cm, and a pair of closely coupled flashlamps. The output coupling mirror has a reflectivity of 100%. A mechanical shutter (not shown on figure 3.5), which can be operated manually or in conjunction with a laser safety interlock system is located between the laser rod and Q-switch [8].

The laser can be operated at harmonics of the fundamental wavelength. Potassium dihydrogen phosphate or KDP crystals can be mounted externally to the Nd: YAG laser for this purpose. For second harmonic generation (SHG) two collinear 1064 nm beams enter KDP crystal with the same circular polarization and are combined to produce a frequency doubled beam which satisfies the usual phase matching conditions. Phase matching is achieved by angle

tuning of the KDP crystal and the resulting beam has horizontal polarization. A dichroic mirror is used to separate the fundamental beam from the harmonic. It diverts the harmonic beam to the exit port and sends the residual infrared light emanating from the KDP crystal to the beam dump. The same process of frequency addition can be used to generate higher order harmonics. For the third harmonic generation a 532 nm beam and the residual 1064 nm photon are combined to generate a 355 nm beam. The fourth Harmonic is then obtained by the combining two 532 nm beams in the non- linear crystal.

In standard operating mode at the pulse repetition rate of 10 Hz, the Pockels cell in the laser cavity triggers approximately 180 μ s after the flashlamps breakdown. This is starting delay time used when optimising the output (pulse shape, duration and energy) for the Surelite III-10 laser.

3.2.4. Synchronisation of the Continuum Surelite III-10 Laser with the Andor (DV420-BN) CCD Camera.

Pulses generated by Continuum Surelite laser systems are linearly polarized and exhibit a Gaussian (spatial) beam profile. The laser can be operated in both single shot and 10 Hz pulse repetition rate mode for different experiments. The laser was mainly used in a burst mode, with the number of individual pulses in each burst, controlled by the laser synchronization electronics. A delay-gate generator (SRS DG535) was used along with an AND gate for synchronisation of the Surelite laser with the CCD camera. All connections between the laser, DG535 and CCD camera were of the 'BNC' type. An active low TTL signal running at 10Hz with a duration of 10 μ s triggered the laser flash lamps which were permitted to run continuously so that the laser cavity could reaches a stable operating temperature. This signal was derived from the 'master clock' signal generated by SRS DG535 operating in 'internal trigger' mode and was taken from the 'T₀' output BNC terminal. A delayed version of the same

signal was taken from the 'A-B' output BNC and sent to one input of each of the dual input AND gate. The delay was set at ca. 180 μ s, corresponding to the recommended mean flashlamp to Q-switch trigger delay time.

The 'Fire' BNC output of the Andor CCD camera 'breakout box' was connected to the other input of the AND gate while the output of the AND gate was fed to the Q-switch trigger of the Continuum Surelite III-10 laser. When the Andor software issued an acquisition command (by clicking on the 'RUN' software button) a trigger pulse was sent from the computer to the CCD detector. The CCD detector, in turn, sent a TTL signal from the 'FIRE' output on the breakout box which, since it was connected to the second input of the AND gate, open that gate for the duration of the 'Fire' pulse, which was, in turn, equal to the CCD acquisition (or exposure) time. As noted above the delayed version of master clock TTL signal (with a pulse repetition frequency of 10 Hz and a pulse width of 10 μ s) input is present on the other terminal of the AND gate. Hence the Q-switch was triggered repetitively at 10 Hz so that the laser generated a burst of pulses for a period of time equal to the full exposure time, e.g., 20 pulses for an exposure time of 2 seconds. The details of laser synchronisation circuit are shown on figure 3.5 [7].

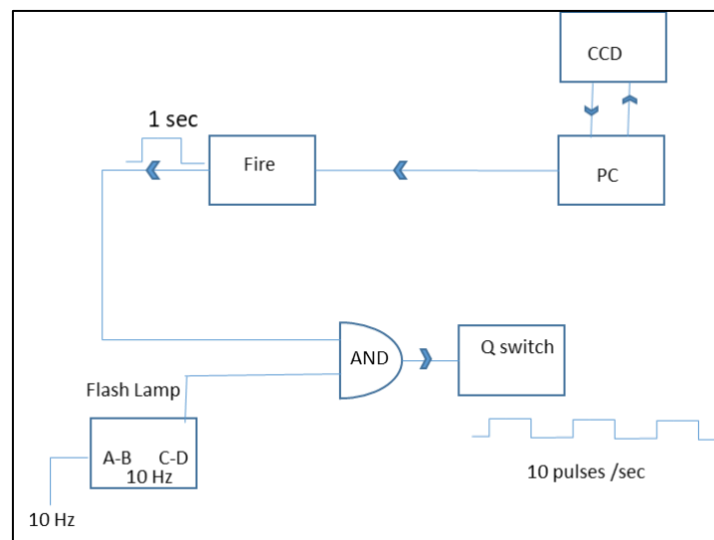


Figure 3. 5 Schematic diagram for the synchronization of the laser system and CCD.

3.3 Vacuum System and Target Chamber

3.3.1 Vacuum Pumps

It is well known that air strongly absorbs radiation in the vacuum ultraviolet (ca. 30 – 160 nm) and in the extreme ultraviolet (ca. 10 – 30 nm) spectral ranges [8]. Data from the Center for X-Ray Optics) at Lawrence Berkeley National Laboratory (CXRO) website shows that the transmission of 1 cm long air path at atmospheric pressure is effectively zero in the VUV [8]. Hence a low-pressure environment is required for the generation, transmission and spectral analysis of VUV radiation.

For the experiments carried out as part of the work reported in this thesis two vacuum pumping systems were used, one for the target chamber and one for the VUV spectrometer. Each vacuum pumping rig was comprised of a combination of a rotary pump and a turbomolecular pump. The rotary pump was used to evacuate air down to a pressure of 1×10^{-3} mbar, at which point the turbomolecular pump could be switched on. The combination could typically produce a pressure of better than 1×10^{-6} mbar for each vacuum chamber (target and spectrometer).

In order to monitor the pressure in each chamber a pair of gauges namely a Pirani and a Penning gauge was used. The Pirani sensor was used to measure pressures above 1×10^{-4} mbar and Penning sensor had a useful range of 1×10^{-4} mbar to 1×10^{-9} mbar. Although not used in this work, gas could be admitted to the target chamber and maintained at a fixed pressure via a variable gas inlet valve.

3.3.2 Target Chamber and Targets

A $12.5 \times 12.5 \times 12.5 \text{ cm}^3$ aluminium hollow cube was used as a target chamber. A series of flanges were machined in order to allow the coupling of two entrance windows (front and side),

the chamber mounting pillar and turbomolecular vacuum pump (underneath), a pair of vacuum compatible target holder-manipulators (top and side) and coupling to the VUV spectrometer, figure 3.6 [9]. All sides were polished to accommodate standard O-ring seals used to keep the system vacuum tight. The target surface was aligned with the optic axis of the full VUV spectrometer system.

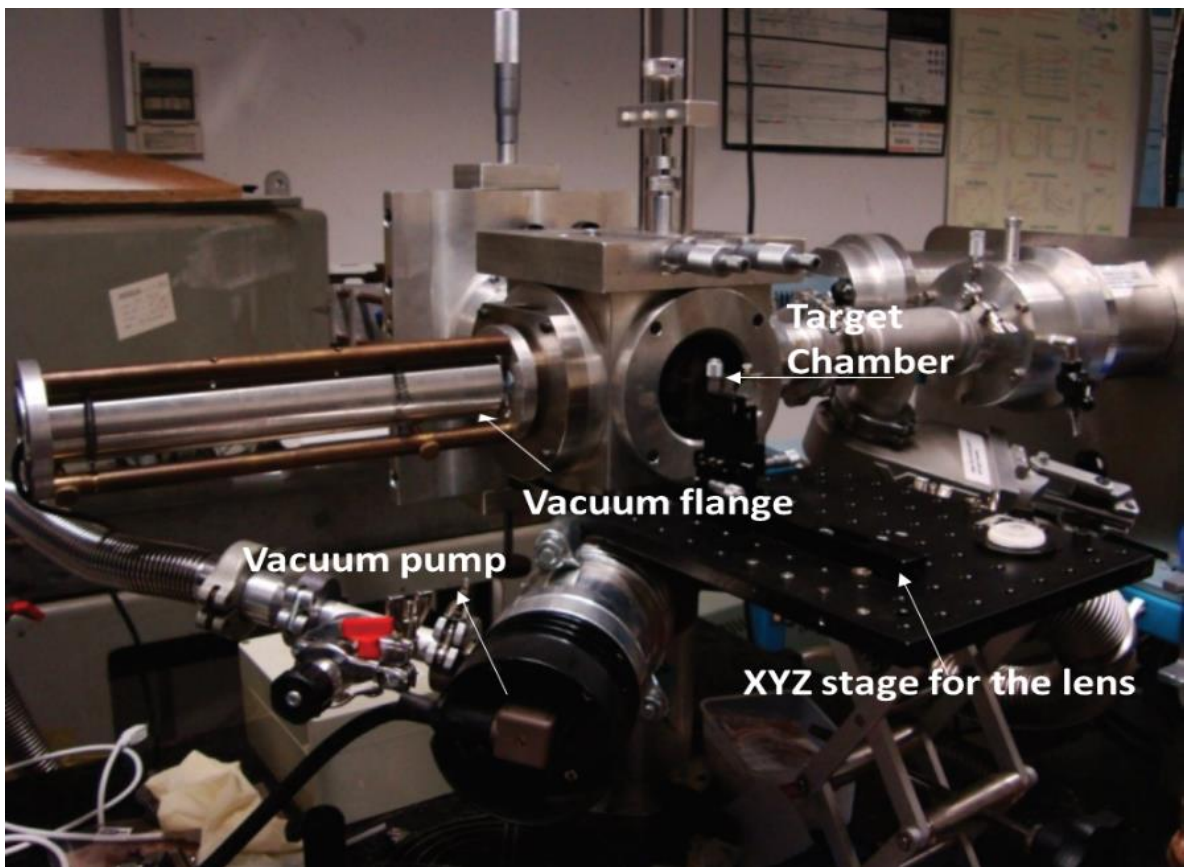


Figure 3. 6 Target chamber along with its associated vacuum and optical components.

For the alignment of the optical system, target, spectrometer (entrance slit and grating), and detector (CCD array or exit slit with VUV sensitive photomultiplier tube) a Helium-Neon (He-Ne) laser operating at its green output wavelength of 543 nm was used. It was mounted on a XYZ translational stage. The target was screwed onto a post which was in turn coupled to an o-ring sealed aluminium stage that could be moved by a pair of manual micrometer drives in

the X and Y directions. The target holder post was mounted on an o-ring sealed (Wilson seal) flange, which was in turn bolted to the aluminium plate. The post passed through a hole in that plate into the vacuum chamber. The post could be moved in z-direction via a micrometer drive so that the target could be moved in all three directions from outside the chamber without breaking the vacuum.

A wide range of (Carbon/Steel) targets, with different analyte concentrations, were purchased from Glen Spectra Reference Materials TM. For time integrated point plasma experiments and time resolved experiments, a carousel was used to mount six samples simultaneously on the aluminium stage, while maintaining the identical experimental conditions. For the line plasma experiments samples were placed in two different targets holders depending on the target size. Two different holders were also needed in order to achieve the optimum distance from the vertical line plasma to the optic axis of the spectrometer. Although there is no need for sample preparation in LIBS, in order to clean the surface, the first few pulses of the laser were used to ablate any contamination. After that step, VUV spectra were acquired.

Table 3.2 shows the list of steel samples used for carbon concentration. The concentration of the samples is provided in weight/weight ratio which is normally defined as the ratio of the solute weight to the solution weight. Here the solute is the carbon (analyte) content (in grams) and the solution is the Fe (matrix) weight (also in grams). Parts per million is the number of units of mass of a contaminant per million units of total mass.

Table 3. 2 Concentration of carbon in the various samples used

Sample	Carbon Concentration (ppm)	Sample	Carbon Concentration (ppm)
CRM 12 B 1767	520	CRM 12 A 215/3	9100
CRM 12 X 15252P	940	11 CM 5078	180
12 M BS XCCV	4400	1008 BS XAAS	410
IARM 268 B	870	CRM Fe 1/1	50
1522 BS 2932	2080	CRM 14 MI 206A	680

3.3.3 Glass Capillary Array (GCA)

A glass capillary array (GCA), positioned between the target chamber and the spectrometer, is another important part of the VUV LIBS system. The GCA permits a pressure difference between the two main parts of the vacuum system (target chamber and spectrometer) and reduced the amount of debris entering the spectrometer from the target chamber, while leaving the aperture between these two areas large enough to ensure a high level of transmission of VUV light from the plasma to the spectrometer.

A GCA is basically a glass plate with very fine holes (pores) bored in it (most often it is a bare, unprocessed, microchannel plate) and is transparent to VUV radiation with typically 50 % of normally incident radiation being transmitted. Depending on the pore size and length, GCAs are capable of maintaining up to 3 orders of magnitude pressure difference between entrance and exit faces.

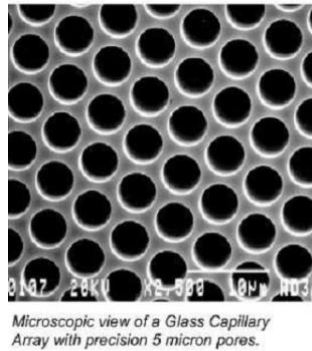


Figure 3. 7 A Glass capillary array (GCA) with 5 micron diameter pores [10].

Table 3. 3 Specifications of the GCA used for VUV LIBS

Manufacturer	Collimated Hole Inc.
Diameter	25 mm
Thickness	3 mm
Pore diameter	50 microns
Material	Lead-alkali Silicate

For these experiments a Glass Capillary Array (GCA) purchased from the Collimated Hole Inc was used. It was made from lead- alkali silicate and had a diameter of 25 mm and was 3mm thick, with a quite large pore diameter of about 50 μm (to ensure high VUV transmission while trapping large size debris particles from the laser plasma).

3.4 Spectrometer

The common type of spectrometers used for LIBS are listed below [12]:

- 1) Czerny- Turner Spectrometer
- 2) Echelle Spectrometer
- 3) Paschen Runge Spectrometer
- 4) Normal Incidence Spectrometer

A 1 m normal incidence spectrometer mount was used for all VUV LIBS experiments carried out as part of the work reported in this thesis. Details are given below.

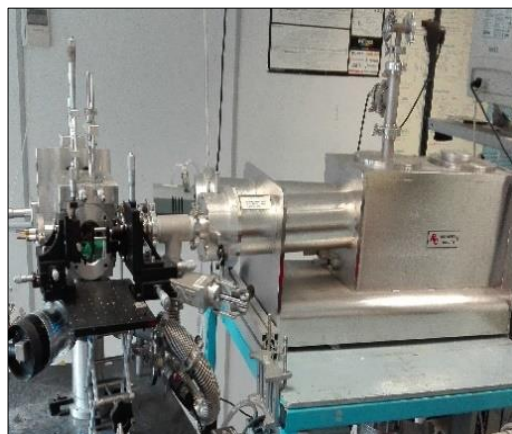
3.4.1 VM521 1m Normal Incidence Spectrometer

Experiments were carried out in the VUV spectral range and the spectrometer used for these experiments was a 1m normal incidence Acton Research Corporation VM521 spectrometer [1,2,12] which was equipped with an Al+MgF₂ coated 1200 groves/mm holographically ruled diffraction grating supplied by Bausch and Lomb. The Al/MgF₂ coating on the grating ensures enhanced reflection efficiency at VUV wavelengths.

The spectral range specified by the manufacturer went from 30 nm to 325 nm. However, for the grating used here, the spectral range extended from 35 nm to 120 nm in practice. The spectrometer, shown in figure 3.8a (top view) and figure 3.8b (side view) used a concave grating in an off-Rowland circle mount. The spectrometer uses a so-called off-Rowland mount in which the entrance slit, the exit slit and the grating all lie on a circle of diameter equal to the radius of curvature of the grating. The off-Rowland designation refers to the fact that as the grating is rotated it must also be translated so that each new wavelength remains in focus at the exit slit (or exit plane when using a CCD detector).



(a)



(b)

Figure 3. 8 Top view(a) and side view (b) of the spectrometer and target chamber.

VUV light from the plasma passes through the GCA and into the spectrometer through entrance slit. As stated above the spectrometer is comprised of only three parts, an entrance slit, a concave grating and an exit slit. If all three components are properly located on a circle with a diameter that is equal to the radius of curvature of the grating, i.e., the so-called Rowland circle [12], the entrance slit will be imaged, by the grating, onto the exit slit position for all VUV wavelengths. In effect, the concave grating combines both dispersion and focusing of the radiation that enters the spectrometer.

The grating is housed in the vacuum chamber of the spectrometer as well as both the entrance slit and exit slit. For operation as a spectrometer, the exit slit is removed and replaced by a back-illuminated CCD camera (Andor Technology, DV420-BN). With the grating sent to the zero order position both the incident and reflected radiation lie at the angle of 7.5 degrees with respect to the normal to the grating as shown in the figure 3.9.

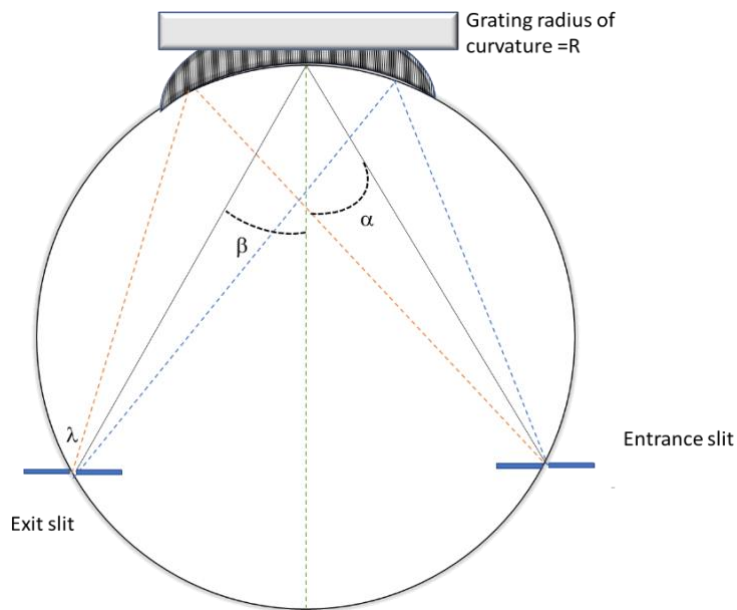


Figure 3. 9 Illustration of the Rowland circle showing entrance and exit slit locations along with the grating.

One issue that affects Rowland circle mounts is astigmatism, an optical aberration in which the horizontal and vertical foci do not coincide [11]. This problem becomes less and less

acute as the angles of incidence and reflection become smaller and smaller, i.e., they get closer to normal incidence. Therefore, this type of spectrometer faces less astigmatism than grazing incidence systems when using concave gratings. In all systems the vertical focus is optimized to obtain the sharpest possible emission lines at the exit slit or CCD detector. Minimising the astigmatism is important because with a tall enough CCD detector (or wide diameter PM tube), it could be possible to capture the whole spectrum, and hence optimise the signal-to-noise ratio of the recorded spectra. It is well established that conditions can be obtained to make a normal incidence mount almost stigmatic over a narrow spectral range by locating the light source at the so-called Sirk's focus [12,13,14,15].

Diffraction by the spherical concave grating is described by the same formula as for a plane diffraction grating:

$$\pm m\lambda = d(\sin(\alpha) - \sin(\beta)) \quad \text{eq. (3.1)}$$

where m is the spectral order (1,2, 3, ...) λ is the wavelength and d is the inter groove spacing ($d = 8.33 \times 10^{-4}$ mm for the 1200 grooves/mm grating used here). The first order light in the spectral region from 35 nm to 70 nm is free from any order overlapping problems since the reflectivity of the grating is close to zero for wavelengths below 35 nm. To change the centre wavelength on the exit slit or CCD camera, the grating is rotated and moved along a linear drive screw to refocus the system for each new wavelength range. These movements are achieved by a motor control system supplied with the spectrometer. For very fine focusing the spectrometer also has a manual (micrometer drive) control external to the spectrometer vacuum vessel.

3.5 Signal Detection and Recording System

3.5.1 Time Integrated Detector

A back illuminated (BI), VUV sensitive Andor Technology TM CCD (Charged Coupled Device) Camera (model number DV420-BN) was used for the time integrated studies. In this work, the camera was used in full vertical binned (FVB) mode to increase the signal to noise ratio of the spectra recorded. In FVB mode the charges stored in each vertical column are summed downwards along each column of pixels so that final image is one dimensional. The temperature for the back-illuminated CCD (BI-CCD) can be reduced to -80°C with a water assisted cooling system. The CCD converts photons into electronic charge packets that can be stored, transferred, digitized and processed by the associated readout and signal conditioning electronics. The CCD chip is a two-dimensional array of the Metal Oxide Semiconductor (MOS) capacitors. Each capacitor consists of a layer of silicon dioxide, grown on a silicon substrate. A positively biased metal electrode, a so-called gate is then formed on the top of the oxide layer as shown in figure 3.10.

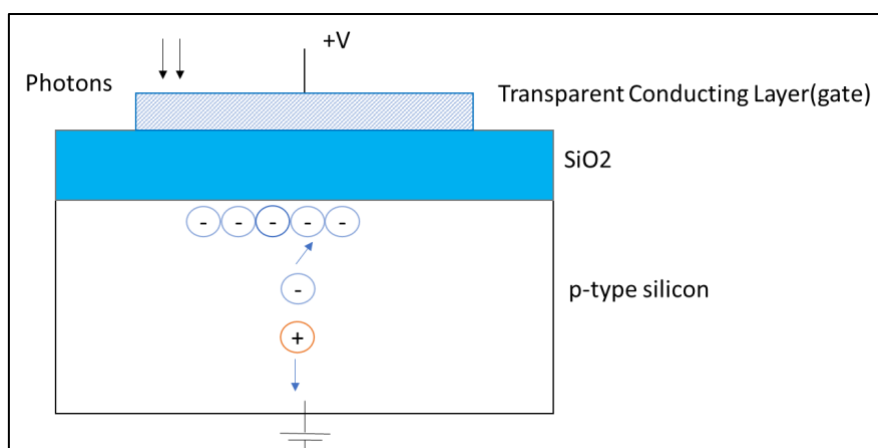


Figure 3. 10 Schematic of a MOS capacitor structure.

With the positively biased gate, photogenerated electron-hole pairs are separated and the electrons are attracted to SiO₂ surface beneath the gate. The potential well, formed below

the gate contact, is also called the depletion region since it is free from majority carriers, which are holes in p-type silicon. The amount of trapped charge in each potential well (pixel) is proportional to the total integrated light flux incident on each CCD pixel during the course of the exposure. As the integration time and or flux increases, the number of trapped electrons rises, and the depletion layer is widened. The voltage between the gate and the p type silicon is thus increased. This voltage is known as reverse bias voltage, as it is in the opposition to the original gate bias. The increment in the reverse bias voltage also increases the strength of the depletion zone electric field.

The basic layout of a CCD pixel is shown in the figure 3.11. The geometric arrangement of the pixels of the CCD is a rectangular array of dimensions 1024 pixels x 512 pixels in our case. The geometric pattern of the stored charges in the CCD pixel array represents the electronic image intensity. It is readout by shifting each row vertically downward, one by one into the shift register which is then read out sequentially. Once the pixel information in the shift register is read out, data is shifted down by another row and register is loaded up with the new data which is then read out.

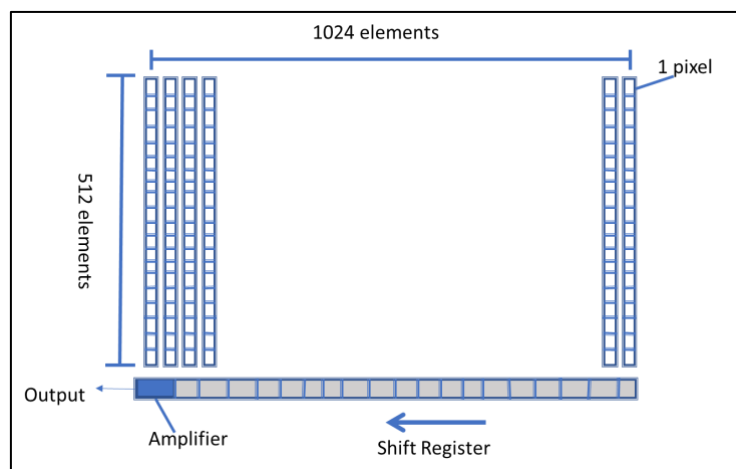


Figure 3. 11 Basic design of a CCD chip [9].

As mentioned above, in LIBS experiments for this doctoral research, the camera was used in full vertical binned mode (FVB). In FVB mode charges stored in each vertical column are summed into a final 1-dimensional (1D) image. This mode has two advantages firstly; it improves the signal to noise ratio (SNR) of the spectra obtained. The output from each pixel has two components, the signal due to the exposure to the spectral image denoted $S(p_i, p_j)$, where ' p_i ' and ' p_j ' are the coordinates of the pixel location, and the noise comprising the inherent pixel noise (mainly thermal and readout) along the quantum or photon noise in the spectral image, denoted $N(p_i, p_j)$. So the total signal is $S_T(p_i, p_j) = S(p_i, p_j) + N(p_i, p_j)$ with ' i ' the pixel index along the horizontal direction and ' j ' the corresponding index along the vertical direction. The CCD used here has ' i ' running from 1 to 1024 and ' j ' running from 1 – 512. Due to the randomly fluctuating nature of the $N(p_i, p_j)$ values, about some mean value, *taken as zero nominally here*, summing a large number of noise values will result in a large reduction in the fluctuations, approaching zero fluctuation in the limit of a large number of noise values. Assuming a Poisson (shot/quantum) noise probability distribution the noise amplitude fluctuations will be reduced by a factor of $(N)^{-1/2}$. As a result, for the CCD used here, where each vertical column has 512 pixels, by vertically binning (adding the pixel values vertically downwards), the noise fluctuation is reduced by a factor of $(512)^{-1/2} \sim 23$.

The second advantage is that it increases the readout speed by a factor of 512 (in this case) as only the remaining 1024 (horizontal) pixel values need to be read out from the CCD. In fact, one can afford to increase the readout time per pixel which is typically 8 or 16 microseconds to 32 microseconds or even higher which improves the readout noise performance (more time available for the charge to be more fully readout from each pixel as the charges are clocked out of the CCD).

The thermally generated background signals are reduced by lowering the temperature of the CCD using a thermo electric cooler. The temperature of thermoelectric camera of Andor

Technology used in these experiments can be reduced to $-80\text{ }^{\circ}\text{C}$ with the assistance of water cooling. In practice the camera was operated at a temperature of $-40\text{ }^{\circ}\text{C}$ as Khater [16] showed that there was no further significant gain in either the thermally generated background, or the noise fluctuation on that background.

In order to determine the sensitivity of the CCD camera, i.e., the number of VUV photons/count at 97.7 nm, it is necessary to know the number of photoelectrons generated per photon and the number of counts per photoelectron generated by the Andor processing electronics. So, for 97.7 nm light (photon energy $\sim 12.7\text{ eV}$), one obtains ca. 3.5 electrons/VUV photon. Extrapolating the measured sensitivity of the Andor BN-CCD [17] to the 10 eV photon energy range one obtains a sensitivity of ca. 0.02 counts/eV or ca. 0.25 counts per 12.7 eV photons or 4 photons/CCD count. Inverting, one count requires 97.7 nm photons to fall on a pixel. Taking the case of the 9100 ppm target used in this doctoral thesis. 150 spectra give rise to 100,000 counts at the peak of the 97.7 nm line and ca. 40,000 counts (background subtracted) at the half maximum. So integrating over the 11 pixels (~ 5 pixels at the FWHM) we would expect a full count of ca. 500,000. Dividing by 150 one gets 3,333 counts/single laser shot for the full 97.7 nm line which translates into $4 \times 3,333 = 13,333$ VUV photons for 4 photons/CCD count.

One final point concerns the wavelength range covered by the 1024 pixel-wide CCD. With the entrance slit width is typically set at $50\text{ }\mu\text{m}$ and noting the 1:1 magnification of the instrument, the corresponding image or ‘instrumental’ width at the focal plane is also $\sim 50\text{ }\mu\text{m}$. The reciprocal linear dispersion is 0.8 nm/mm . In the current work, the AndorTM CCD chip is 26.6 mm wide and has 1024 pixels along this axis. Therefore, the wavelength interval captured by the camera is $26.6 \times 0.8\text{ nm}$ or about 21.3 nm . Since this interval is covered by 1024 pixels, the spectral distance between pixels is about 0.021 nm . Since full vertical bin (FVB) mode is used as described above it essential that the entrance slit, grating and CCD camera are all

aligned with each other. Any misalignment can be checked by recoding a full 2D image of a spectrum that is dominated by narrow lines (e.g., Al). This was done occasionally, and no such misalignment was observed. Also, comparing horizontal lineouts with the FVB traces did not show any observable difference in line widths, indicating that broadening due to misalignment was absent.

3.5.2 Time Resolved Detector

In this doctoral research, following the time integrated VUV LIBS experiments, experiments on time resolved VUV LIBS with metal targets were performed using the same experimental setup as explained above. However, a different detector was used for time resolved VUV LIBS, as illustrated in figure 3.13. For these experiments, the BI CCD detector (used in the time integrated system) was replaced by a plastic scintillator and a photomultiplier tube (PMT).

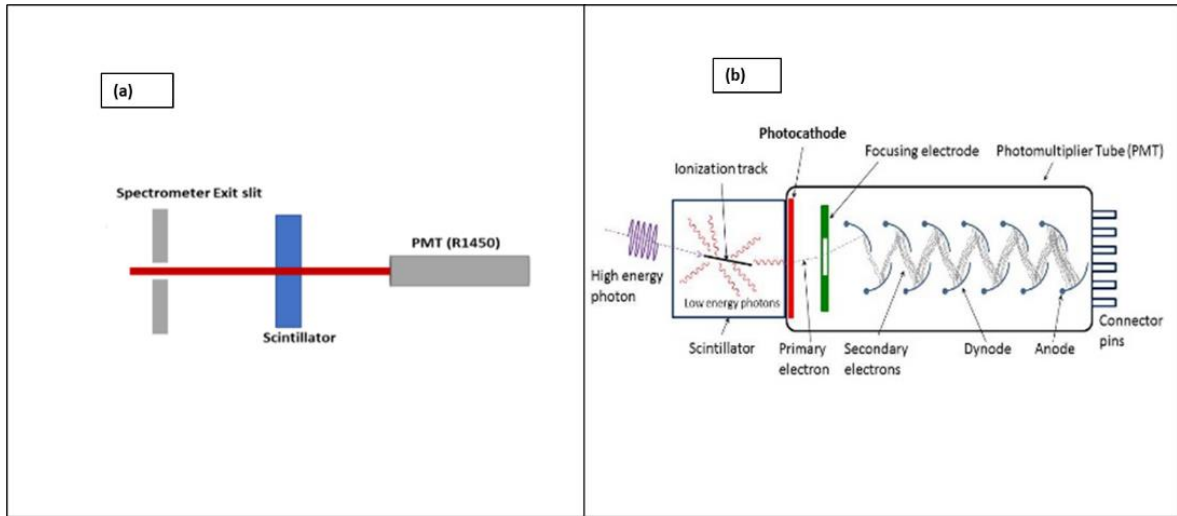


Figure 3. 12 a) Schematic diagram of time resolved detector, showing the plastic scintillator and photomultiplier tube, b) scintillation process combined with the light detection by photomultiplier tube [18].

The plastic scintillator was placed on the vacuum side of the window. EJ 212 Plastic Scintillator (Eljen technology) was used to down-convert the VUV radiation to visible light.

A fast time response photomultiplier tube (PMT) was used in combination with the scintillator. The base material used in this scintillator was Poly-Vinyl Toluene (PVT) [19]. Due to low yield of plastic material, the primary fluorescent emitter (flour) is usually suspended in the base matrix prior to the bulk polymerization which absorbs the scintillation from the base and then emits at longer wavelengths converting UV radiation from the base to the visible light which can be used by the Photo Multiplier Tube [20]. Figure 3.14 shows the emission spectrum from the EJ212 for UV irradiation.

The R-1450 is a Hamamatsu head on type photomultiplier tube (figure 3.15) with a spectral response extending from 300 to 650 nm. The EJ212 scintillator was chosen since the wavelength of its maximum emission (423 nm) is well matched to the peak sensitivity of the R1450 PMT (at 420 nm), figure 3.14.

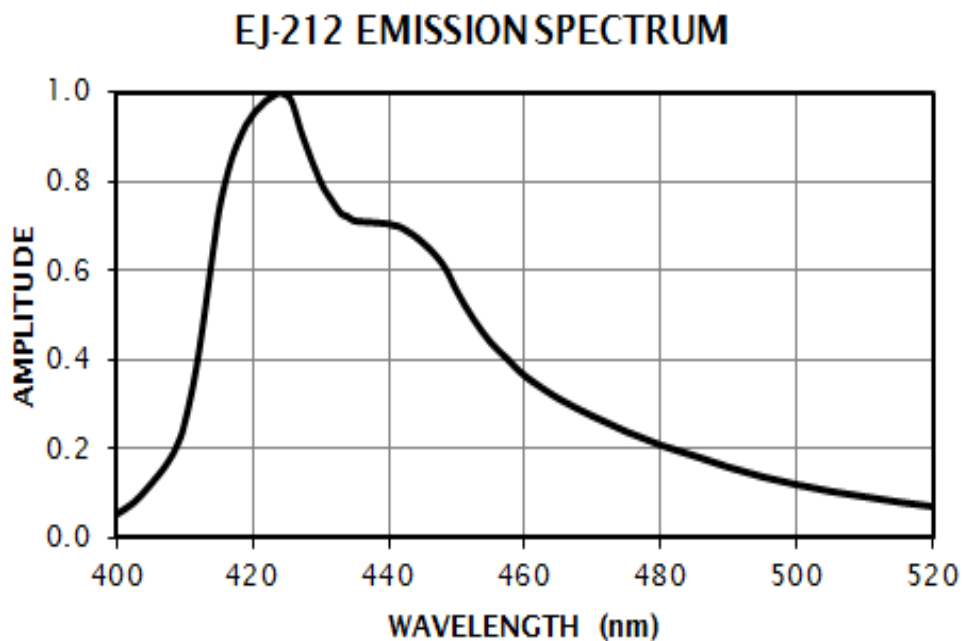


Figure 3. 13 The fluorescence spectrum of the EJ-212 scintillator [17].

The response time of the PMT was ca. 1.8 ns and the rise time of the scintillator was 0.9 ns with a decay time of 2.4 ns. The down converted visible light was delivered to the

entrance window of PMT which was placed in the atmospheric pressure (air side) of the window. The output signal from the photomultiplier tube is coupled to an oscilloscope where the measurements were recorded and stored.

For the EJ212 scintillator, the fluorescence yield is one 420 nm photon per 27 VUV incident photons. For a FWHM of 50 ns and an average PMT voltage of 50 mV across 50 ohms, the average PMT current is 1.0 mA (50 mV/50 ohms). So, the charge is $10^{-3} \text{ A} \times 50 \times 10^{-9} \text{ sec} = 5 \times 10^{-11} \text{ C}$ (or $\sim 3 \times 10^8$ electrons). The photocathode QE for the PMT is ca. 25%. Hence one gets one photoelectron per 4 x 420 nm photons. The PMT gain is 2.4×10^6 for an applied voltage $\sim 1600\text{V}$. As a result, the number of exiting electrons per incident VUV (97.7 nm) photon is:

$N_e = 0.25 \times 2,400,000/27 \sim 22,222 \text{ e- per VUV Photon}$. Hence, at 97.7nm, $Q \sim (2.2222 \times 10^4 \times 1.6 \times 10^{-19} \text{ C}) \sim 3.55 \times 10^{-15} \text{ C per VUV photon}$. From the above considerations, the measured charge for the 97.7 nm line emitted from the 9100 ppm target plasma is $1\text{mA} \times 50 \text{ ns} = 10^{-3} \text{ A} \times 50 \times 10^{-9} \text{ sec} = 5 \times 10^{-11} \text{ C}$ (or $\sim 3 \times 10^8$ electrons). Finally we obtain that the number of VUV photons $\sim (5 \times 10^{-11} \text{ C}/3.5555 \times 10^{-15} \text{ C}) = 14,060$ photons, good agreement with the 13,333 photons estimated from the VUV CCD calculation above.



Figure 3. 14 Side view of the Hamamatsu PMT model number R1450 [21].

Summary

In this chapter, the details of the equipment used in the LIBS experiments have been presented. The major features of the experimental setup included the Nd: YAG laser, the vacuum system, the spectrometer and the CCD camera are described. For all experiments a Nd: YAG (Continuum Surelite III-10) laser was used with pulse energy of up to 650 mJ, a repetition rate of 10 Hz and a wavelength of 1064 nm.

A 1 m Normal incidence (VM 521) spectrometer which was equipped with an Al+MgF₂ coated 1200 grooves/mm holographically ruled diffraction grating supplied by Bausch and Lomb was used to obtain both time integrated and time resolved VUV spectra. The spectral range of the VM521 specified by the manufacturer extended from 30 nm to 325 nm. However, for the grating used here, the spectral range extended from 35 nm to 120 nm in practice.

A back-illuminated (BI), VUV sensitive Andor Technology TM CCD (Charged Coupled Device) Camera (model number DV420-BN) was used for the time integrated studies. In this work, the camera was used in full vertical binned mode to increase the signal to noise ratio of the spectra recorded.

For the time resolved VUV LIBS, a combination of scintillator and photomultiplier tubes was used as detection system. This selection was made on the basis of efficiency and compatibility with each other. The plastic scintillator EJ 212 from Eljen technology was used in the combination of Hamamatsu photo multiplier tube (R 1450).

References

- [1] Jiang X, Hayden P, Costello J.T., Kennedy E.T. 2014. Spectrochim. Acta - Part B At. Spectrosc. **101** pp 106-113.
- [2] Khater M.A., Costello, J.T. Kennedy E.T. 2002. Applied Spectroscopy **56** pp 970-983
- [3] Radziemski L, Cremers D.A, Benelli K, Khoo C, Harris R.D. 2005. Spectrochim. Acta - Part B At. Spectrosc. **60** pp 237-248.
- [4] Jiang X, Hayden P, Laasch R, Costello J.T, Kennedy E.T. 2013. Spectrochim. Acta - Part B At. Spectrosc. **86** pp 66-74.
- [5] Register D.F, Jackson G.L, Walker S.E. 1985 Rev. Sci. Instrum. **56** p870
- [6] Continuum Surelite Pulsed Nd:YAG laser support www.photonicsolutions.co.uk .
- [7] Delaney B. 2019, Imaging and Spectroscopy of Laser Produced Annular Plasmas, PhD Thesis, Dublin city university, Dublin.
- [8] Cremers D.A, Radziemski L.J. 2006. Handbook of Laser Induced Breakdown Spectroscopy, Wiley, England, (ISBN 978-0470092996).
- [8] <http://www.cxro.lbl.gov/>.
- [9] Jiang X. 2013. Dual Pulse Laser Induced Breakdown Spectroscopy in the Vacuum Ultraviolet with Ambient Gas: Spectroscopic Analysis and Optimization of Limit of Detection of Carbon and Sulphur in Steel, PhD Thesis, Dublin City University, Dublin.
- [10] Glass Capillary Array www.idlphotonics.com.
- [11] Khater M.A. 2013. Opt. Spectrosc. **115** pp 574-90.
- [12] Thorne A. Ulf L, Sveneric J. 1999. Spectrophysics: Principles and Applications. Springer, Berlin. (ISBN 978-3540651178).

- [13] Hirsch J.S. 2003. Vacuum-UV Photoabsorption Imaging of Laser Produced Plasmas. PhD Thesis, Dublin City University, Dublin.
- [14] Hirsch J. S, Kennedy E.T, Neogi A, Costello J.T, Nicolosi P, Poletto L.2003. Rev. Sci. Instrum.**74** pp 2992-2998.
- [15] Jones B.B. 1962. App. Opt. **1** pp 239-242.
- [16] Khater M. A. 2002. Spectroscopic Investigations of Laser-Produced Steel Plasmas in the Vacuum Ultraviolet PhD thesis, Dublin City University, Dublin.
- [17] <https://andor.oxinst.com/learning/view/article/calibrated-soft-x-ray-spectrometer>
- [18] Scintillation light detecting devices SCIONIX <https://scionix.nl/read-out/>
- [19] Eljen technology plastic scintillators EJ-212 <https://eljentechnology.com>.
- [20] Wieczorek A. 2017. Development of novel plastic scintillators based on polyvinyltoluene for the hybrid J-PET/MR tomograph PhD thesis, Jagiellonian University, Krakow.
- [21] Hamamatsu photomultiplier tube R1450 <https://www.hamamatsu.com>.

Chapter 4 – Limit of Detection (LoD)

Optimization for Carbon in Steel: Point Plasma LIBS

4.1 Introduction

In this chapter, a comparison of time resolved, and time integrated VUV LIBS is presented and discussed. Quantitative VUV LIBS analysis was performed to obtain calibration curves for carbon detection in steel samples, and to determine the corresponding Limits of Detection (given in units of parts per million). The term Limit of Detection is widely used as a figure of merit and is one of the most important parameters in analytical sciences. It is the smallest concentration that can be detected with reasonable certainty for a given analytical procedure (as defined by the International Union of Pure and Applied Chemistry or IUPAC).

The main aim of the work reported in this chapter was to improve the limit of detection (LoD) for VUV LIBS by extending it into the time resolved domain. The Limit of Detection (LoD) in LIBS is defined as:

$$LoD = \frac{3\sigma}{S} \quad \text{eq. (4.1)}$$

where σ is the standard deviation of the background and S is the slope of a best fitted line to the calibration plot of line intensity versus element concentration. With known values of both the slope of the calibration curve and the standard deviation of the background signal, the final LoD value is then determined by the above equation. To benchmark limit of detection measurements using time resolved VUV LIBS, initial experiments were conducted using the existing space resolved, time integrated VUV LIBS system [1]. In this way it would be possible

to quantify any improvement in the Signal to Background Ratio (SBR) as well as the limit of detection (LoD) obtained from time resolved LIBS. All LIBS experiments were carried out using a single laser pulse for plasma generation.

4.2 Space Resolved VUV LIBS - Principle

A schematic diagram illustrating the basic concept of ‘space resolved LIBS’ is shown in figure 4.1. A so-called ‘fore-slit’ was placed between the laser plasma and the entrance slit of the spectrometer. The fore-slit width was set to 250 μm and the entrance slit width was set to 50 μm . The fore-slit was located 40 mm from the plasma and 350 mm from the entrance slit of the spectrometer. The optic axis of the spectrometer is defined as the line drawn from the entrance slit to the centre of the grating, and from the grating centre to the centre of the CCD. The fore-slit and entrance slit are centered on the optic axis of the spectrometer so that plasma radiation can pass through them and fall on the diffraction grating [2,3].

The important point is that the fore-slit defines a slice of the expanding plasma plume that can be ‘viewed’ or ‘captured’ by the spectrometer. Taking the current example consider the plasma plume to be a large ‘extended’ light source. Noting the separation between the plasma plume and the entrance slit is (350 mm + 40 mm =) 390 mm, and that the angular opening defined by the fore-slit is $\sim 0.25/350$ radians = 0.7 mrad, the width of plume viewed by the spectrometer is $(0.7 \times 10^{-3} \times 390)$ mm $\sim 275 \mu\text{m}$. To a good approximation one can state that if the entrance slit is set to a width ‘w’ the slice of plasma plume viewed by the spectrometer is $1.1 \times \text{‘w’}$. In this way spatial resolution along the plasma expansion direction, i.e., orthogonal to the entrance slit direction, is achieved.

The optic axis of the system is depicted as the blue line in figure 4.1 (a,b). The distance between the target surface and the optic axis is denoted by ‘s’ in figure 4.1(a) and typically ranges from 1 mm to 10 mm for VUV LIBS experiments. During the early stages of

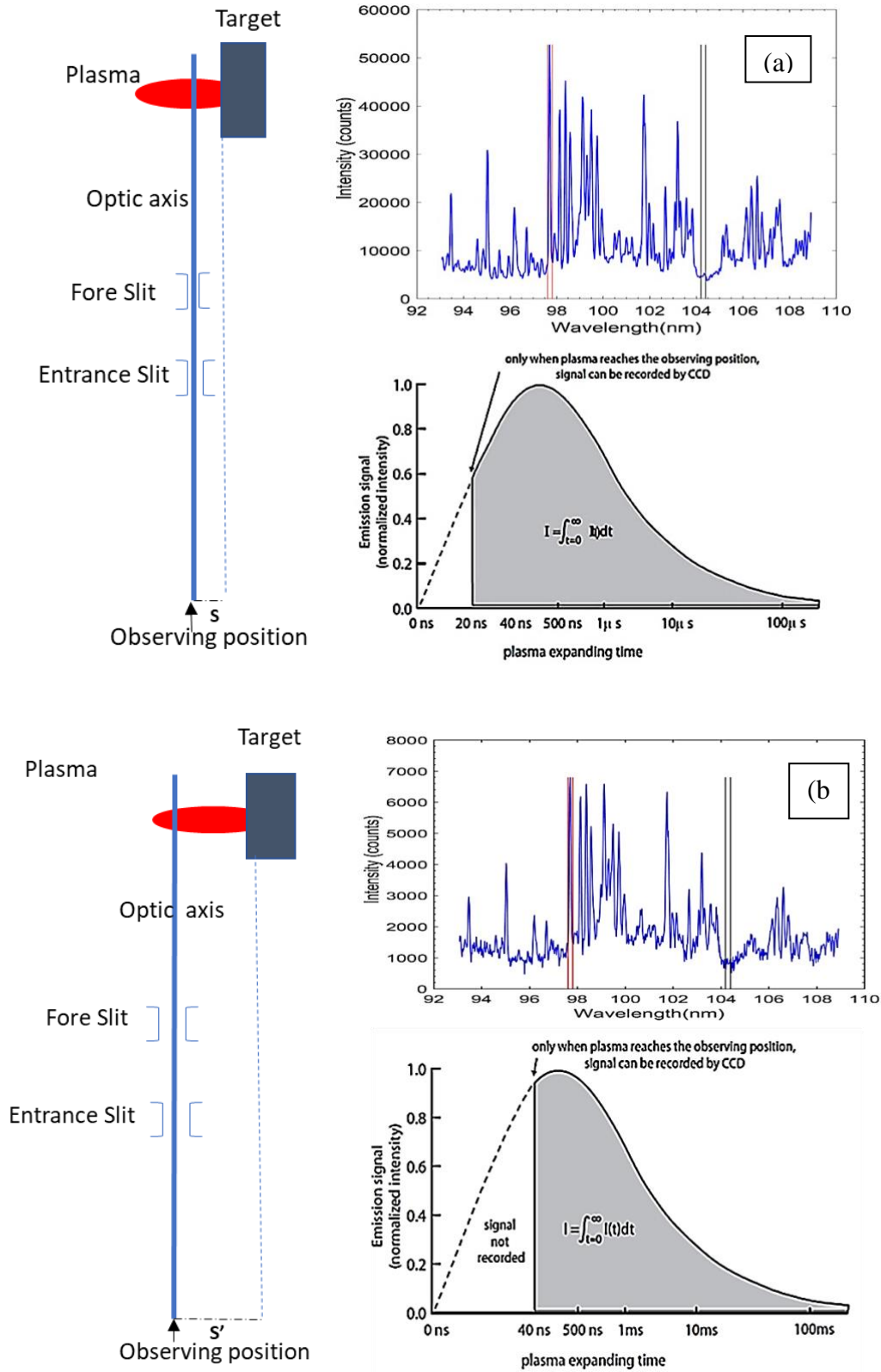


Figure 4. 1Schematic of the TISR principle and observing position of plasma ‘s’ (b) emission signal recorded at 2 mm (c) and 4mm target distance from the optic axis [1,7].

plasma formation and evolution, when the temperature and density are high, the spectral emission is comprised of mainly continuum emission, bremsstrahlung, recombination radiation. However, it should also be noted that the electron density is so high, that emission lines from bound-to-bound transitions in the hot core of the plasma will be so strongly affected by Stark broadening, that they will overlap and blend into each other. In this way they create the appearance of a continuum and add to the underlying free-free and free-bound contributions to the spectrum. Normally time gating via an ICCD is used to block out the continuum emission [3], which is present only in the early stages of the plasma evolution (typically < 500 ns) when plume is dense and hot. Here, a fore-slit is used to occlude the hot core of the plasma plume, responsible for most of the continuum signal, from the entrance slit of the spectrometer, exploiting spatial, as opposed to temporal, resolution.

In practice, for values of 's' at or below 1 mm (figure 4.1), the hot core of the plasma plume is visible to the spectrometer and a strong spectrum, sitting atop a bright broadband continuum, is usually observed. On the other hand, a very weak spectral signal, comprising discrete lines and a weak continuum pedestal, is observed when the target is pulled back from the optic axis by distances of 10 mm or more (i.e., for 's' ≥ 10 mm). Hence, by displacing the target surface by a few mm from the optic axis of the VUV spectrometer, and, using the fore-slit to occlude the core, the continuum emission can be screened out to a significant degree.

There are a couple of other points to note. The CCD detector used here is not gated and hence the VUV LIBS system is time integrating. However, since plasma plumes formed by table top lasers expand at maximum speeds of ca. 10^7 cm.s⁻¹ or 100 μ m.ns⁻¹ [4,5], there is a 'time-of-flight' before the plasma plume reaches the optic axis of the spectrometer if the target surface is displaced from it by some distance (shown as 's' in figure 4.1(a)). Consider the following scenario. If the fore-slit is located at a distance of 2 mm from the optic axis of the spectrometer (i.e., $s = 2$ mm), no emission will be recorded in first 20 ns because it will take at

least 20 ns for the plasma to expand by a distance of 2 mm and reach the optic axis of the spectrometer (blue line in figure 4.1(a,b)). Of course, in practice the plasma plume constituents (i.e., atoms and ions) will have a distribution of velocities. Therefore, different species will reach the optic axis at different times, i.e., the more highly charged ions, which predominantly emit at shorter (soft X-ray) wavelengths, will get there first, while the more lowly charged ions (which emit at longer UV and VUV wavelengths) will reach the optic axis later. Hence, although it cannot be measured with this system one would expect to see a time delay between the intensity peak of the soft X-ray emission and intensity peak of the VUV emission from these plasmas. In the same way when the target is placed further away, e.g., at 4 mm from the optic axis of the spectrometer (figure 4.1(b)), the plasma plume will take more time to reach the optic axis. Assuming a plume expansion velocity of 10^7 cm.s^{-1} , the time of flight will be 40 ns and so little or no emission would be expected to be detected before this time. An attempt to illustrate this point is made by showing these time-of-flight delays as white space up to 20 ns (figure 4.1(a)) and 40 ns (figure 4.1(b)) along the plasma expansion time axis in each case.

Another point to note is that the duration of the soft x-ray emission will be shorter than that of the VUV emission, since the more highly charged ions will be lost very quickly (on a timescale of nanoseconds) due to rapid recombination rates. On the other hand, it is known that the full duration of the emission in the VUV, coming from all VUV emitting atoms and ions in the plasma plume, can exceed 100 ns, depending on the spectral range [6]. This is borne out by the time resolved VUV measurements in chapter 5 which yield a duration of 100 ns or so for the 97.7 nm line emission.

In summary, space resolved VUV LIBS allows for some control over the amount of continuum emission admitted to the spectrometer. The optimal lateral position of the target surface can be found by observing the spectral emission in real time to obtain the best

possible (line) signal to background ratio [7] or even to obtain the maximum continuum emission if one wanted to carry out VUV photo absorption spectroscopy [8].

4.3 Choice of Laser Pulse Energy

The other experimental parameter to be adjusted to obtain the optimal limit-of-detection for VUV LIBS is the laser pulse energy (and hence irradiance or power density on target). In 2002 Khater et.al [3] showed that the 97.7 nm line emission increased monotonically with laser pulse energy in the 200 mJ to 800 mJ range. He also showed that the signal-to-background ratio (SBR) increased with laser pulse energy up to a value close to 400 mJ before it began to turn downwards. So, one can conclude that the optimal pulse energy for VUV LIBS experiments should be in the 350-450 mJ range.

A combination of half wave plate and polarizer is used to attenuate the pulse energy of Surelite laser. The laser pulse energy as a function of half wave plate angle is shown in figure 4.2(a). The relative intensity of the 97.7 nm line was measured as a function of laser pulse energy is shown in figure (4.2 (b)). For these experiments the maximum pulse energy (at the target) was 450 mJ and it was at this point that the maximum line intensity was observed. It is also clear from the figure that the line intensity follows the same trend as the laser pulse energy, as Khater observed [3].

In the figure 4.2 (c) some examples of measured spectra are shown for different pulse energies ranging from 40 mJ to 470 mJ.

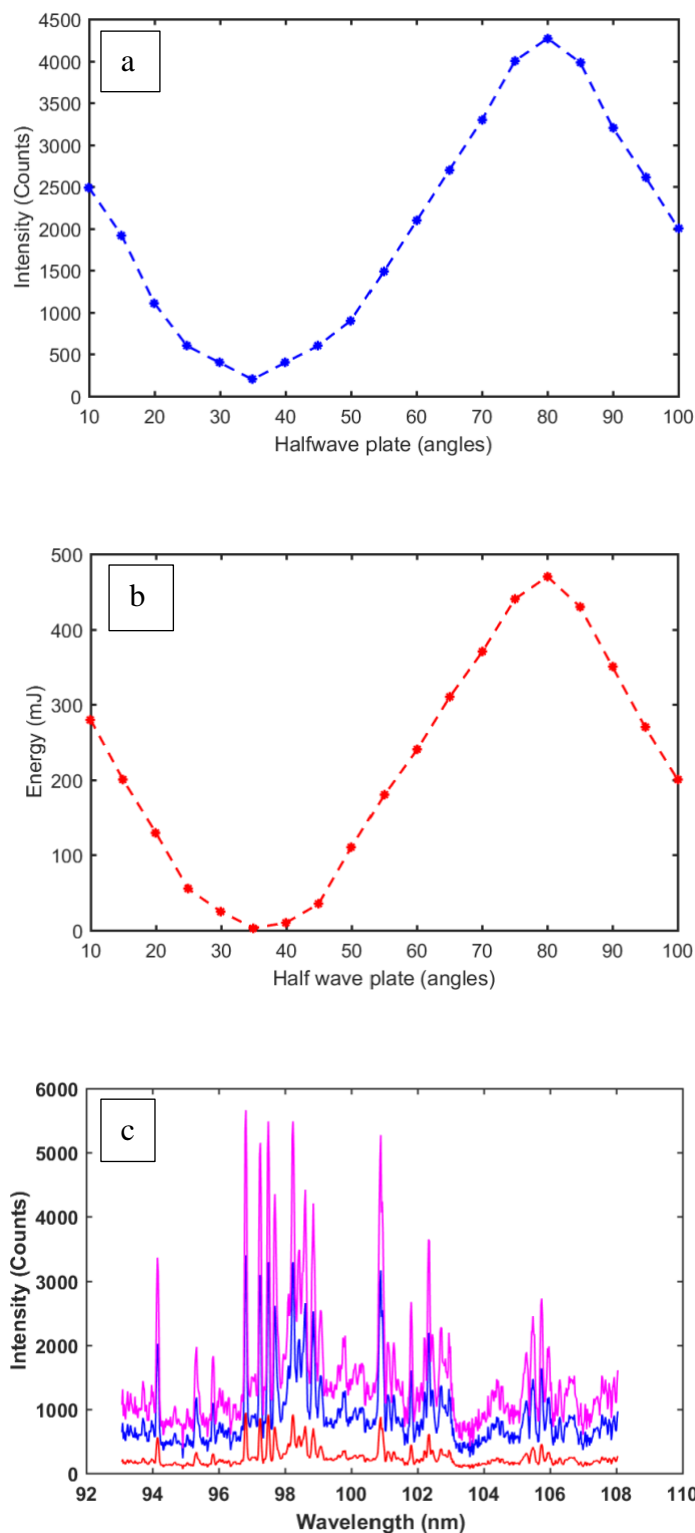


Figure 4. 2 (a) Variation in the 97.7 nm line intensity with $\frac{1}{2}$ -wave plate angular setting. (b) Variation in the laser pulse energy with $\frac{1}{2}$ -wave plate angular setting. The pulse energy was controlled by the combination of a $\frac{1}{2}$ -wave plate and polariser, the latter set orthogonal to the laser polarisation direction. (c) Examples of C-Steel spectra taken for different pulse energies.

4.4 Time Integrated Space Resolved VUV LIBS System

The target was placed at optimum distance of 2 mm and 4 mm to perform spatially resolved time of flight LIBS experiments. The Surelite III-10 laser, running at a pulse repetition rate of 10 Hz was used to generate the plasma so that a plasma was formed every 0.1 seconds and the emission signal recorded for every produced plasma. Hence during a CCD exposure time of 1 second, 10 plasmas were formed in sequence. Also, the full VUV spectral signal was recorded, from the moment the expanding plasma reached the observing position until the plasma completely decayed, as shown in the shaded regions in figure 4.1.

The number of spectra accumulated on the CCD for a laser pulse repetition frequency (f_p) of 10 Hz is directly proportional to the CCD exposure time and can be determined using the following equation:

$$N_{shots} = f_p \times T_{expo} = 10 \cdot T_{expo} . \quad \text{eq. (4.2)}$$

Where, f_p is the pulse repetition frequency (Hz) and T_{expo} is the exposure time of the CCD camera. Typically, the exposure time is set to 2 seconds (i.e., VUV spectra from 20 laser shots are accumulated in a single exposure) and 10 – 100 such exposures are made. Hence, a large number of laser shots are used to increase the signal to noise ratio for the laser plasma plume spectra recorded. However, the number of laser shots should not exceed a certain limit, typically 25 shots, on a single spot on the Fe targets in order to prevent the effect of plasma confinement and occlusion by the crater formed on the target surface.

Plasma occlusion leads to a reduction in the signal to background noise ratio for the spectra while expansion from the cratered target surface can give rise to variations in the electron temperature and density of the plasma plume, and hence the spectral distribution of the radiation emitted [9]. In the time integrated-space resolved (TI-SR) VUV LIBS experiments, the observing positions were usually set at 2 mm and 4 mm.

With a 1200 grooves/mm grating and a focal length $f = 1\text{ m}$, the reciprocal linear dispersion achieved for the spectrometer was 0.8 nm/mm . Hence the width of the spectral window captured by the 25.4 mm wide CCD camera was approximately 20 nm . Although the VUV region covered by the spectrometer ranged from 30 nm to 160 nm with the grating used, in the experiments reported in this doctoral thesis, the CIII line at 97.7 nm is the main point of interest so the spectral wavelength range extending from approximately 90 nm to 110 nm was focused on. It should be noted that spectral width captured on the CCD was reduced to ca. 16 nm due to a coating at one end of the CCD covering approximately the first 300 pixels (when in full vertical binned mode). Hence the signal yielded by these 300 pixels was not used.

Wavelength calibration of spectrometer was done manually using an existing MATLAB code. The NIST spectral database [10] was used for the identification of strong and clear emission lines (ion stage, absolute wavelength, upper and lower quantum state (term) designations, etc.) A quadratic fit was applied to the plot of wavelength vs pixel number for each spectral window captured by the CCD. In this way a wavelength calibration function could be generated for each such window. Figure 4.3 shows the spectrum obtained as counts vs pixel number while using the CCD in full vertical binned or FVB mode. Applying the corresponding fit function for that spectral window, the wavelength calibrated spectrum shown in figure 4.4 was obtained.

The laser was usually set to operate at a pulse energy of 450 mJ for all spectra shown below. The laser had good shot-to-shot stability of $\pm 2.5\%$ which could be seen from monitoring the pulse shape on a digital oscilloscope with a fast photodiode (Thorlabs, DET Series, 1 ns risetime) in conjunction with a Tektronix TDS 3032B oscilloscope. ‘Background elimination’ is performed to account for the effect of the background in each spectrum. This process is applied in order to remove the effects of any residual dark signal or continuum emission from the background. In practice a dark level signal is usually recorded before each exposure and

subtracted from the actual LIBS exposure. Hence the contribution from the thermal signal is usually just the residual noise after subtraction.

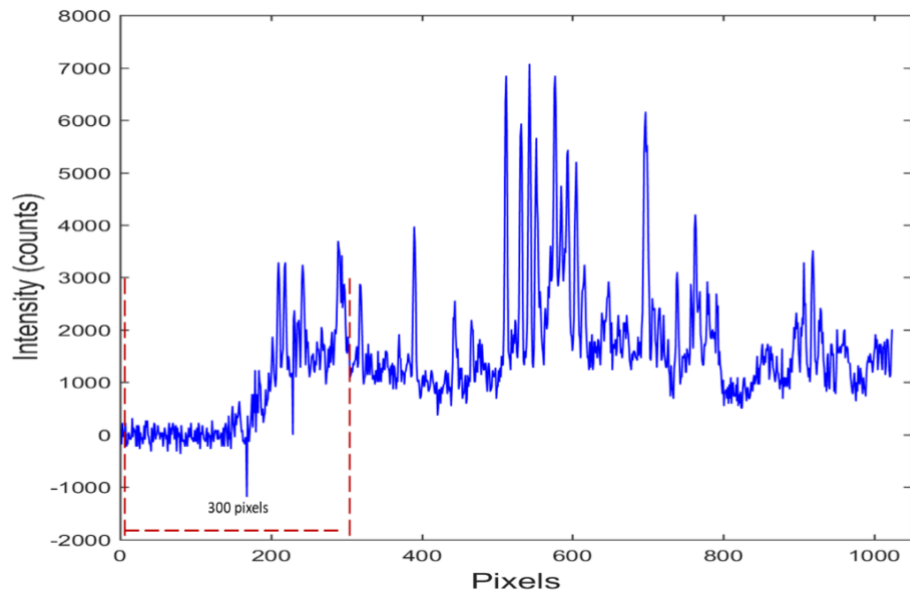


Figure 4. 3 Spectrum obtained with CCD in full vertical binned (FVB) mode.

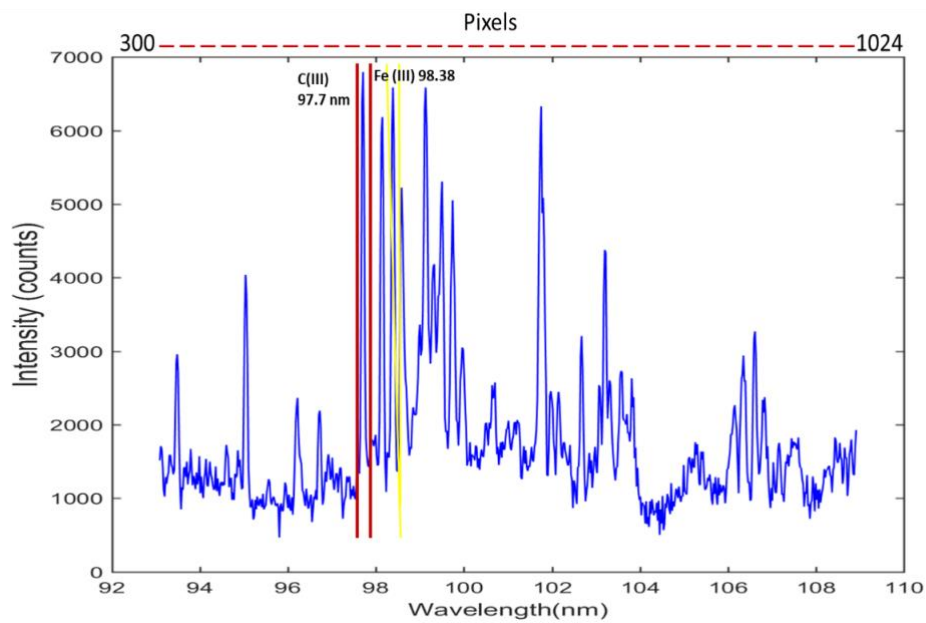


Figure 4. 4 Part of the spectrum in figure 4.3 following pixel to wavelength conversion.

Table 4. 1 Carbon and iron lines, wavelength, configuration and transition probability

Ion Stage	Wavelength	Transition	Transition Rate
C ²⁺	97.7 nm	1s ² 2s ² (¹ S ₀) - 1s ² 2s2p (¹ P ₁)	1.77 x 10 ⁹
Fe ²⁺	98.4 nm	-	-

For these experiments a water-cooled Peltier cooler attached to the sensor in the Andor BI-CCD camera helped to significantly reduce the dark signal level and the noise on that signal. The working temperature of the CCD during all the experiments performed during this work was set at -35°C. In practice, an isolated spectral line is selected as the fingerprint of the element of interest for the purposes of classification and quantification of that species, here it was the CIII 97.7 nm line. This is done in order to eliminate the influence of other lines on the measurement; therefore, the only need got background elimination is to reduce the continuum emission.

For the process of background elimination, a computer code was developed using the software package MATLAB. In practice a relatively smooth region of the spectrum, free of emission lines and near the selected line in each spectrum was chosen and the integral of the signal over a fixed number of pixels (equal to the instrumentally broadened linewidth), was taken in order to determine the background signal level. The background signal was then subtracted from the integral over the selected spectral line (with the limits of the integral covering and same number of pixels as for the background level case). In this case the signal corresponding to the integral of 11 pixels was taken as the background and subtracted from the corresponding signal obtained by integrating over 11 pixels of the selected spectral line signal.

Using this method, we obtained reasonable values of the background eliminated line intensity for the CIII line of interest in the spectra of the samples studied.

There are various studies on the defocusing effect in the single pulse mode including [11,12,13]. The single pulse defocusing effect was studied using the VUV LIBS system [11] to examine the behaviors of three spectral lines, including two trace elements in steel (C III 97.7 nm), (S V 78.6 nm) and Fe III (98.4 nm). Results showed that there is a peak on each side of the tightest focus position i.e., one maximum occurs with the beam focus located about 10 mm to 15 mm under the sample surface, while the other was observed when the beam was focused at 5 mm to 10 mm above the sample surface. A possible explanation for this observation is as follows. At the tightest focus, and hence irradiance on target, the plasma temperature could become quite large (in the say 40 – 100 eV range), so that the dominant ion stages could be significantly higher than the ion stage of interest [14] here C^{2+} . Therefore, very low VUV emission is expected in this plasma regime because the low charge states are almost absent. One way to solve the problem is to reduce the plasma temperature by reducing the power the irradiance on target,

In order to reduce the irradiance on the target one can either reduce the laser pulse energy or defocus the laser to increase the spot size. The former has the effect of reducing the plasma temperature but also the overall brightness of the plasma. Hence the latter was preferred here. When the plasma is produced by focusing the laser beam underneath the sample surface, the spot size is enlarged, the plasma temperature is lowered and can be tuned (by varying the focal spot size) in order to increase the number density of doubly charged (carbon) ions as required here.

In practice the laser pulse energy and spot size are varied until the power density is such that the plasma temperature drops to ca. 10 eV, which is optimal for the generation of excited doubly charged ions, and the radiation emitted by them. When the laser is focused above the

target surface the point with the highest power density lies above the target surface. Consequently, when the (defocused) laser ablates the surface the resulting plasma plume expands outwards, back along the incident laser direction, into the region of space where the laser focus exists. Hence a high plasma temperature can result (due to reheating of the plume by the high laser irradiance spot) resulting in emission from highly charged ions at that 'hot spot'.

4.2.1 Time Integrated VUV LIBS (Target 2 mm from the Optic axis of the Spectrometer)

The first step was to reference carbon line which could be used to both identify and quantify trace amounts of the element in the iron matrix of the steel targets used in this study. So, it was also important that the line chosen would be well isolated not just from other emission lines in the iron matrix but also from other impurity lines. It has already been established in other studies [1,7] that the C^{2+} line at 97.7 nm is an excellent candidate for this exercise. In order to have a spectrum to compare with those of the steel target spectra of carbon were recorded under the same laser and optical conditions as those for steel. Accordingly, a pure graphite sample was placed in the target holder which was located a distance of 2 mm from the spectrometer optic axis. A total of 50 shots were taken and accumulated, to obtain the spectrum shown in figure 4.5, while changing the lateral position of the target from time to time in order to avoid excessive surface/target damage and/or crater formation.

As can be seen, the spectrum exhibits a low background level and high signal to noise ratio under these conditions. The CIII line of interest, located at a wavelength of 97.7nm and corresponding to the $1s^22s2p (^1P_1)$ to $1s^22s^2 (^1S_0)$ transition, is shown enclosed in vertical red bars on the figure, Also, highlighted is the region of the spectrum free of carbon line emission around 104.4 nm.

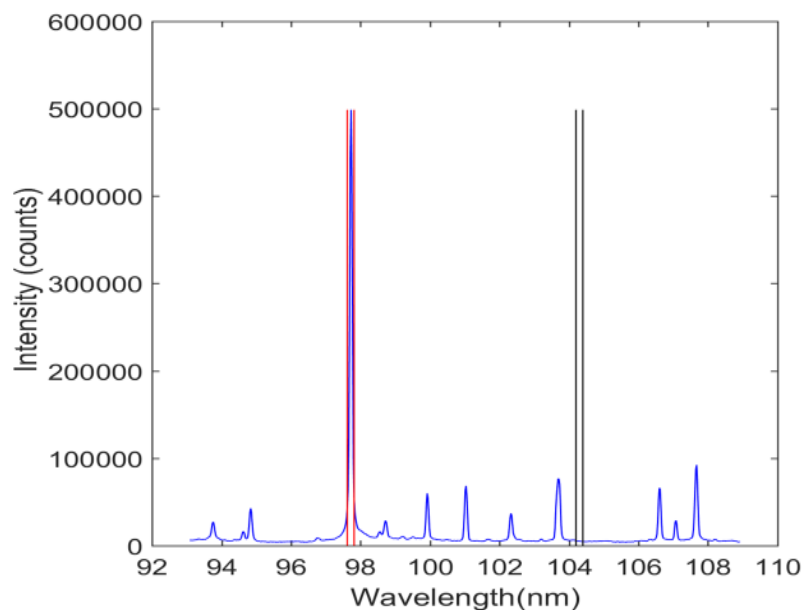


Figure 4. 5 Spectrum obtained with a pure graphite target containing a distance of 2 mm from the spectrometer optic axis. Red (vertical) bars – the 11 pixels integrated around the C III $1s^22s2p$ (1P_1) to $1s^22s^2$ (1S_0) line at 97.7 nm. Black (vertical bars)– the background was obtained by integrating 11 pixel values around 104.4 nm.

In the next experiment the graphite was replaced by a C/Fe reference target with a known concentration of carbon (2080 ppm). Locating the target at 2 mm from the optic axis of the VM521 vacuum spectrometer, a typical spectrum obtained is shown in figure 4.5. In order to calculate the signal to background ratio, the intensity values (in counts) for 11 pixels were integrated around the C III $1s^22s2p$ (1P_1) to $1s^22s^2$ (1S_0) line at 97.7 nm.

In addition, the background (continuum) level was obtained by integrating across 11 pixels the intensity values around 104.4 nm, which is a largely line free and smooth region of the spectrum. Figures (4.6- 4.9) show the average spectra for four sample targets with different carbon concentrations. Table 4.2 shows the line intensities obtained using different (C/Fe) steel targets.

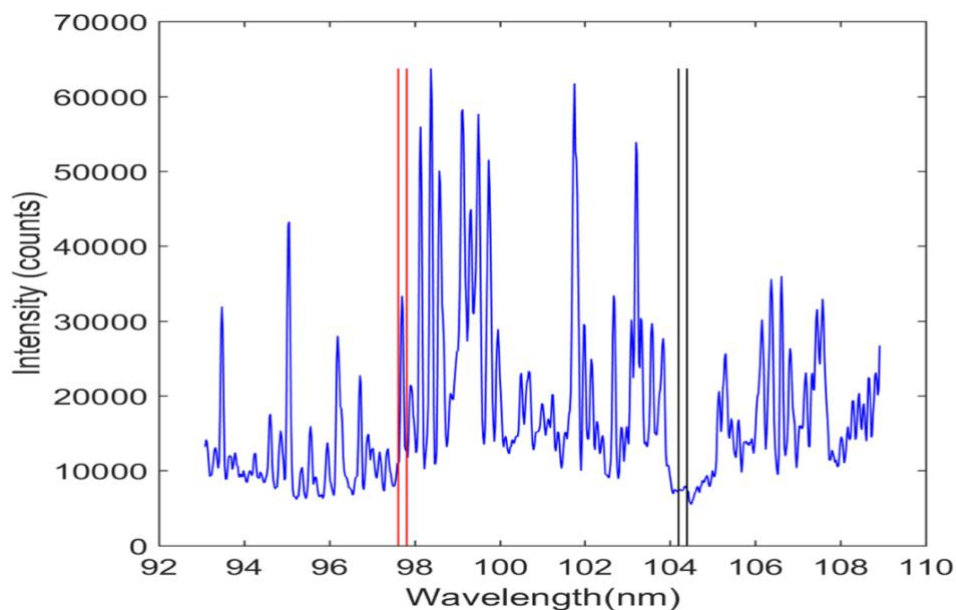


Figure 4. 6 Spectrum obtained for the reference C/Fe target (IARM 268 B) with a carbon concentration of 870 ppm placed located 2 mm from the spectrometer optic axis. Red bars – the 11 pixels integrated around the C III $1s^22s2p$ (1P_1) to $1s^22s^2$ (1S_0) line at 97.7 nm. Black bars – the background was obtained by integrating 11 pixel values around 104.4 nm.

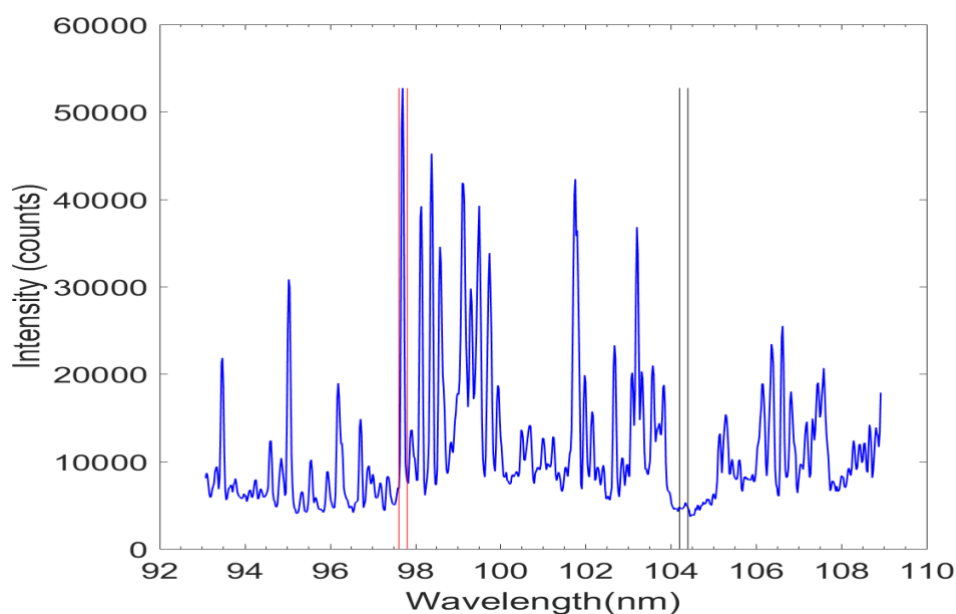


Figure 4. 7 Spectrum obtained for the reference C/Fe target (1522 BS 2932) with a carbon concentration of 2080 ppm located 2 mm from the spectrometer optic axis. Red bars – the 11 pixels integrated around the C III $1s^22s2p$ (1P_1) to $1s^22s^2$ (1S_0) line at 97.7 nm. Black bars – the background was obtained by integrating 11 pixel values around 104.4 nm.

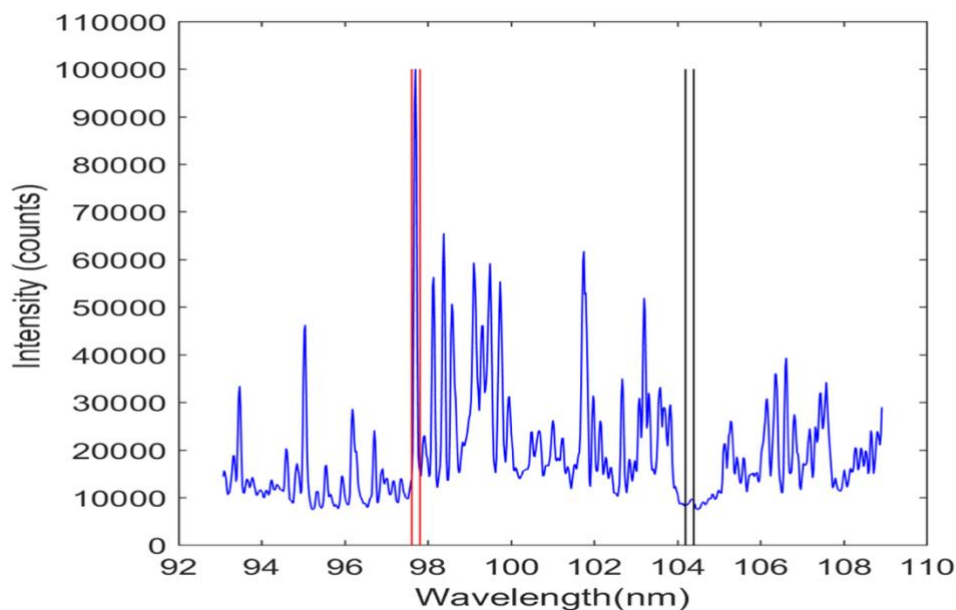


Figure 4. 8 Spectrum obtained for the reference C/Fe target (12 M BS XCCV) with a carbon concentration 4400 ppm located 2 mm distance from the spectrometer optic axis. Red bars – the 11 pixels integrated around the C III $1s^22s2p$ (1P_1) to $1s^22s^2$ (1S_0) line at 97.7 nm. Black bars – the background was obtained by integrating 11 pixel values around 104.4 nm.

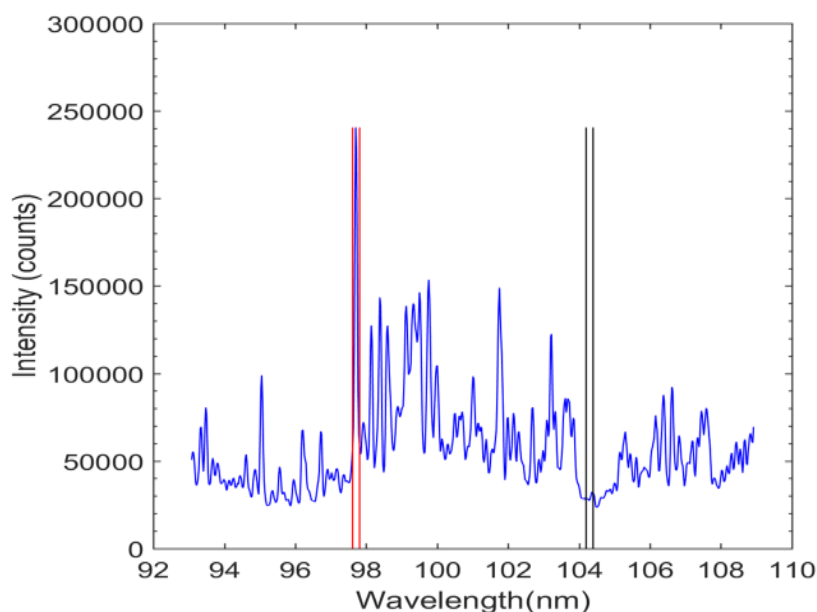


Figure 4. 9 Spectrum obtained for the reference C/Fe target (CRM 12 A 215/3) with a carbon concentration of 9100 ppm located 2 mm from the spectrometer optic axis. Red bars – the 11 pixels integrated around the C III $1s^22s2p$ (1P_1) to $1s^22s^2$ (1S_0) line at 97.7 nm. Black bars – the background was obtained by integrating 11 pixel values around 104.4 nm at 2 mm.

The regions from which the carbon line and background intensities are determined are marked by red (C III line 97.7 nm) and black (background continuum 104.4 nm) vertical lines in the figures. The general trend seen in the above spectra is that the intensity of the CIII 97.7 nm line increases with concentration from 870 ppm (reference target IARM 268 B) to 9100 ppm ((reference target CRM 12 A 215/3) table 4.2. The background subtracted intensities were obtained by the trapezoidal integration method, applied to the wavelength calibrated data, with the wavelength interval (one pixel width) being set at ca. 0.02 nm. Finally, as expected for such low carbon concentrations (and corresponding high and similar Fe concentrations) the average background continuum signal is similar in each case.

Table 4. 2 Line intensity values for the different steel samples with concentrations of 870 ppm to 9100 ppm – target located 2 mm from the optic axis

	Time Integrated LIBS -Target Location: 2 mm from the Optic axis		
Sample	Concentration (ppm)	Laser pulse energy	Line Intensity (CIII)
IARM 268 B	870	450 mJ	2.75E+03
1522 BS 2932	2080	450 mJ	4.27E+03
12 M BS XCCV	4400	450 mJ	8.24E+03
CRM 12 A 215/3	9100	450 mJ	2.22E+04

4.2.2 Time Integrated VUV LIBS (Target 4 mm from the Optic axis of the Spectrometer)

In the next experiment, the target was placed at 4 mm from the optic axis of the spectrometer. Again, typical spectra obtained from the average of 50 laser shots is shown in Figs. 4.10 - 4.13 for all four different samples. The same C III line at 97.7 nm was extracted for the line intensity

measurements and the background intensity level measurements were made in the wavelength region around 104.4 nm.

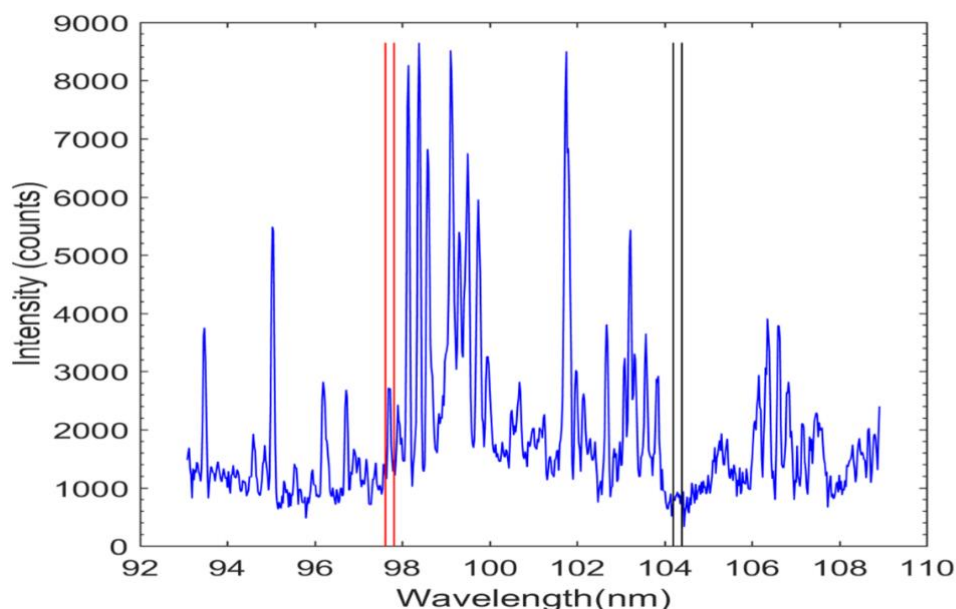


Figure 4. 10 Spectrum obtained for the reference C/Fe target (IARM 268 B) with a carbon concentration of 870 ppm at 4 mm distance from the spectrometer optic axis. Red bars – the 11 pixels integrated around the C III $1s^22s2p$ (1P_1) to $1s^22s^2$ (1S_0) line at 97.7 nm. Black bars – the background was obtained by integrating 11 pixel values around 104.4 nm.

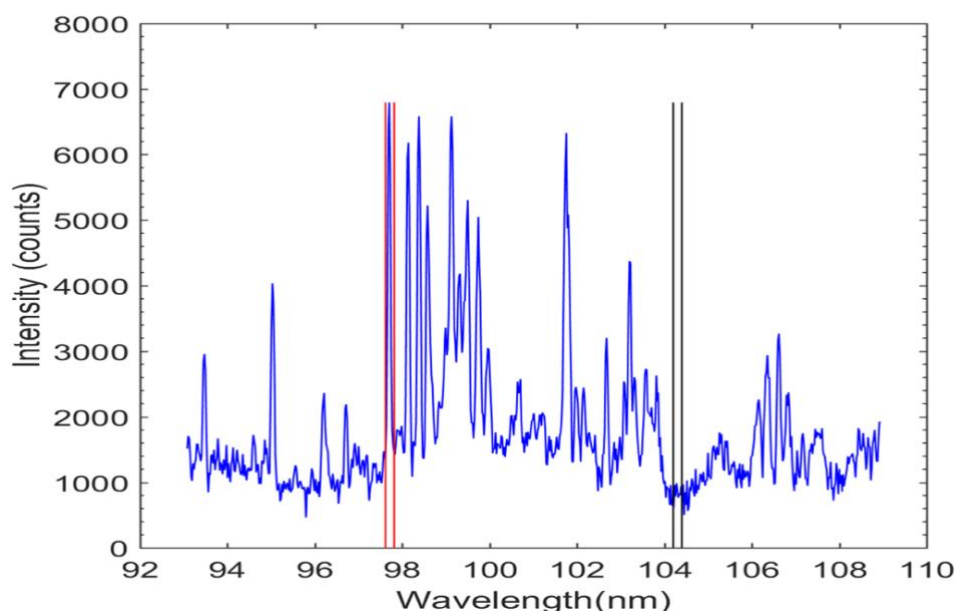


Figure 4. 11 Spectrum obtained for the reference C/Fe target (1522 BS 2932) with a carbon concentration of 2080 ppm located 4 mm from the spectrometer optic axis. Red bars – the 11 pixels integrated around the C III $1s^22s2p$ (1P_1) to $1s^22s^2$ (1S_0) line at 97.7 nm. Black bars – the background was obtained by integrating 11 pixel values around 104.4 nm.

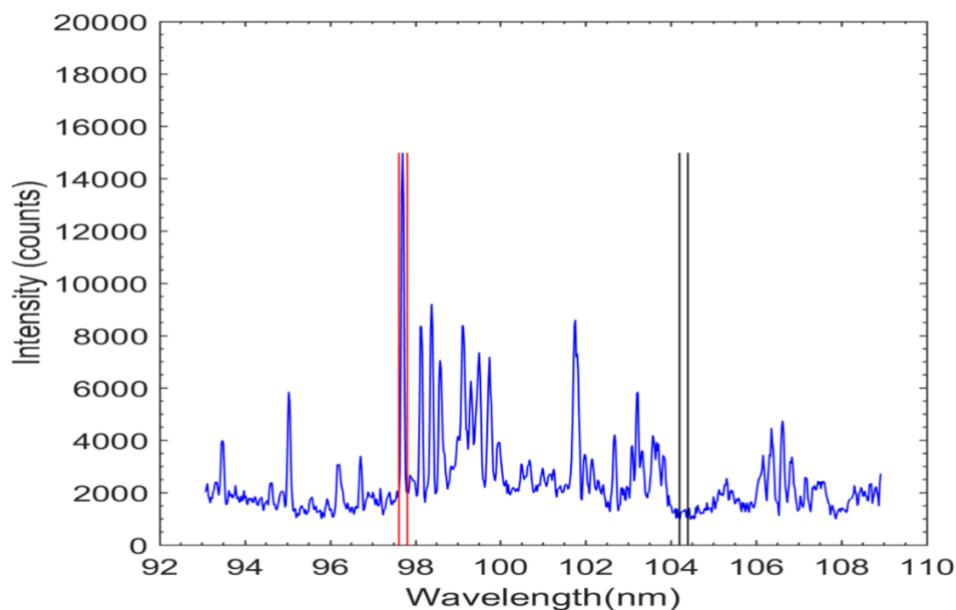


Figure 4.12 Spectrum obtained for the reference C/Fe target (12 M BS XCCV) with a carbon concentration of 4400 ppm at 4 mm distance from the spectrometer optic axis. Red bars – the 11 pixels integrated around the C III $1s^22s2p$ (1P_1) to $1s^22s^2$ (1S_0) line at 97.7 nm. Black bars – the background was obtained by integrating 11 pixel values around 104.4 nm.

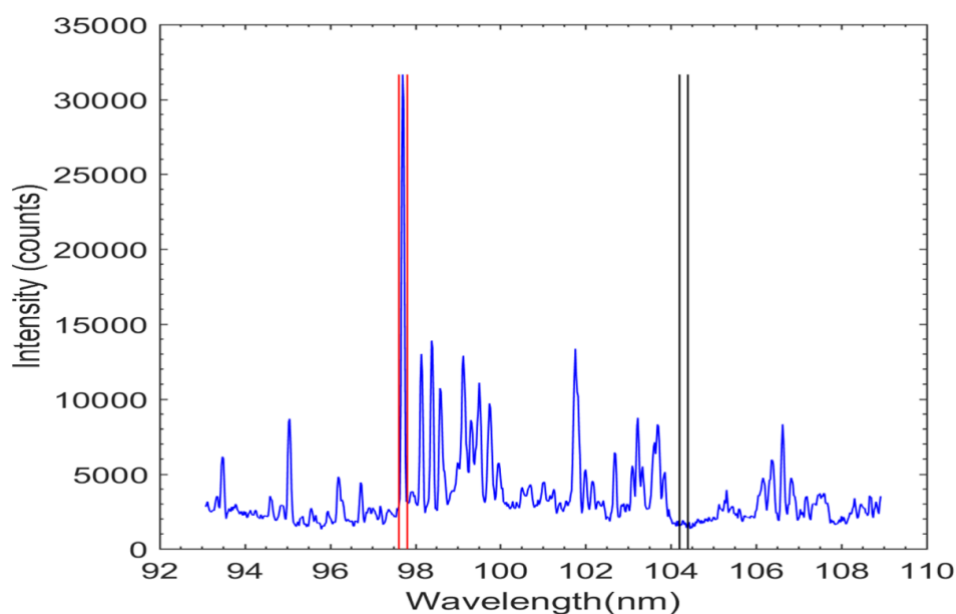


Figure 4.13 Spectrum obtained for the reference C/Fe target (CRM 12 A 215/3) with a carbon concentration of 9100 ppm at 4 mm distance from the spectrometer optic axis. Red bars – the 11 pixels integrated around the C III $1s^22s2p$ (1P_1) to $1s^22s^2$ (1S_0) line at 97.7 nm. Black bars – the background was obtained by integrating 11 pixel values around 104.4 nm.

If we compare the spectra of the lowest carbon concentration (ca. 870 ppm) C/Fe target (IARM 268 B) placed at 2 mm (figure 4.6) with the 4 mm (figure 4.10) distance from the optical distance of the spectrometer there is a drastic drop in intensity of C(III) line at the wavelength of 97.7 nm i.e., from 31122.67 to 2684.87 counts (table 4.3).

Table 4. 3 Line intensity values for the different steel samples with concentrations of 870 ppm to 9100 ppm – target located 4 mm from the optic axis

	Time Integrated LIBS - Target Location: 4 mm from the Optic axis		
	Concentration (ppm)	Laser pulse energy	Line Intensity (CIII)
IARM 268 B	870	450 mJ	2.32E+02
1522 BS 2932	2080	450 mJ	5.70E+02
12 M BS XCCV	4400	450 mJ	1.21E+03
CRM 12 A 215/3	9100	450mJ	2.67E+03

A general trend showing a significant drop in the spectral line intensity C(III) at 97.7 nm for all targets located at a distance of 4mm, in comparison with a target displacement of 2 mm, dis observed. However, spectra at the 4 mm position display a very low background signal in comparison with the spectra obtained at 2 mm, which improves the overall signal to background ratio in this case, as discussed later in section 4.4.

4.5 Time Resolved VUV LIBS

For time resolved experiments, as mentioned in section 3.1, the same laser, spectrometer setup was used, however, the back illuminated (BI) CCD was substituted by a single channel time resolved detector that was comprised of the combination of a plastic scintillator and a

photomultiplier tube (PMT). The exit slit for the VM521 spectrometer was replaced so that it was returned to operation as a monochromator. The spectral window width encompassed by the width of the exit slit was set equal to the width of 11 pixels on the CCD camera, i.e., 282 μm , so that the same signal integration took place in each case.

A scintillator was placed behind the exit slit which captured dispersed VUV radiation and converted it to light in the UV and visible region of the spectrum. The photons emitted by the scintillator, with a peak wavelength of 420 nm, were detected by the photocathode of the PMT and converted into electrons which were then amplified by the dynode chain in the PMT. The time resolved output signal from the PMT was then recorded as a voltage signal by a fast-sampling digital oscilloscope (Tektronix TDS 3032B, 300 MHz, 2.5 Giga-Samples/sec).

Initially the monochromator was set at a wavelength of 97.7 nm in order to record the time history of the CIII $1s^22s2p$ (1P_1) - $1s^22s^2$ (1S_0) line emission.

Typical output signals are shown in figure 4.14-4.17 where the signal starts after a delay of ca. 60 ns and terminates at about 230 ns. The 60 ns delay arises from the fixed pulse used to trigger the oscilloscope and appears approximately 60 ns before the optical pulse. The VUV signal persists out to a time delay of ca. 230 ns, by which time it has returned to a value close to zero volts (cf. figure 4.14). The continuum emission (figure 4.18) was obtained by setting the monochromator centre wavelength to 104.4 nm.

For the signals shown in figures 4.14 to 4.18, the target was placed at 2 mm distance from the optic axis 's' of the spectrometer for the time resolved experiments same as shown in figure 4.1, so that the line emission from the plasma for the specific wavelength of interest (here 97.7 nm) could be isolated and recorded over the full duration of VUV emission (here 230 ns). The time history of the continuum emission around 104.4 nm could also be recorded

over its full duration and subtracted from the 97.7 nm to give a fully background-subtracted and time resolved emission signal for the CIII line of interest here.

The time resolved data, recorded for all four targets, was then processed and the integral of the voltage signal around 97.7 nm obtained to determine the CIII line intensity. In the same way the integral of the signal around 104.4 nm, captured by the digital oscilloscope, was also computed, in order to obtain a measure of the background (continuum) signal. The numbers corresponding to the line and background (continuum) integrals are shown in figure 4.19 for all the target positions. The integral of each time resolved line and continuum emission signal for each spectral region, used to construct figure 4.19, was determined using a simple MATLAB code.

Figures 4.14 – 4.17 show the time resolved plasma emission at a centre wavelength of 97.7 nm for four different carbon concentrations in steel samples. Each of the traces represents the average of 50 time resolved traces with one trace obtained per individual laser shot.

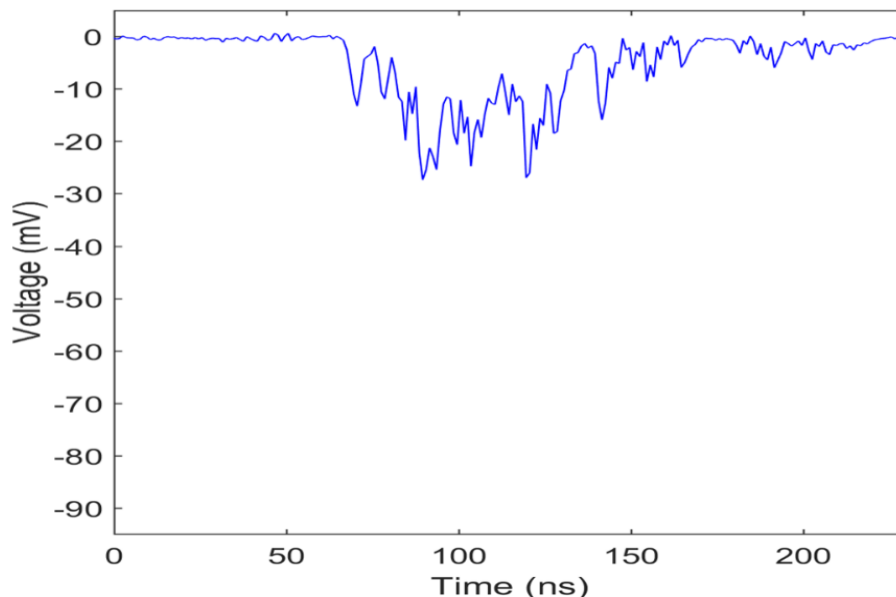


Figure 4. 14 Time resolved plasma emission at 97.7 nm for the steel target with a carbon concentration of 870 ppm located 2mm from the monochromator optic axis.

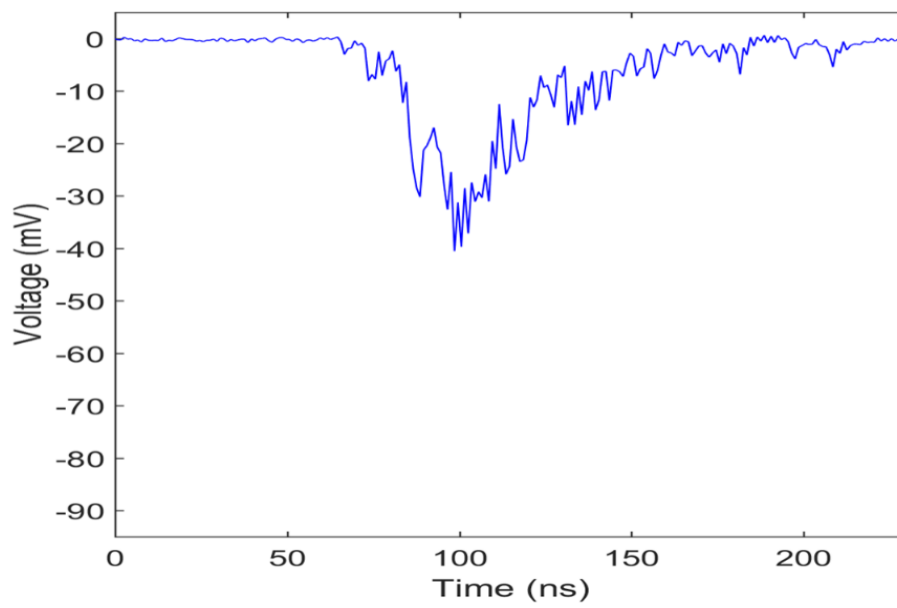


Figure 4. 15 Time resolved plasma emission at 97.7 nm for the target with a carbon concentration 2080 ppm.

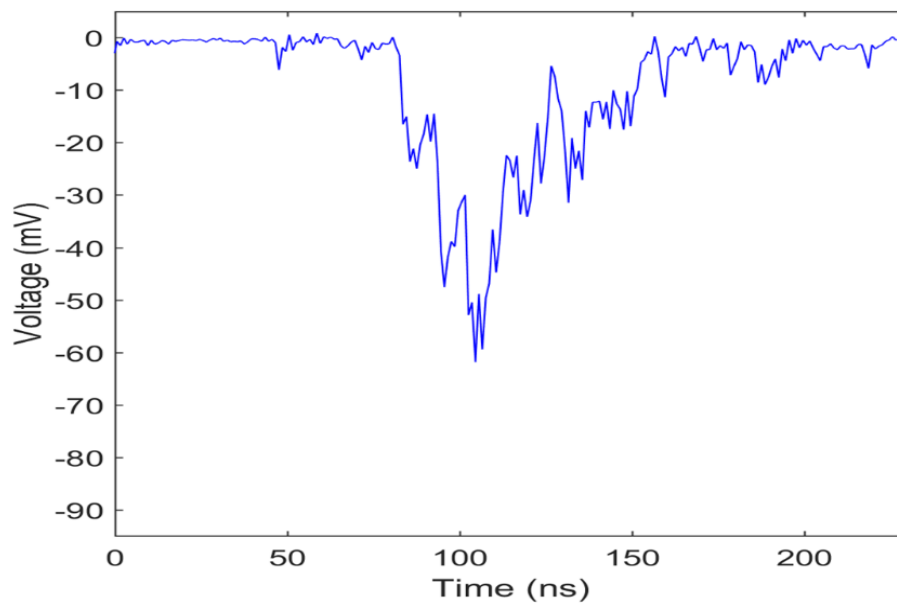


Figure 4. 16 Time resolved plasma emission for the target with a carbon concentration of 4400 ppm.

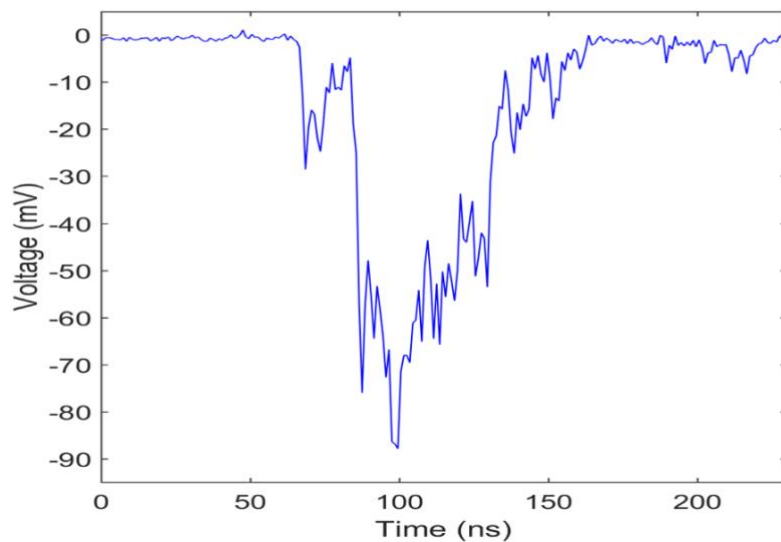


Figure 4.17 Time resolved plasma emission at 97.7 nm for the steel target with a carbon concentration of 9100 ppm.

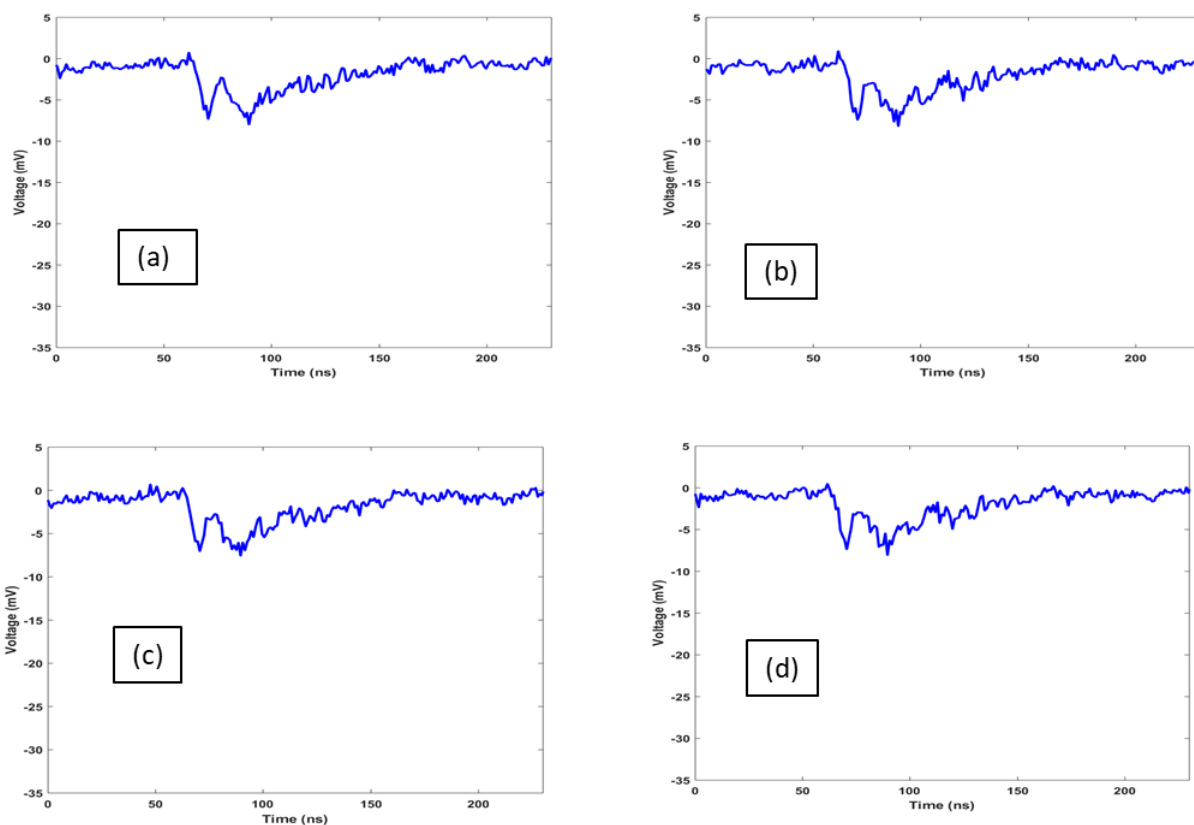


Figure 4.18 (a-d) shows the time resolved continuum emission signal for a target with a carbon concentration of 870, 2800, 4400, 9100 ppm (respectively) obtained at a monochromator wavelength of 104.4 nm.

For the background elimination from the CIII $1s^2 2s 2p (^1P_1)$ to $1s^2 2s^2 (^1S_0)$ line emission the continuum emission was also measured for every sample with the monochromator set at a wavelength of 104.4 nm. Figure 4.18 shows the continuum emission obtained for the target containing 4400 ppm C. For the calibration curve the time integral of the continuum signal is subtracted from the time integral of line signal in corresponding plots. Figure 4.19 shows the continuum and background signal for the target with carbon concentration of all four samples.

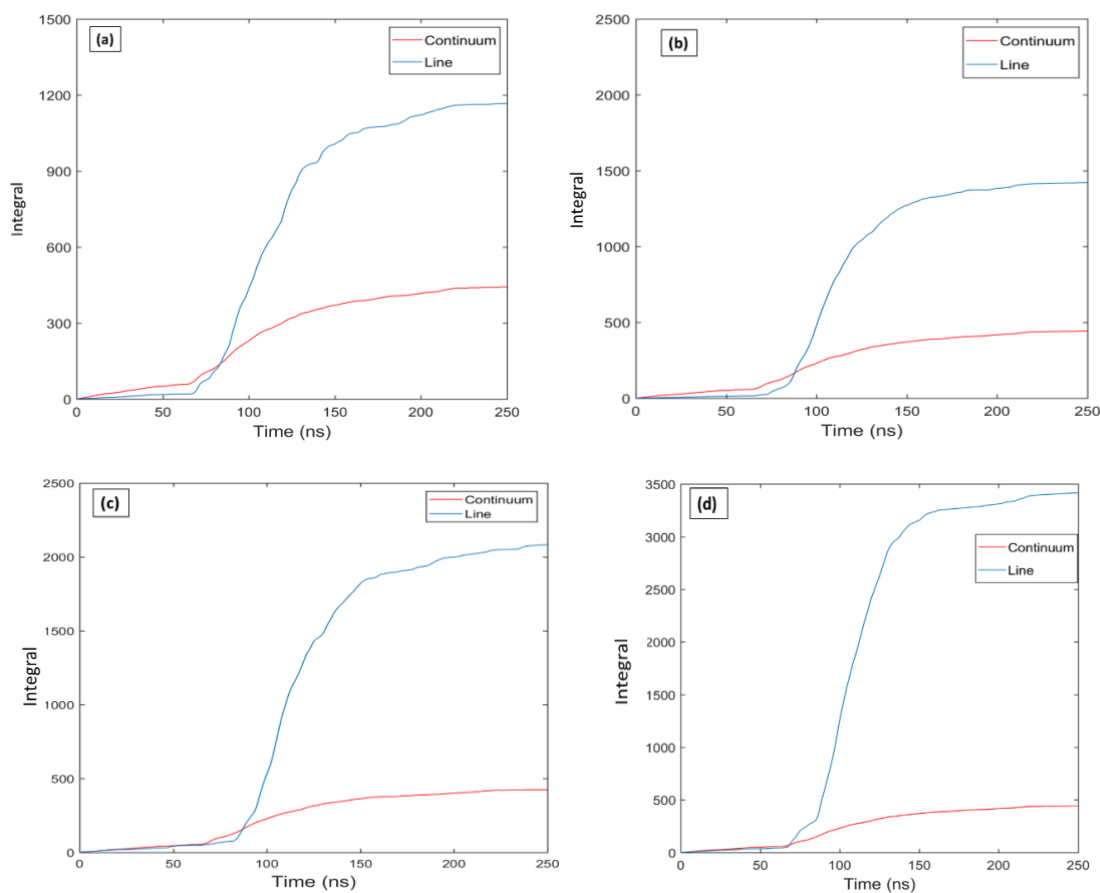


Figure 4. 19 Integral of the line and continuum signals for targets with carbon concentrations of (a) 870 ppm, (b) 2080 ppm, (c) 4400 ppm and (d) 9100 ppm.

4.6 Calibration Curves from TI-SR and Time Resolved Spectra.

Calibration curves linking carbon concentration to 97.7 nm line intensity were constructed using spectra obtained using single point plasmas with the VUV LIBS system operating in both time integrated-space resolved (TI-SR), multichannel with CCD detection mode and also in time resolved (TR), single channel with PMT detection mode. In each case the line emission signals at 97.7 nm are background subtracted using the signals recorded at 104.4 nm.

4.4.1 Time Integrated Space Resolved (TISR) LIBS Calibration Curves

i. TISR Calibration Curve (Optic axis 2 mm from the Target Surface)

With the target located 2 mm from the optic axis of the spectrometer, 50 single shot spectra were recorded for each sample, having a specific concentration. The steel sample was moved laterally in the laser focus, moving the target position by a few mm after 25 laser shots. The final spectrum in each case was obtained by averaging all 50 single spectra. The carbon concentrations varied from 870 ppm to 9100 ppm for the four targets used and the resultant, background-corrected, intensities are shown in figure 4.20 below.

The best fit straight line for the resultant calibration curve shows the data points scattered quite well on either side of the fitted line indicating that simple univariate analysis is quite well justified in this case. The estimated error on each data point arises from experimental factors (e.g., signal and background fluctuations, measurement uncertainties and systematic error) and is $\pm 10\%$ of the largest signal value. The calibration curve in figure 4.20 is based on the background subtracted values shown in table 4.2.

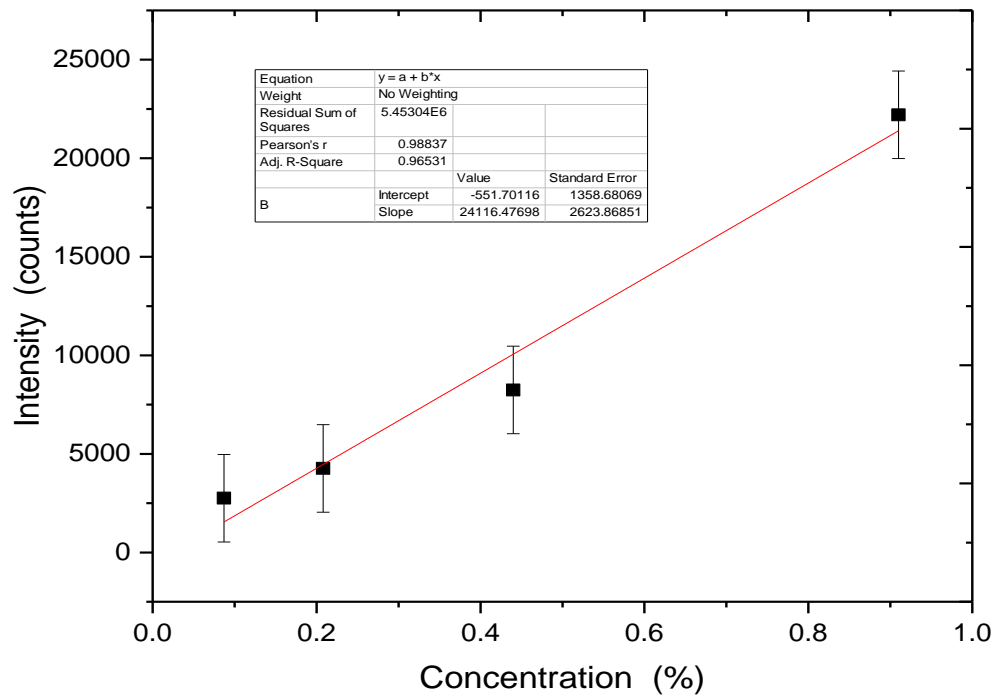


Figure 4. 20 Time integrated VUV LIBS calibration curve for spectra recorded with the target located 2 mm from spectrometer optic axis.

ii. TISR Calibration Curve (Optic axis 4 mm from the Target Surface)

With the target displaced by 4 mm from the optic axis, once again 50 single shot spectra were taken for each of the four samples. As can be seen from figure 4.21, the best fit line, passed through all the points well, a better outcome compared to the 2 mm case. The coefficient of determination (R squared value) obtained in this case is 0.9998, which helps confirm this assertion. With the target placed at 4 mm distance from the optic axis, a lower continuum level and a higher and more stable signal was observed, both of which contributed to improved results in this case compared to the results when the target was displaced by 2 mm from the optic axis.

For reference the calibration curve in figure 4.21 below is based on the background corrected line intensity values shown in table 4.3.

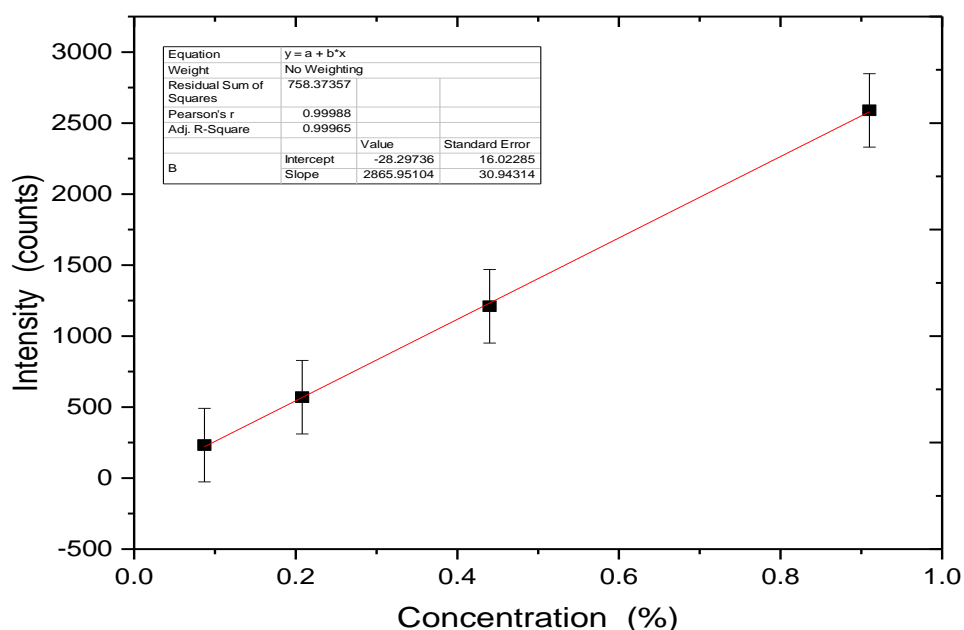


Figure 4. 21 Time integrated VUV LIBS calibration curve for spectra recorded with the target 4 mm from spectrometer optic axis.

4.4.2 Time Resolved (TR) VUV LIBS - Calibration Curves

For the time resolved measurements, each sample was irradiated by 50 laser shots and the calibration curve was constructed using the average spectral intensity obtained from the accumulation of 50 time resolved VUV traces for each sample. First all 50 traces were added and then integrated using MATLAB code. Background subtraction was performed after integration of time resolved signal by subtracting the integral of the continuum from the integrated signal using the same MATLAB software. As shown in figure 4.22 the best fit line passes well through all the data points well, showing a clearly linear relationship between intensity and concentration. The calibration curve (figure 4.22) is based on the background subtracted values given in table 4.4.

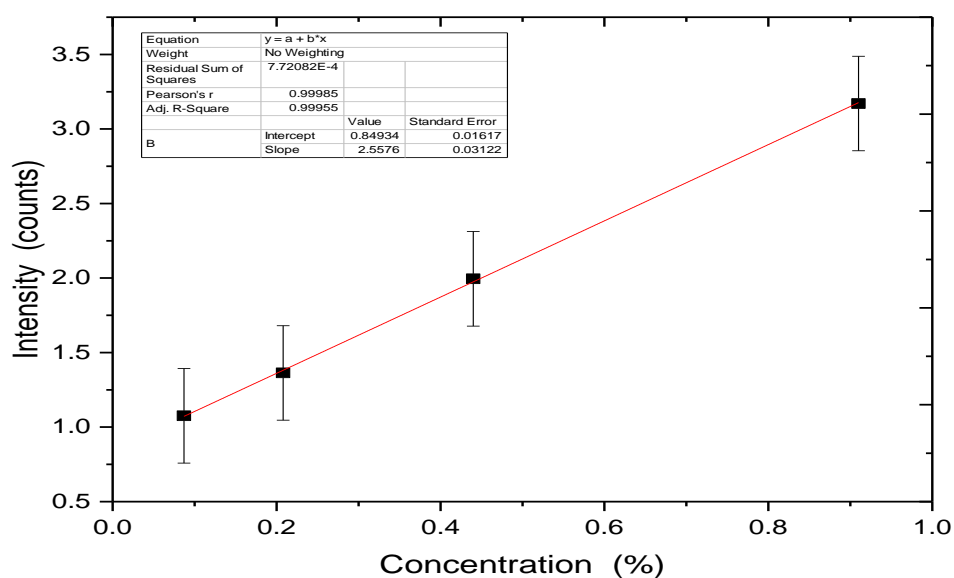


Figure 4. 22 Time resolved VUV LIBS calibration curve for spectra recorded with the target located 2 mm from spectrometer optic axis.

Table 4. 4 Line intensity values for the different steel samples with concentrations of 870 ppm to 9100 ppm – target located 2 mm from the optic axis

Time resolved LIBS - Target Location: 2 mm from the Optic axis			
Sample	Concentration (ppm)	Laser pulse Energy	Integral line emission
IARM 268 B	870	450 mJ	931.43
1522 BS 2932	2080	450mJ	1128.4
12 M BS XCCV	4400	450 mJ	1627.6
CRM 12 A 215/3	9100	450 mJ	2726

4.7 Limit of Detection Determination

The limit of detection (LoD) depends on the fluctuation in the signal with respect the background and therefore it depends strongly on the standard deviation of the background for the lowest concentration of carbon, which is 870 ppm in this case. Using the plots shown in figures 4.20 to 4.22 the slope was determined for each case, TI-SR (2 mm and 4 mm) and TR (2 mm) TR VUV LIBS.

For each case the standard deviation of the background signal at 104.4 nm was determined and hence the LOD could be extracted by using the usual formula (Chapter 2, Section 2.6), namely:

$$LoD = \frac{3\sigma}{S}$$

where ‘S’ is the slope of the calibration curve and s is the standard deviation of the background. Hence using the ratio between three times standard deviation of the background continuum values and the slope of the calibration curve, the limit of detection is determined. Table 4.5 shows that LoD value in the time resolved VUV LIBS mode was lower than for both time integrated cases (TI-SR-VUV LIBS for targets displaced by 2 mm and 4 mm). This is an important result as the optimization of LoD for carbon in steel is main aim of the work reported in this thesis.

The goodness of the linear fit is an important parameter for the determination of the quality of calibration curves. R^2 is a coefficient which takes the value between 0 to 1, and the closer it is to 1, the better is quality of the fit. For the LoD calibration, it should ideally be better than 0.97 [1,7], whereas R^2 values above 0.99 indicate a very good linear fit and are highly desirable. The R^2 values in table 4.4 show that the best linear fits to the calibration data are obtained for time integrated VUV LIBS with the target positioned 4 mm away from the optic

axis, although the limit of detection at 316 ppm is somewhat poorer than that obtained for the 2 mm target position (224 ppm). However, the latter fit, has a R^2 value just at the threshold of 0.97 and so, for that reason, the 4 mm position, which exhibits $R^2 \sim 1$ is chosen for reporting the LoD value. For the time resolved mode, with the target was displaced 2 mm from the optic axis. As a future step a systematic study of the effect of target displacement in this case will be performed.

Table 4. 5 Comparison of the analytical quality of three VUV LIBS methods used for carbon in steel

Method	R^2 Value	LoD	SBR
Time integrated space resolved VUV LIBS at 2 mm	0.975	224ppm	2.4
Time integrated space resolved VUV LIBS at 4 mm	0.99988	316ppm	2.8
Time resolved VUV LIBS	0.99985	56ppm	3.3

Hence the results from this data are considered to be more reliable (even if the LoD is higher for the TI-SR case at 4 mm). In table 4.3, the LoD obtained at 2 mm distance from the optic axis is slightly lower (at 224 ppm) than at 4 mm, which is 316 ppm. However, as the R^2 value for the data obtained at 2 mm is 0.975 compared to 0.999 (effectively 1) at 4mm, the value of the LoD obtained is considered to be more reliable for the LIBS data obtained with the target displaced by 4 mm from the optic axis of the VM521 spectrometer. This is not surprising considering the good fit of the intensity data to the fit, and albeit the the overall

reduction in counts for both the line and continuum signals results in a higher LoD, albeit once that one can have confidence in. For the time resolved case the LoD, at 56 ppm, is significantly better than both time integrated (TI-SR-VUV LIBS) cases and, given the proximity of the R^2 value to 1, one can have a high confidence in the LoD in this case.

In order to measure the improvement in the LoD by using time resolved VUV LIBS, an improvement coefficient α is introduced and defined as:

$$\alpha = \frac{LoD_{TISR}}{LoD_{TR}} \quad \text{eq. (4.3)}$$

where TI-SR and TR have the usual meanings.

Table 4. 6 Comparison of time resolved system with respect to time integrated LIBS system

α	Time integrated at 2 mm	Time Integrated at 4 mm
Time resolved at 2 mm	4.0	5.6

It is clear from the above that time resolved LIBS shows an improvement in comparison with time integrated LIBS at a corresponding target displacement of 2 mm. ~~with the α value showing that the time resolved method reduces the limit of detection by at least a factor of 4.~~

In relation to the absolute LoD values obtained with VUV LIBS system used here, it should be noted that these depend critically on a number of key system performance factors, especially the emission line signal to noise ratio (SNR) and signal to background ratio (SBR). The SNR depends in turn on the source intensity, the spectrometer (VUV) transmission/ throughput and the detector sensitivity/ noise performance. In the first version of the system, reported by Khater et al. [15], an image intensified photodiode array (IPDA) was used as the multichannel detector. The best absolute limit-of-detection (LOD) obtained for carbon in steel

was 87 ± 10 ppm. Simply changing to the current Andor BNCCD detector, the carbon/steel LoD improved dramatically to just a few ppm [3]. This example is used to illustrate the point that it is not possible to make direct comparisons of LOD values between different LIBS setups or between setups with modified detection or between measurements made with the same setup, but at quite different times [3, 11, this thesis]. The latter point is made since the VUV LIBS system performance will degrade over time. One example concerns reflectivity loss due to coating of the grating surface with vacuum pump oil. We already know that the CCD has a coating on the surface which has made part of it (an area covering ca. 300×512 pixels) completely insensitive to VUV radiation. So one can only conclude that the remaining active area suffers from at least some sensitivity loss. One can also expect a reduction in the transmission of the GCA due to plasma debris either deposition on the surface facing the plasmas. Clogging of at least some of the pores is also possible for those cases where the moving debris penetrates the GCA.

Looking at the historical trend in absolute LOD measurement performance, Jiang Xi measured a LoD of 54 ppm *in vacuo* [11]. In contrast Muhammad Khater measured 1.2 ppm (albeit in air at very low pressure 0.1 mbar) [2]. He did not measure the LOD *in vacuo*, but he mentioned a signal to background ratio that was 5 times poorer *in vacuo*. So, one can expect the LOD to lie somewhere between 5 to 10 ppm for vacuum conditions which is at least 5 times lower than when Jiang Xi performed her experiments and obtained a LOD of 54 ppm.

Using the same 97.7 nm line, under the same experimental conditions and the using the same experimental system, a LOD of 316 ppm was obtained here. So, there has been decline by a factor of approximately six in the LOD achievable with the current TI SR VUV LIBS setup since 2014 [1,7]. In summary, as the absolute LoD values depend on the quality of the LIBS optical system, the absolute values cannot be directly compared, and hence we can only look for improvements in LoD between e.g., time integrated and time resolved VUV LIBS

measured at the same time. That point noted, for completeness, a comparison with other groups performing limit of detection for carbon in steel is presented in the table 4.6 [3,11, 16-21]. In most of the studies carbon line at 190.3 nm was studied.

Table 4. 7 Comparison of limit of detection with the literature

1992	1993	1999	2000	2001	2002	2012	2019	2020
C(I)	C(I)	C(I)	C(I)	C(I)	C(III)	C(III)	C(I)	C(III)
193.09	193.09	193.09	193.09	193.09	97.7	97.7	193.09	97.7 nm
Aguilera et.al [15]	Aragon et.al[16]	Aragon et al	Strum et al	Noll et al	Khater et al	Jiang et al	V strum et al	S. Zehra et.al
65 ppm	250ppm	80 ppm	7 ppm	3 ppm	1.2ppm	3.6 ppm	34 ppm	56 ppm

Summary

Results of point plasma experiments are discussed in this chapter. For this study specifically the C^{2+} line at a wavelength of 97.7 nm was studied using standard reference targets with four different concentrations. The study includes a comparison of time resolved and time integrated LIBS methods for the limit of detection of carbon in steel. Initial experiments were based on a time integrated VUV LIBS study for targets with surface displacements of 2 mm and 4 mm from the optic axis of the spectrometer. Results show that when the target was placed at 2 mm from the optic axis of spectrometer (in time integrated LIBS mode) the limit of detection was 224 ppm while the signal to background ratio was found to be 2.4. When the target was placed at 4 mm from the optic axis of the spectrometer (again in in time integrated VUV LIBS mode) the limit of detection increased to 316 ppm with signal to background ratio of 2.8. In the case

of time resolved VUV LIBS, the limit of detection was significantly better, 56 ppm at a signal to background ratio of 3.3. It can be concluded that, time resolved VUV LIBS shows a lot of promise for the detection of carbon in steel with low LOD values.

References

- [1] Jiang X, Hayden P, Laasch R, Costello J.T, Kennedy E.T. 2013. Spectrochim. Acta Part B At. Spectrosc.**86** pp 66-74
- [2] Khater M.A. 2001. Spectroscopic Investigations of Laser-Produced Steel Plasmas in the Vacuum Ultraviolet, PhD thesis, Dublin City University, Dublin.
- [3] Khater M.A, Costello J.T, Kennedy E.T. 2002. Applied Spectroscopy **56**, pp970-983
- [4] Capitelli M, Casavola A, Colonna G, De Giacomo A. 2004. Spectrochim. Acta Part B At. Spectrosc.**59** pp 271-289.
- [5] Harilal S.S, Tillack M.S, O'shay B, Bindhu C.V, Najmabadi F. 2004. Phys. Rev. E **69** Art. No. 026413.
- [6] Zehra S. S., Costello J. T., Nicolosi P. and Hayden P. 2018. Proc. SPIE **10674** 106741H
- [7] Jiang X. 2013. Double-Pulse Laser Induced Breakdown Spectroscopy with Ambient Gas in the Vacuum Ultraviolet: Optimization of Parameters for Detection of Carbon and Sulfur in Steel, PhD thesis, Dublin City University, Dublin.
- [8] Lu H, Varvarezos L, Alli M.B, Nicolosi P, Costello J.T, Hayden P. 2020. J. Phys. B At. Mol. Opt. Phys.**53** Art. No.115001.
- [9] Yeates P, Kennedy E.T. 2011. Physics of Plasmas, **18**(6), Art. No. 063106.
- [10] Ralchenko Y, Kramida A.E. Reader J. 2008. NIST atomic spectra database. National Institute of Standards and Technology, Gaithersburg, MD.
- [11] Jiang X, Hayden P, Costello J.T, Kennedy E.T. 2014. Spectrochim. Acta - Part B At. Spectrosc.**101** pp 106-113.

- [12] Harilal S.S, Diwakar P.K, Hassanein A. 2013. Appl. Phys. Lett.**103** pp 041102-041104.
- [13] Fortes F.J, Cabalín L.M, Laserna J.J. 2008. Spectrochim. Acta - Part B At. Spectrosc. **63** pp 1191-1197.
- [14] Colombant D, Tonon G.F. 1973. J. Appl. Phys.**44** pp 3524-3537.
- [15] Khater M. A., van Kampen P., Costello J. T., Mosnier J. P., Kennedy E. T. 2000. J Phys. D: Appl. Phys. **33** pp2252-2262
- [16] Aguilera J.A, Aragon C, Campos J. 1992. Appl. Spectrosc. **46** pp 1382-1387.
- [17] Aragon C, Aguilera J.A, Campos J. 1993. Appl. Spectrosc. **47** pp 606-608.
- [18] Aragon C, Aguilera J.A, Penalba F.1999. Appl. Spectrosc. **53** pp 1259-67.
- [19] Sturm V, Peter L, Noll R. 2000. Appl. Spectrosc. **54** pp 1275-1278.
- [20] Noll R, Bette H, Brysch A, Kraushaar M, Mönch I, Peter L, Sturm V. 2001. Spectrochim. Acta - Part B At. Spectrosc. **56** pp 637-649.
- [21] Sturm V, Erben B, Fleige R, Wirz W. 2019. Opt. Express **27** pp 36855-36863.

Chapter 5 – Limit of Detection (LoD)

Optimization for Carbon in Steel: Line Plasma LIBS

5.1 Introduction

Although in principle laser induced breakdown spectroscopy is a straightforward technique, there are a variety of experimental parameters that affect its performance [1,2]. These pertain to the main components such as the laser, the focusing optics, the target shape, the spectrometer and the type of detection. Taken together there is a huge range of possible combinations which can be explored [1,2]. In this thesis, with a special focus on VUV LIBS [3,4], the laser is simplified to a device which produces pulses with a duration of a few nanoseconds, carrying energies of up to 100's of mJ. The Acton Research Corporation (ARC) VM521 normal incidence spectrometer parameters (e.g., dispersion, focal length and mount) are fixed. The targets used are all standard reference metals [4] presented to the laser as flat surfaces aligned with the optic axis of the spectrometer.

In the previous chapter, time integrated, multichannel detection, with a back illuminated CCD [5] was compared with time resolved, single channel detection, with a fast scintillator [6] and photomultiplier tube [7]. In both cases the experiments were space resolved, achieved by placing a fore-slit close to the emitting plasma. In this chapter the emphasis is on the focusing of the laser pulse onto the target surface. Specifically, the key performance parameters for LIBS [2,8], namely signal to background ratio (SBR) and limit of detection (LoD) are compared for time integrated, space resolved (TI-SR) VUV LIBS [9,10] for both point and line focus geometries [1,2,11].

Experiments on the latter are explored in detail, specifically the effect of focusing and the location of the plasma with respect to the optic axis. In these experiments a plano-convex cylindrical lens with a 1064 nm antireflection coating and a focal length of 130 mm was used. Importantly the axis of the plasma is aligned vertically, to lie along the direction of the entrance slit of the spectrometer. Combined with the near normal incidence configuration of the ARC VM521 VUV spectrometer [12,13], it can be expected that this configuration is partially stigmatic [13,14]. Hence the illuminated slit is focused onto the CCD and its full length of a few millimetres can be captured by the tall CCD. Considering the line plasma source to act like a ‘continuous array’ of point sources, one would expect, by optimising the plasma conditions, that a signal to noise ratio (SNR) gain in the recorded spectra could be achieved which, with line focus and plume region selection, could result in SBR and hence LoD gains over a single point plasma.

5.2 Effect of Laser Focus and Target Position

For these set of experiments, a plano-cylindrical lens with a focal length of 130 mm was oriented in the vertical direction such that the laser was focused onto the target surface to form a long and vertical narrow line of plasma in the corresponding direction as illustrated in figure 5.1. As a simple plano-cylindrical lens was used, focusing occurred in only one direction and the length of the line formed depended on the diameter of the laser beam. The length of plasma column so formed could then be adjusted by controlling the diameter of the laser beam. This was done by placing an aperture (an adjustable iris) in the beam before it was incident on the lens. The effect of defocusing and of the absolute target position with respect to the optic axis of the spectrometer were both important parameters to be varied and optimised to obtain the best possible LoD values.

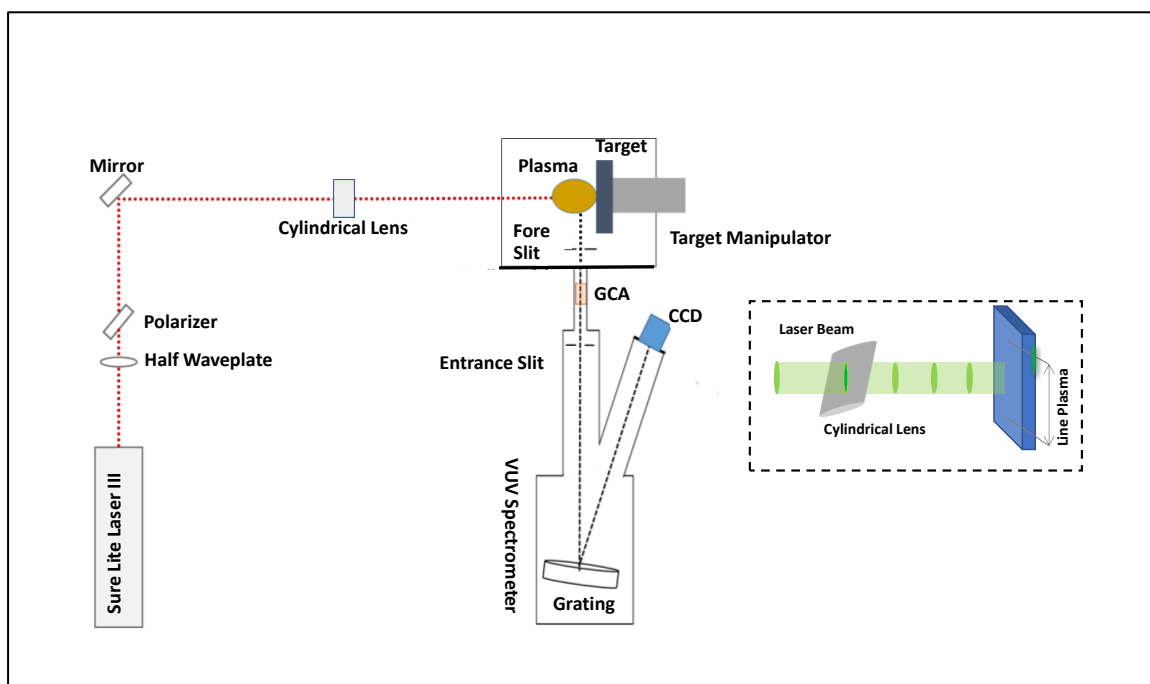


Figure 5. 1 TISR LIBS setup with plano-convex cylindrical lens (focusing in the vertical direction).

Since the overarching objective of this research is the optimization of the LoD for carbon in steel using the C^{+2} line at 97.7 nm, the key task has to be to maximize the corresponding SBR. Hence it is the combination of high emission intensity (signal) along with low background, and background fluctuation, amounting to a low standard deviation ' σ ' for the background, that must be aimed for. To this end, a steel sample with a carbon concentration of 520 ppm was used in experiments, designed to determine the lens and target positions that optimised signal to noise ratio (SNR), signal to background ratio (SBR) and limit of detection (LoD). Measurements were made for target positions (displacements from the optic axis of VM521 VUV spectrometer) ranging from 0.5 mm to 2.5 mm, in steps of 0.5 mm. These measurements were also made at each target position for different lens positions, ranging from

12.5 mm to 25 mm, in step of 1 mm. 25 laser shots were taken at every target and lens position and then averaged.

Figures 5.2 - 5.4 shows some sample spectra obtained at lens positions of 5 mm, 10 mm and 20 mm for target positions ranging from 8.0 mm to 9.5 mm for the chosen reference steel sample CRM 12 B 1767 (purchased from Glen Spectra Reference Materials TM). This sample has an average concentration of 520 ppm which sits in the middle of the range for other samples used for LoD studies, as can be seen in table 5.1.

Table 5. 1 Steel samples and the respective carbon concentrations

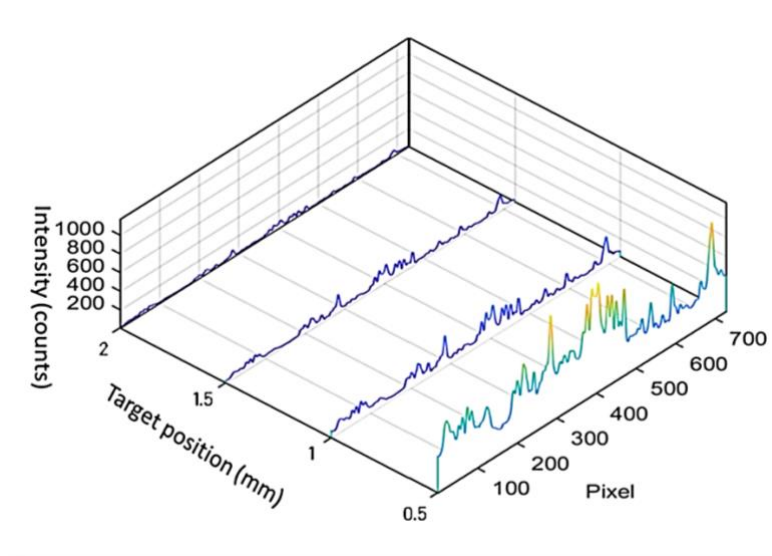
No	Sample Label	Concentration (ppm)
1	CRM Fe 1/1	50
2	11 CM 5078	180
3	1008 BS XAAS	410
4	CRM 12 B 1767	520
5	CRM 14 MI 206A	680
6	CRM 12 X 15252P	940

For all these experiments a combination of half wave plate and polarizer was used to attenuate the laser pulse energy. In the case the polariser is set orthogonal to the polarisation direction of the laser to act as an analyser. The half wave plate is inserted between the laser output aperture and the polariser and rotated to control the polarisation plane angle and hence the power transmitted by the analyser polariser [1]. The laser pulse energy around 450 mJ is used to perform all these experiments.

All spectra used for the calibration curves and limit of detection calculations represent the average of 150 laser shots. Spectra were captured and stored as single laser shots and aggregated after each experiment for post processing and analysis. During the experiments

there were 25 laser shots at each target position, achieved by simply moving the target in the x-y plane and/or rotating it after each 25-shot accumulation. This was done in order to avoid the crater effects. The laser was focused above and below the target surface, as previous studies showed that maximum intensity of the selected C(III) line was acquired when the laser beam was focused between 5 to 10 mm above and below the target surface in case of single pulse VUV LIBS experiments in point plasma studies [1].

In addition, when the focal point is above the sample surface, the plasma temperature is expected to be higher because the plasma plume expands into the more tightly focused laser beam region where the laser beam power density is correspondingly higher than in the case where is focused below the target surface. For the line plasma studies, the effects of defocusing of the lens with respect to the target were studied, as they were in previous studies for point plasmas [15,16,17], so that the optimum target position and lens position could be determined.



(a)

Figure 5. 2 TI-SR VUV LIBS spectra for different locations of the target surface relative to the optic axis of the spectrometer. The C(III) line at 97.7 nm occupies the pixel range from 467 to 475 while the pixel range 637 to 645 was chosen to estimate the background intensity. The cylindrical lens was defocused by 12.5 mm (below the target).

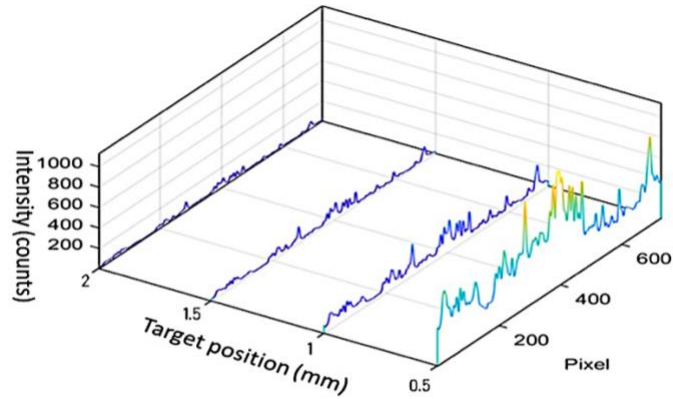


Figure 5. 3 TI-SR VUV LIBS spectra for different locations of the target surface relative to the optic axis of the spectrometer. The C(III) line at 97.7 nm occupies the pixel range from 467 to 475 while the pixel range 637 to 645 was chosen to estimate the background intensity. The cylindrical lens was defocused by mm (below the target).

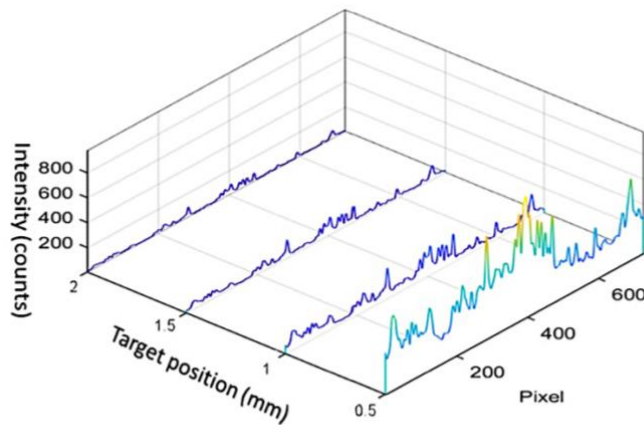


Figure 5. 4 TI-SR VUV LIBS spectra for different locations of the target surface relative to the optic axis of the spectrometer. The C(III) line at 97.7 nm occupies the pixel range from 467 to 475 while the pixel range 637 to 645 was chosen to estimate the background intensity. The cylindrical lens was focused by 2.5 mm (above the target).

Figures 5.2 to 5.4 show three examples of TI-SR VUV spectra for plasmas formed by a line focused laser. Each figure corresponds to a different degree of defocusing of the cylindrical lens, namely 5mm, 10 mm and 20 mm above the steel target surface. In each figure four spectra are shown corresponding to displacements of the target surface by 8.0 mm, 8.5

mm, 9.0 mm and 9.5 mm, respectively, from the optic axis of the VM521 VUV spectrometer. It is clear that the overall spectral intensity varies significantly with target location for every lens defocus and especially so when one compares the 0.5 mm location to the other three. The effect of lens defocus is also clear, but more gradual, with the overall spectral intensity decreasing with increasing defocus from 12.5mm to 7.5 mm below and above the target surface.

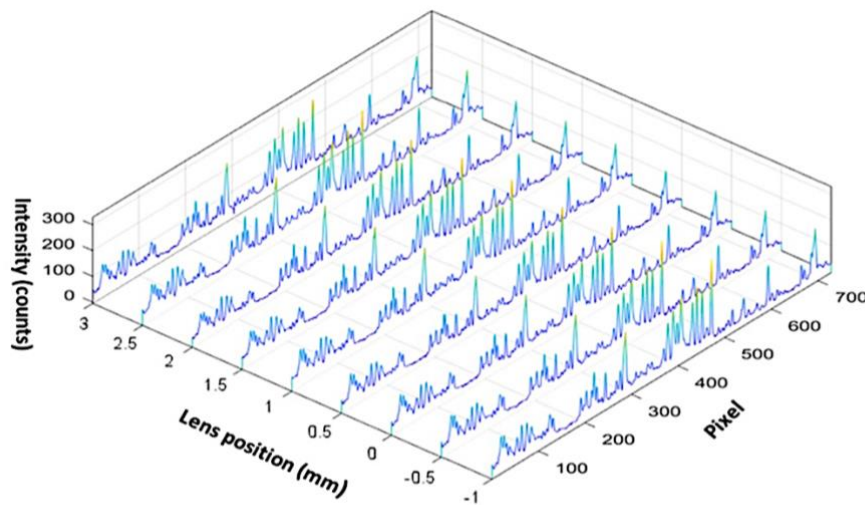


Figure 5. 5 TI-SR VUV LIBS spectra for a displacement of the target surface, relative to the optic axis of the spectrometer, of 1 mm. The C(III) line at 97.7 nm occupies the pixel range from 467 to 475 while the pixel range 637 to 645 was chosen to estimate the background intensity. The cylindrical lens focus was varied from -1 mm to 3 mm in increments of 0.5 mm (above the target).

Figure 5.5 shows the spectra obtained at a target position of 1 mm with the lens defocused from -1 mm to 3 mm with an emphasis on analysing its effect on the line intensities and background intensities. The plot was motivated by the fact that the 2 mm target offset appeared to yield the best compromise between a low background intensity while exhibiting clear and distinct line emission. Hence it was considered a good plan to look at the defocusing effects on the spectral distribution of the VUV emission in more detail than in figure 5.2-5.4.

For limit of detection, the standard deviation of the background intensity is considered as a parameter of the utmost importance as the lowest fluctuation in the background intensity is one key to obtaining the best limit of detection in LIBS experiments. For example, in figure 5.2 above, for each of these spectra shown, it can be seen that the spectrum recorded at a target position of 0.5 exhibits the highest overall line intensities.

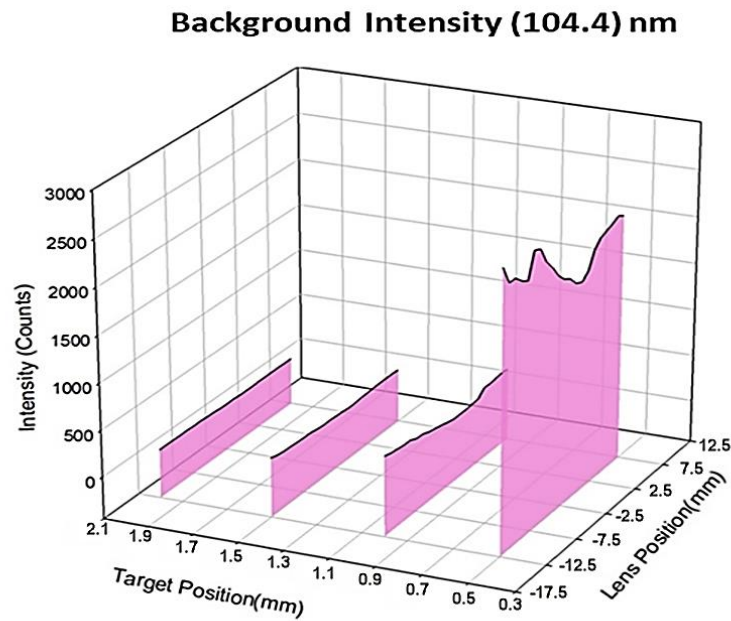


Figure 5. 6 Intensity of the background (at ca. 104.4 nm) obtained at four different target positions ranging from 8.0 to 9.5 mm and lens positions ranging from 5 mm to 25 mm.

However, this spectrum also exhibits the highest background levels, and one can expect the highest fluctuation in the background since, in simple terms, for a background signal level of ' N ' counts, the noise or fluctuation on that level will be related to \sqrt{N} . The spectra obtained at a target position of 1 mm in each of figures 5.2 to 5.4, appears to be the best compromise on the basis of the two key criteria, i.e., high CIII 97.7 nm line intensity along with lowest background level (with respect to the line intensity) and hence low fluctuation in the background. In order to select the optimum spectrum from those recorded, the spectral data

needed to be analysed in greater detail with respect to 97.7nm line intensity and 104.4 nm background level.

To this end, the background intensity was measured for different target and lens positions, as can be shown in figure 5.6. The average background intensity was extracted by computing the integral of 11 pixels around 104.4 nm. It can be seen that there is a large drop in the background intensity when the target is moved from 0.5 mm to 1 mm relative to the optic axis of the spectrometer. On the other hand, there is not much difference when the target is moved further to displacements of 1.5 mm and 2 mm. The significant dropoff in the background between the 0.5 mm and 1.0 mm target positions reflects the fact that most of the continuum emission comes from the hot core of the laser plasma which is quite small in extent (typically less than 1 mm in diameter). Hence, when the target surface is pulled back by 1 mm, the main continuum emitting region is occluded from the spectrometer. Hence the ‘cliff edge’ in figure 5.6 that is observed between 0.5 mm and 1.0 mm.

It is also worth noting that the background intensity changes quite significantly with lens position for a target position of 0.5 mm (figure 5.6). Therefore, 0.5 mm target location should be compared with the background continuum emission at target surface positions of 1.0 mm, 1.5 mm, and 2.0 mm which is lower and more stable.

The intensity of the CIII line of interest was obtained by taking the integral of 11 pixels around a wavelength of 97.7 nm (figure 5.7). Each individual spectrum represents the average of 150 laser shots with 25 single shot spectra taken at each target position. The line intensity is highest when the target is located a distance of 0.5 mm from the optic axis. At 1.0 mm the average peak intensity drops sharply and continues to decrease more slowly as the target is moved to locations at 1.5 mm and 2.0 mm.

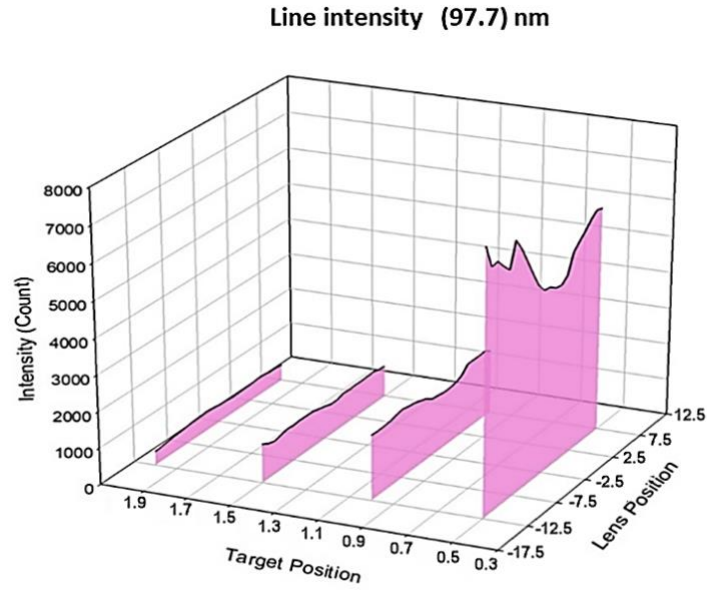


Figure 5. 7 Intensity of the 97.7 nm line obtained at four different target positions ranging from 0.5 mm to 2.0 mm and lens positions from 12.5 mm to 17.5 mm above and below the target surface.

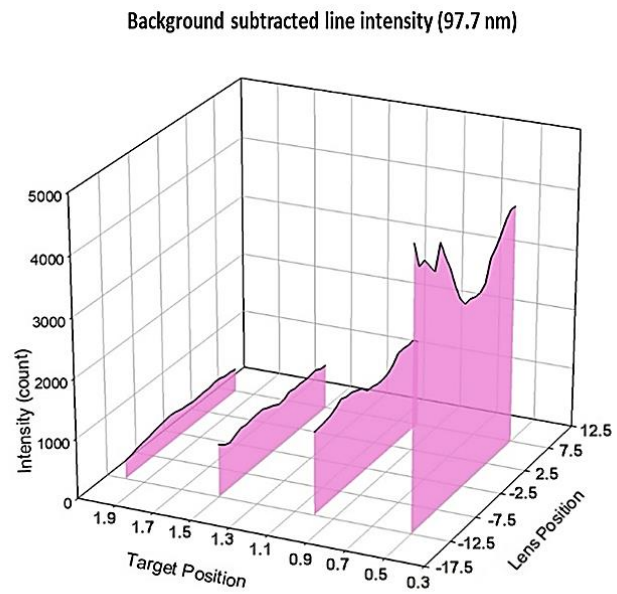


Figure 5. 8 Background subtracted, peak intensity of the 97.7 nm line at four different target positions ranging from 0.5 mm to 2.0 mm and lens positions from 12.5 mm to 17.5 mm above and below the target surface.

Hence the target position is very significant in the optimization of the signal in TI-SR VUV LIBS. In summary a target location of 1 mm results in a significantly lower variation in the background intensity with lens position while maintaining a strong 97.7 nm signal. In addition, it was found that the 97.7 nm signal was also reasonably insensitive to the lens defocus with the target located at 1 mm.

For the calibration curve and limit of detection determination, it is the *background subtracted intensity* of the C^{+2} line at 97.7 nm that is used. Therefore, the background subtracted line intensity was analysed at different target and lens positions (figure 5.8). The overall trend in 97.7 nm line intensity (raw and background subtracted) with target location is similar in both figures (5.7 and 5.8). For each target location, the lens position range over which the 97.7 nm line intensity appears to be quite stable lies between -1.5 and 2.5 mm. As proposed earlier, the target location that gives the best compromise between a high 97.7 nm signal combined with a small background signal level is 1.0 mm with respect to the optic axis of the spectrometer.

One other highly significant parameter is the standard deviation of the background, which is the parameter used to quantify the fluctuation in the background or continuum emission. Figure 5.9 shows that the standard deviation of the background (SDB) is largest and varies quite a lot with lens position (focusing/defocusing) when the target is placed at the 0.5 mm position. It is lower and flatter for all other target positions. It also varies with lens position with the lowest fluctuation of background emission when the lens was placed between -1.5 mm to 2.5 mm position from the target surface, albeit the improvement is marginal. This result serves to copper fasten the choice of target surface location to lie at 1.0 mm with a lens defocus somewhere between -1.5 mm and 2.5 mm.

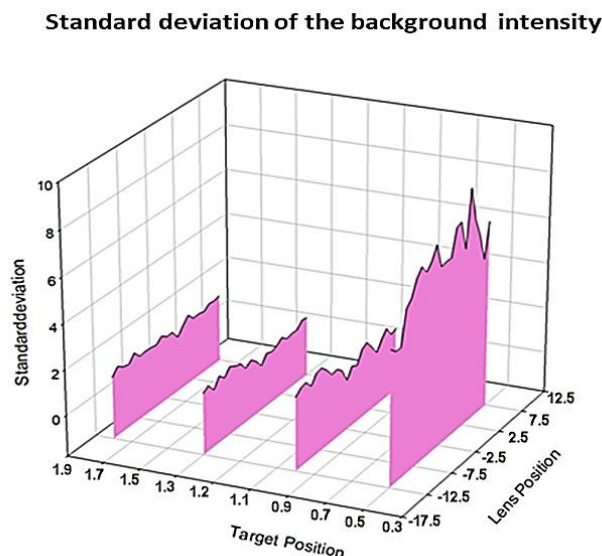


Figure 5. 9 Standard deviation of the background intensity (at ca. 104.4 nm) obtained at four different target positions ranging from 0.5 to 2.0 mm and lens positions from 12.5 mm to 17.5 mm above and below the target surface.

Figure 5.10 below shows the integral of 150 spectra obtained at 1 mm target position and 2.5 mm lens position. Figure 5.11 (a) shows how the CIII 97.7 nm line and background at 104.4 nm intensities vary with target position for one single lens position, namely 1.0 mm. It can be very clearly seen here that the line and background (continuum) intensity values both drop significantly when the target is moved away from the optic axis of the spectrometer, from 0.5 mm to the 1.0 mm position. The rate of the decay in each signal drops significantly in the 0.5 mm to 2.0 mm range and it can be seen that the optimal SBR is obtained at a target position of 1.0 mm.

The data in figure 5.11 (b) shows the average line intensity obtained at every target position from 1.5 mm to 2.0 mm. Using the values of average background subtracted line intensities and average background intensities, one can extract the signal to background ratio (SBR) which is an important indicator of the quality of spectral signal used for LIBS which is shown in figure 5.10 (b).

The standard deviation of the background shown in figure 5.11 is obtained by simply calculating the standard deviation of the background of 150 spectra obtained at each target position. For the optimum limit of detection, we need to find the target position where we can obtain the most stable signal i.e., with very low standard deviation. Also, in the case of figure 5.11, the standard deviation of the background (SDB) was obtained at every lens position from 12.5 mm below to 7.5 mm above the target surface.

The spectra obtained represent the accumulation of a number of individual laser shots (determined by the laser repetition rate and CCD exposure time, typically 10 pulse per second and 1 second). The thermal background (or dark signal) was subtracted from each accumulation (CCD integration) leaving the residual thermal noise fluctuations on the resulting spectrum. This residual noise was thus superimposed on the noise due to random photon number fluctuations on each signal. Hence, the noise on each pixel results from different noise sources. To obtain the final spectra for the construction of each calibration curve and the determination of the background standard deviation a number of accumulated spectra were added together to form the average of typically 150 single shot spectra.

For the calculation of the SDB, 11 pixels, representing 11 measurements of the background signal (pixels 637 to 645 around 104.4 nm), were used. A MATLAB code was used to process all measurements including accumulating and averaging spectra and determining standard deviations. In this case each pixel was considered as a single background measurement for the statistical analysis and the sum of 11 pixels was considered as the total background. The resulting sum of 11 pixel values for a target position of 1 mm is equal to c.a. 300 as seen in figure 5.11 a. Figure 5.11 b shows the corresponding standard deviation which was calculated to be ca. 10 counts.

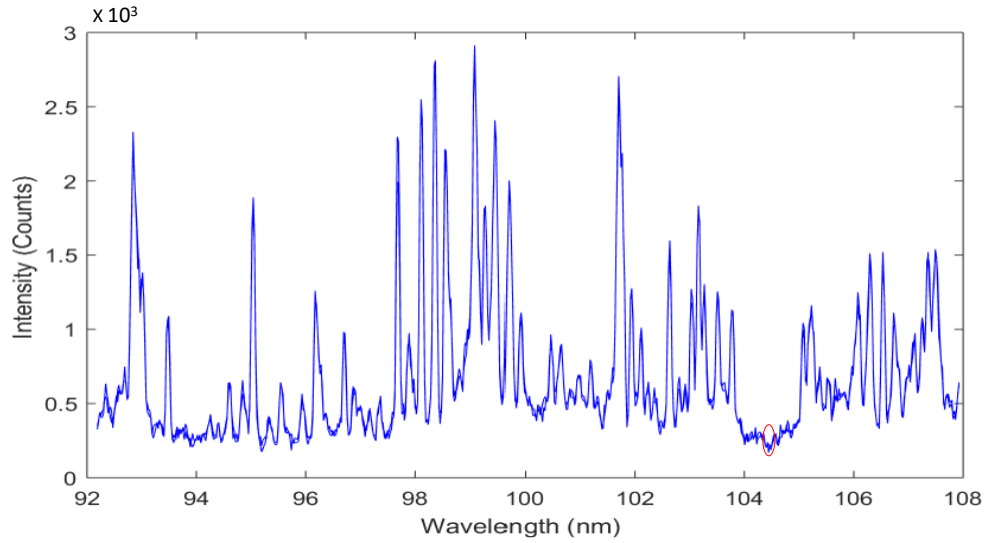


Figure 5. 10 Overlapped 150-line plasma spectra, when the target was placed at 1 mm and lens position at 2.5 mm.

The trend in figure 5.10 (b) shows that the signal to background ratio increases with distance of the target from the optic axis of the spectrometer. It is interesting to note that while the standard deviation of the background (SDB) is quite flat for target positions from 1.0 mm to 2.0 mm, the SBR increases from below 6 to almost 8. This observation indicates that while both the signal and the background levels may be decreasing relative to the 97.7 nm line signal (in this target position range), the background does so faster.

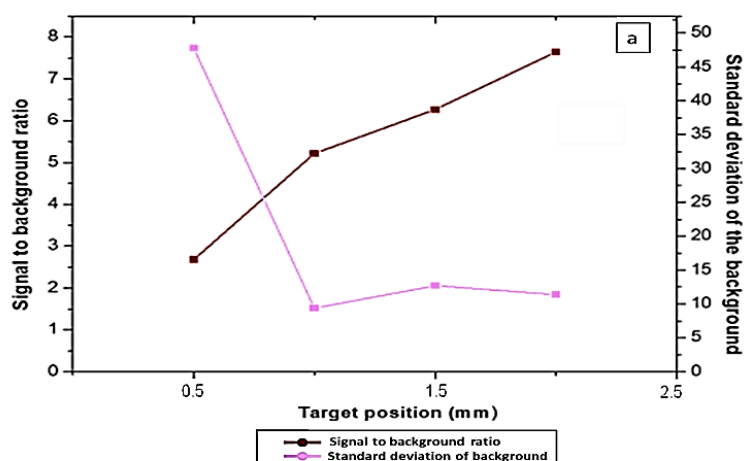
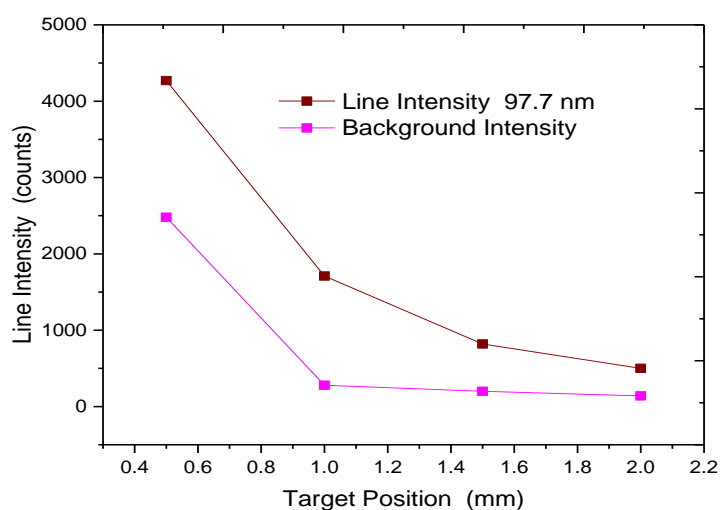


Figure 5. 11 Line (97.7 nm) and background intensities obtained at four different target positions ranging from 0.5 mm to 2.0 mm. The lens position was fixed at 1 mm. Using the raw data shown in panel (a), the signal to background ratio (SBR) and standard deviation of the background (SBR) at ca. 104.4 nm are obtained and shown in panel (b). Two plots in (a) and (b) have two different scales.

Figure 5.12 (a) illustrates the variation in both CIII 97.7 nm line and continuum (around 104.4 nm) signals with lens position. The target position was 1.0 mm. These data were used to construct the traces in figure 5.12 (b). The background signal varies from 220 – 420 counts with a mean value of ca. 310 counts. The 97.7 nm discrete line signal varies from just below 1,600 counts to just above 1,280 counts with a mean value of approximately 1430 counts.

Whereas the signal to background ratio (SBR) varies from a minimum value close to 3.0 to a maximum value of ca. 5.5, as shown in figure 5.12 (b).

In figure 5.12 (b) the SBR and the standard deviation of the background (SDB) are shown. These data were obtained from spectra recorded at a target position of 1 mm. It can be seen that the SBR increases as the lens is moved from 12.5 mm to 2.5 mm and thereafter it remains reasonably constant over the focus range from 2.5 mm to 2.5mm below and above the target surface after which it again starts to decrease. On the other hand, the SDB fluctuates over the whole lens focus/ defocus range from a low of approximately 4 to a high of almost 20 but is confined to a reasonable narrow range of values, from ca. 8 to 12, for lens positions lying in the range from 1.5 mm below to 2.5 mm above the target surface. Hence, once again, a lens defocus position between 1.5 mm and 2.5 mm is a good choice for TR-SI VUV LIBS experiments with 'line plasma' plumes as both parameters (SBR and SDB) are quite stable in that range. This is clear from the 'dip region' in figure 5.12 (a). It should also be noted that although both line and continuum signals exhibit the lowest absolute intensities in this lens defocus range (figure 5.12 (a)) the SBR is highest, lying between 5.0 and 5.5 in this case.

The optimum target position was also confirmed to be 1.0 mm with the lower background signal and lower standard deviation of the background signal and relatively higher signal to noise ratio for the CIII 97.7 nm line intensity in comparison to other target positions. Also, according to data obtained the optimum lens position obtained was found to lie in the range 1.5 mm below to 2.5 mm. This lens position range yield good SNR for the 97.7 nm line, stable SBR values of ca. 5.5, along with low fluctuation in the background (figure 5.12 (b)). For this reason, the target surface was located at a distance of 1.0 mm from the optic axis of the spectrometer and the lens position (focus/defocus) was chosen to be 2.5 mm in front of the target.

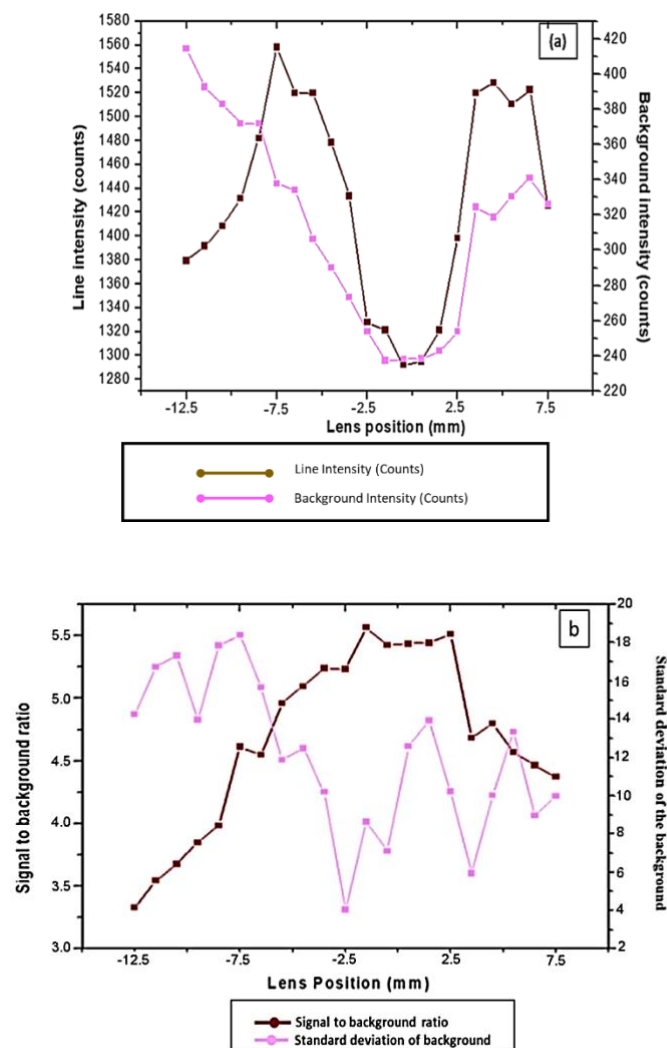


Figure 5. 12 Line (97.7 nm) and background (ca. 104.4 nm) intensities obtained at lens positions ranging from 12.5 mm to 7.5 mm below and above the target surface, when target was fixed at 1.0 mm. (a) Using the raw data show in panel, (b) the signal to background ratio (SBR) and standard deviation of the background (SDB) are obtained and shown in panel.

Two plots in (a) and (b) have two different scales.

Hence the optimum conditions determined above and subsequently used to perform the final experiments, shown in the next section 5.3, are summarised in table 5.2 below. Using these conditions line plasma experiments were performed on a number of standard reference steel samples and compared with time integrated, space resolved (TI-SR) and time resolved VUV LIBS results.

Table 5. 2 Parameter for experiments on calibration curves and limit-of-detection for C in steel

Optimized lens position	2.5 mm
Optimised Target position	1.0 mm
Laser Energy	450 mJ
Focus type	Line focus
Pulse width	6 ns
Lens Type	Cylindrical lens
CCD Exposure time	1 sec (Laser in single shot mode)
CCD Temperature	-40° C
Laser Beam diameter	9.5 mm

5.3 TI-SR VUV LIBS Spectra for Optimum SBR

Using optimized experimental parameters, final TI-SR VUV LIBS experiments were performed for line plasmas formed on six different steel targets of low carbon concentration (listed in Table 5.1). The data extracted from these spectra were used to construct the calibration curve for the determination of the carbon content in unknown steel samples. Figures 5.12 - 5.17 show the spectra of the six different steel reference samples with carbon concentrations of 50, 180, 410, 520, 680 and 940 parts per million (ppm). These TI-SR VUV LIBS spectra were obtained by aggregating 150 single shot spectra. Using the information shown in Section 5.2, the target surface was pulled back from the optic axis of the Acton Research Corporation VM521 VUV spectrometer by a distance of 8.5mm. The lens was set in order to focus the Continuum Surelite III-10 laser 20 mm in front of the target. The laser pulse energy was set to 450 mJ. The spectra show the clear evolution of the CIII 97.7 nm line with target concentration relative to the Fe matrix spectrum.

As in Section 5.2 above, in order to determine CIII line and background intensities, the counts from 11 pixels centered at wavelengths of 97.7 nm (line) and 104.4 nm (continuum), respectively, were summed. In order to get the continuum free 97.7 nm line signal, the background level was subtracted from each line intensity. These corrected intensity values were used to determine the signal to construct the calibration curve for carbon in steel.

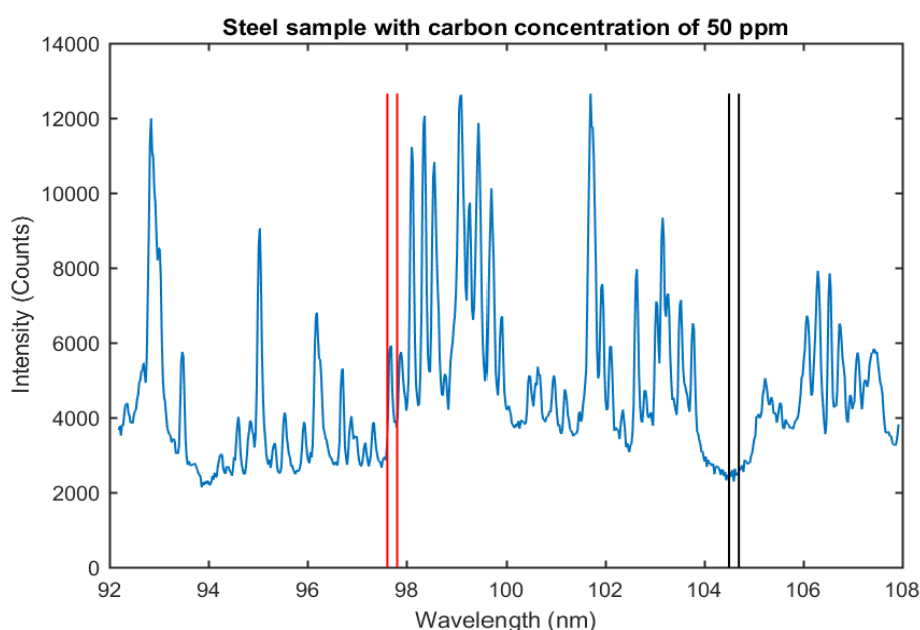


Figure 5. 13 Spectrum obtained with the reference target CRM Fe 1/1 (carbon concentration of 50 ppm). Red bars – the 11 pixels integrated around the C III $1s^2s2p (^1P_1)$ to $1s^2s^2 (^1S_0)$ line at 97.7 nm. Black bars – the background was obtained by integrating 11 pixel values around 104.4 nm.

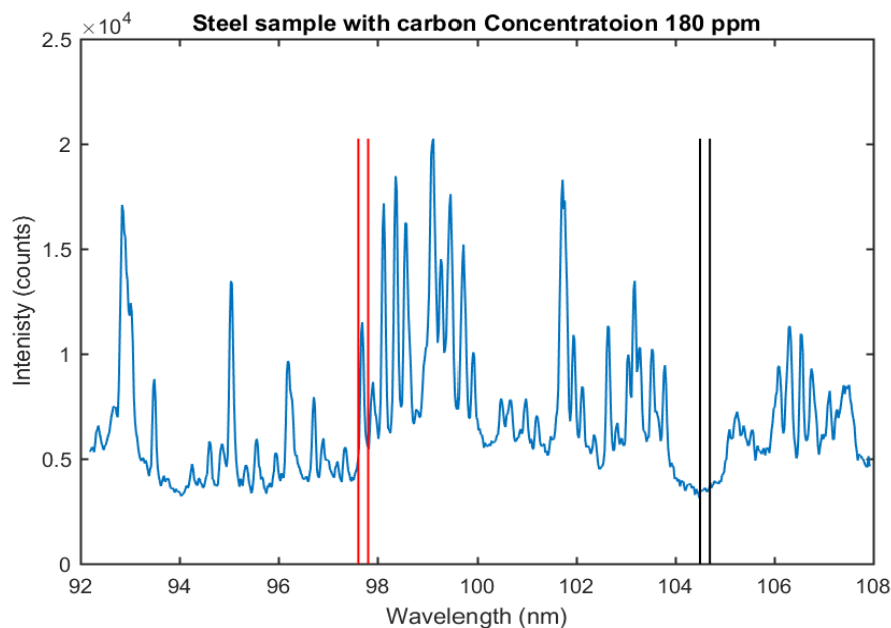


Figure 5. 14 Spectrum obtained with the reference target 11 CM 5078 (carbon concentration of 180 ppm). Red bars – the 11 pixels integrated around the C III $1s^22s2p (^1P_1)$ to $1s^22s^2 (^1S_0)$ line at 97.7 nm. Black bars – the background was obtained by integrating 11 pixel values around 104.4 nm.

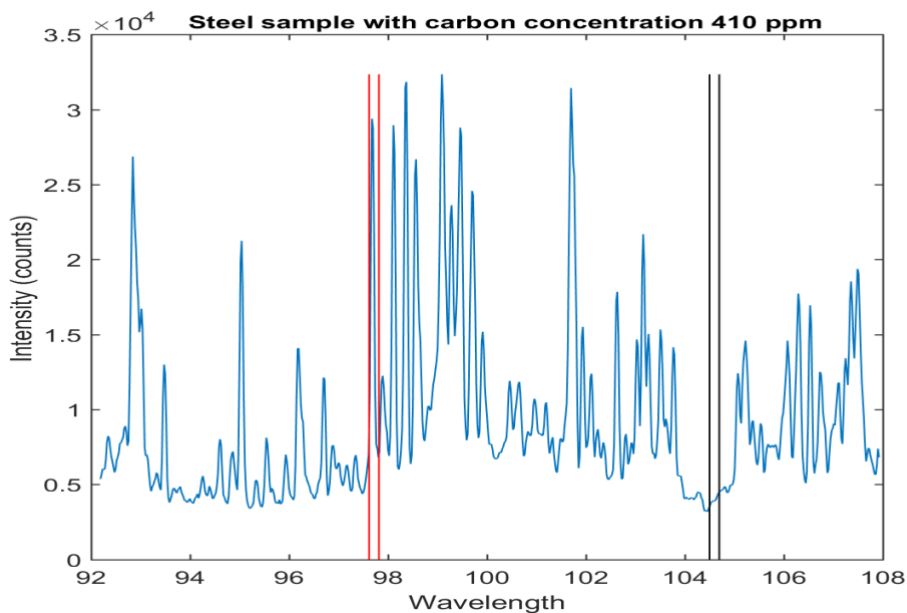


Figure 5. 15 Spectrum obtained with the reference target 1008 BS XAAS (carbon concentration of 410 ppm). Red bars – the 11 pixels integrated around the C III $1s^22s2p (^1P_1)$ to $1s^22s^2 (^1S_0)$ line at 97.7 nm. Black bars – the background was obtained by integrating 11 pixel values around 104.4 nm.

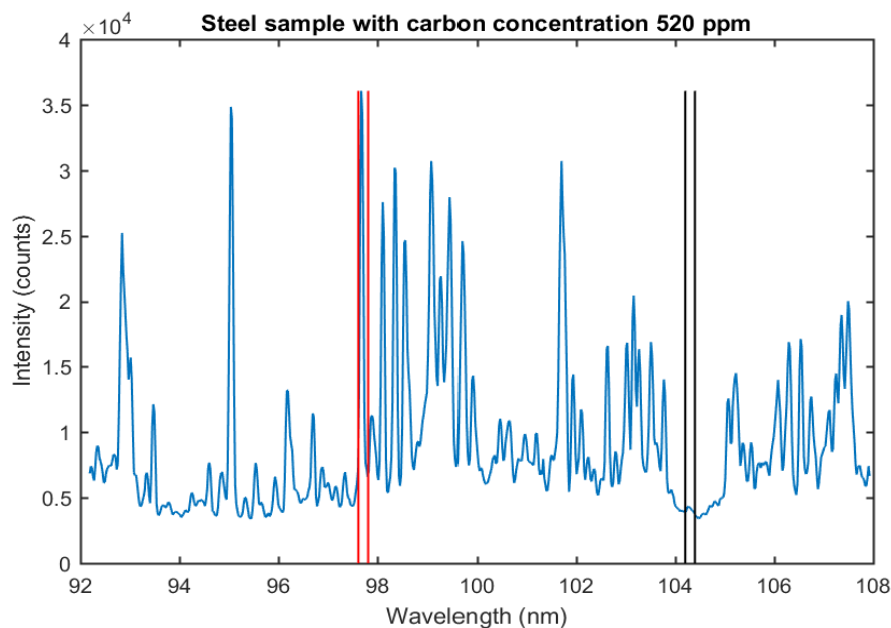


Figure 5. 16 Spectrum obtained with the reference target CRM 12 B 1767 (carbon concentration of 520 ppm). Red bars – the 11 pixels integrated around the C III $1s^22s2p$ (1P_1) to $1s^22s^2$ (1S_0) line at 97.7 nm. Black bars – the background was obtained by integrating 11 pixel values around 104.4 nm.

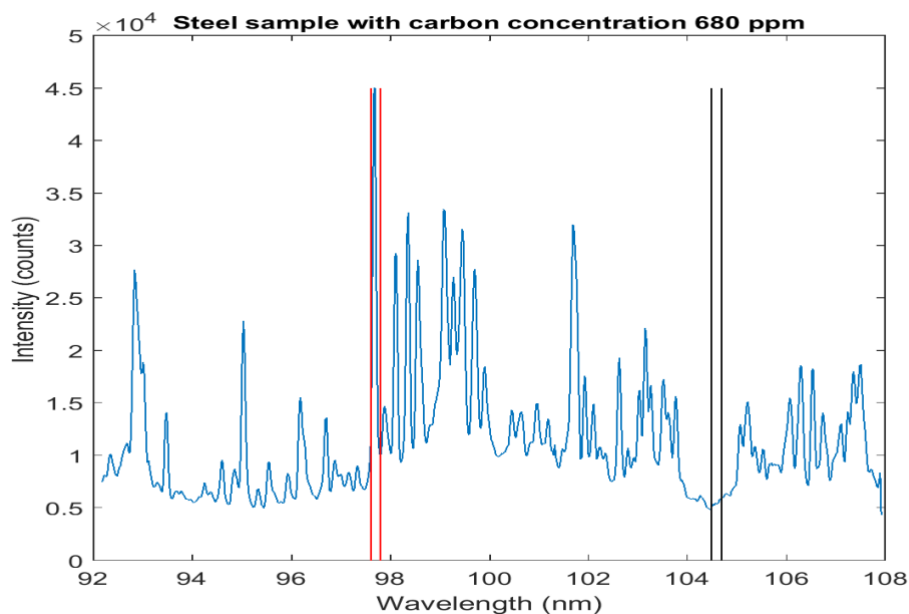


Figure 5. 17 Spectrum obtained with the target CRM 14 MI 206A (carbon concentration of 680 ppm). Red bars – the 11 pixels integrated around the C III $1s^22s2p$ (1P_1) to $1s^22s^2$ (1S_0) line at 97.7 nm. Black bars – the background was obtained by integrating 11 pixel values around 104.4 nm.

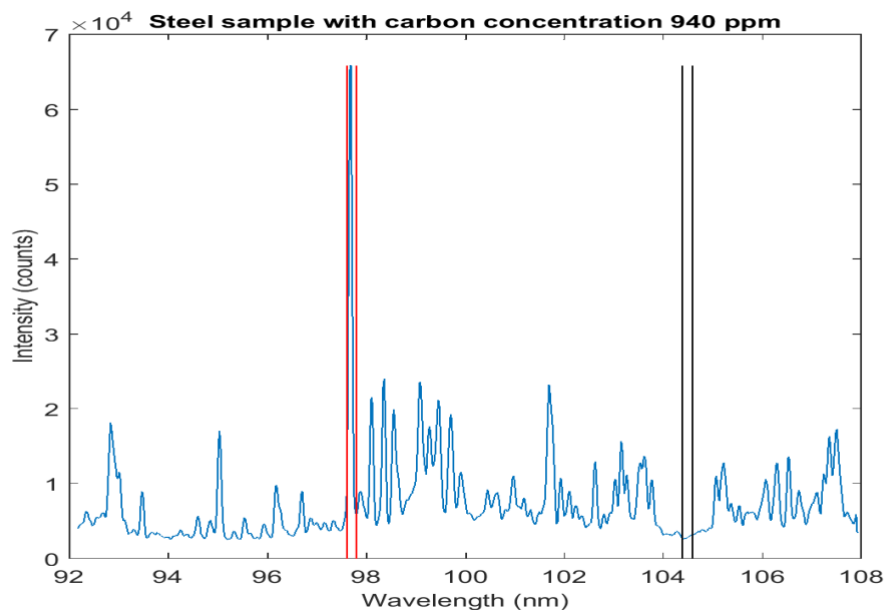


Figure 5. 18 Spectrum obtained with the target CRM 12 X 15252P with a carbon concentration of 940 ppm. Red bars – the 11 pixels integrated around the C III $1s^22s2p$ (1P_1) to $1s^22s^2$ (1S_0) line at 97.7 nm. Black bars – the background was obtained by integrating 11-pixel values around 104.4 nm.

The line, continuum and SBR values extracted from each spectrum shown in figures 5.12 to figure 5.17 (inclusive) are shown in table 5.3. It is clear from the table that there is a general trend for the SBR to increase with concentration, as expected.

Table 5. 3 CIII 97.7 nm line intensity (background subtracted), and signal to background ratio (SBR) obtained from different samples of steel having different carbon concentrations

Sample	Concentration (ppm)	Laser pulse energy (mJ)	Line Intensity C (III)
CRM FE 1/1	50	450	421
11 CM 5078	180	450	1180
1008 BS XAAS	410	450	2340
CRM 12 B 1767	520	450	2960
CRM 14 MI 206A	680	450	3890
CRM 12 X 15252P	940	450	5420

The data contained in the Table 5.3 was used to construct a calibration curve for carbon in steel and ultimately determine a limit-of-detection for TI-SR VUV LIBS using a line plasma focus which could then be compared with the results on point focus plasmas from chapter 4.

5.4 Calibration Curve

For this exercise 150 single shot VUV spectra of each steel sample were aggregated, from which the CIII line at 97.7 nm was extracted and the background continuum level determined. Background elimination on the emission line of interest was done by subtracting the integral of 11 pixels of the background signal (in the vicinity of the 97.7 nm line) from the integral of 11 pixels of the raw carbon emission line intensity values at 97.7 nm. The background subtracted CIII emission line intensity was then used to form the final calibration curve shown in figure 5.18.

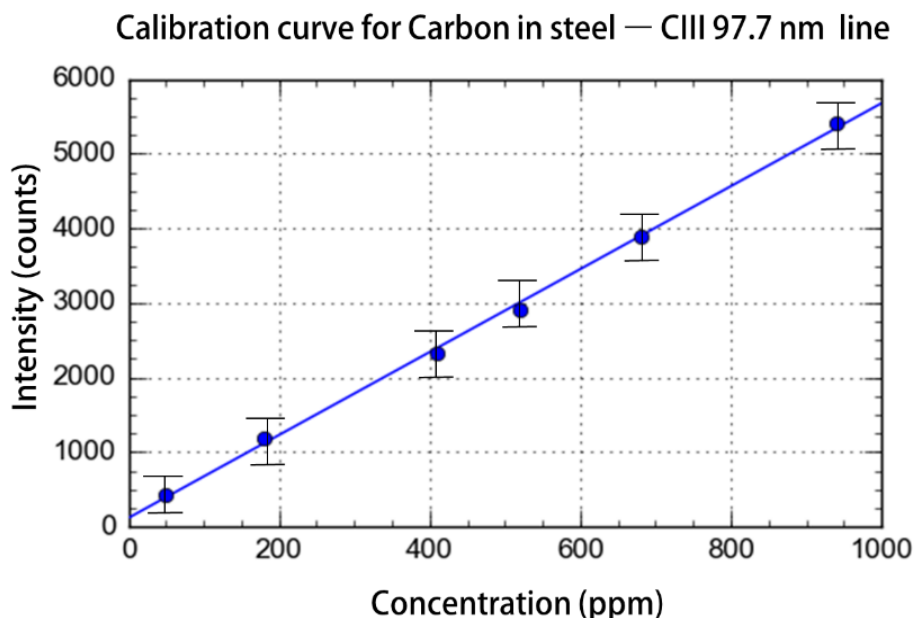


Figure 5. 19 Carbon in steel intensity calibration curve. Six different samples with carbon concentrations of 50 ppm to 940 ppm (cf. Table 5.1) were used to construct the curve.

The calibration curve is quite linear with a coefficient of determination (R^2) of 0.99823 which can be considered to be a very good value. A calibration curve with the R^2 value of about 0.97 is considered as reliable but if in cases where it is higher than 0.99, it means that the regression model is sufficiently reliable to predict the outcomes of the unknown values. In this case it means that the value of carbon concentration can be obtained on the basis of the measured intensity of the (background subtracted) CIII 97.7 nm line intensity obtained from the spectrum of any sample of unknown concentration, within this range. In the next, and final section, the limit of detection and limit of quantification for carbon in steel are computed. These require some additional information to be determined, namely the slope of the calibration curve ‘S’ and the variance in the background signal ‘ σ ’.

5.5 Limit of Detection (LoD) and Limit of Quantification (LoQ)

On the basis of calibration curve obtained in the previous section the limit of detection can be calculated. The formula used to obtain limit of detection (LoD) is shown in Section 2.6 (Eqn. 2.34). By definition it is the lowest quantity of a substance (analyte) which can be distinguished from the absence of that substance with some defined confidence level, typically 99.7%, or 3σ [18]. The latter is the signal corresponding to the absence of the analyte, in this case carbon, is sometimes referred to as the limit of blank (LOB). The limit of detection may be obtained from the calibration curve (figure 5.18) by dividing the slope (5.6) of the calibration plot by three times the standard deviation of the background signal (93 counts) (the latter arising from the specification of a 99.7% confidence interval for a normal distribution).

$$LoD = \frac{3*(\sigma=93)}{s=5.6} = \sim 50 \text{ ppm}$$

For the case of TI-SR VUV LIBS of carbon in steel, using line plasma formation, the limit of detection is found to be ~ 50 ppm (or $50 \mu\text{g/g}$) as calculated above. The corresponding limit of quantification (LoQ) is usually taken as $3.3 \times LoD$ [18] and hence it is 167 ppm (or

167 µg/g) in this case. These values are to be compared with those obtained from VUV LIBS measurements made with point plasmas in chapter 4. The LoDs obtained in those cases were ca. 220 ppm from TI-SR LIBS for a target displacement of 2 mm from the optic axis and ca. 315 ppm for the same measurements made at 4 mm target displacement from the OA. The LoD obtained from the single channel time resolved (TR) VUV LIBS data was closer to the value obtained here at ca. 55 ppm but still some 10% higher. In order to compare the three LoD values an ‘improvement parameter’ β is introduced.

$$\beta = \frac{LOD_{pointplasma}}{LOD_{line plasma}} \quad \text{eq. (5.1)}$$

Table 5. 4 LoD improvement for line plasma-based VUV LIBS over point plasma-based VUV LIBS

	Point plasma - time integrated space resolved at 2 mm	Point plasma - time integrated space resolved at 4 mm	Point plasma - time resolved
β	4.5	6.3	1.1

Hence results in table 5.4 show that limit of detection for the line plasma experiments is better than other time integrated and even time resolved methods, albeit the LoDs are quite close. The results obtained through line plasma experiments can be even better than all other single pulse experiments performed on this system. In 2002, when the system was new, M A Khater achieved 1.2 ppm using the same system [10,12]. Jiang et al. measured a LoD of about ~54 ppm in 2013 using single pulse experiments in vacuum whereas repeating the exact same experiments here gave results of 316 ppm of LoD [19]. Therefore, we can conclude that line plasma will yield a significantly better absolute LoD for a VUV LIBS system with all new optical components (grating, GCA, etc.). So, TI-SR VUV LIBS with a line plasma source can be considered to be the optimum method to improve limit of detection for trace amounts of carbon in steel samples.

If we compare our optimized values with the other existing values in the literature, it is evident that most of the groups have determined (LoD) at the wavelength of 193.09, for the C(I) line. The current study shows that the results show the lowest LoD of all times in single pulse mode in vacuum using both the Line plasma method and time resolved LIBS for the C(III) line at 97.7 nm.

Table 5. 5 Comparison of limit of detection with the literature

1992	1993	1999	2000	2001	2002	2012	2019	2020
C(I)	C(I)	C(I)	C(I)	C(I)	C(III)	C(III)	C(I)	C(III)
193.09	193.09	193.09	193.09	193.09	97.7	97.7	193.09	97.7 nm
Aguilera et.al	Aragon et al	Aragon et al	Strum et al	Noll et al	Khater et al	Jiang et al	V strum et al	S. Zehra et.al
65 ppm	250ppm	80 ppm	7 ppm	3 ppm	1.2ppm	3.6 ppm	34 ppm	50ppm

Summary

The results of line plasma experiments are discussed in this chapter. the effect of defocusing of the lens and target position was investigated for target positions from 8 to 9.5 mm back from the optic axis of the VM521 spectrometer and at lens positions defocus positions of 5 mm to 25 mm above the target surface. The optimal lens position was found to lie between ca. 16 and 20 mm. The 20 mm lens defocus position was chosen for the different statistical analyses leading to LoD measurements. The optimum target surface position was chosen to be 8.5 mm from the VM521 optic axis.

The spectra obtained for 6 different samples were analysed and discussed in the later part of the chapter. The C(III) line was analysed for each spectrum and a calibration curve for intensity versus concentration established from which the limit of detection could also be determined. It was concluded that a line plasma, obtained by employing cylindrical lens focusing, is the optimum method to obtain the lowest limit of detection in carbon in steel in comparison with all other techniques used for the determination of the limit of detection under similar conditions.

References

- [1] Hahn D.W, Omenetto N. 2012. Appl. Spectrosc. **66** pp 347-419.
- [2] Hahn D.W, Omenetto N. 2010. Appl. Spectrosc. **64** pp 335A-66A.
- [3] Musazzi S, Perini U. 2014. Laser-Induced Breakdown Spectroscopy Springer Berlin, Heidelberg **182** pp 59-89 (ISBN978-3-642-45085-3).
- [4] Glen technology reference materials, user guide; 2020.
- [5] Andor CCD camera, User guide, Andor technology, 2000.
- [6] Ej-212 Eljen technology fast scintillator, <https://eljentechnology.com>. 2016.
- [7] Hamamatsu photomultiplier tubes (R1450), <https://www.hamamatsu.com>. 2016.
- [8] Tognoni E, Cristoforetti G. 2016 Opt Laser Technol. **79** 164-172.
- [9] Jiang X, Hayden P, Laasch R, Costello J.T, Kennedy E.T. 2013 Spectrochim. Acta - Part B At. Spectrosc. **86** pp 66-74.
- [10] Khater M.A, Van Kampen P, Costello J.T, Mosnier J.P, Kennedy E.T. 2000 J. Phys. D Appl. Phys. **33** pp 2252-2262.
- [11] Mateo M.P, Palanco S, Vadillo J.M, Laserna J.J. 2000 Appl. Spectrosc. **54** pp 1429-1434.
- [12] Khater M. A. 2002 PhD thesis, Dublin City University, Dublin.
- [13] Doyle B. A. 1995 PhD thesis, Dublin City University, Dublin.
- [14] Asano Y, Iwamoto Y, Fukuyama K, Tamura N, Endo T, Namba S. 2018 IEEE Trans Plasma Sci. IEEE Nucl. Plasma Sci. Soc. **46** pp 2626-2629.

- [15] Harilal S.S, Diwakar P.K, Hassanein A. 2013 Appl. Phys. Lett. **103** pp 041102-041104.
- [16] Fortes F.J, Cabalín L.M, Laserna J.J. 2008 Spectrochim. Acta - Part B At. Spectrosc. **63** 1191-1197.
- [17] Jiang X, Hayden P, Costello J.T, Kennedy E.T. 2014 Spectrochim. Acta - Part B At. Spectrosc.**101** pp 106-113.
- [18] Shrivastava A, Gupta V.B. 2011 Chron. Young Sci. **2** 21-25.
- [19] Jiang X. 2012, PhD thesis, Dublin City University, Dublin.
- [20] Aguilera J.A, Aragon C, Campos J.1992 Appl. Spectrosc.**46** pp 1382-1387.
- [21] Aragon C, Aguilera J.A, Campos J.1993. Appl. Spectrosc.**47** pp 606-608.
- [22] Aragon C, Aguilera J.A, Penalba F.1999 Appl. Spectrosc.**53** pp 1259-1267.
- [23] Sturm V, Peter L, Noll R. 2000 Appl. Spectrosc.**54** pp 1275-1278.
- [24] Noll R, Bette H, Brysch A, Kraushaar M, Mönch I, Peter L, Sturm V. 2001 Spectrochim. Acta - Part B At. Spectrosc.**56** pp 637-649.
- [25] Hemmerlin M, Meilland R, Falk H, Wintjens P, Paulard L. 2001 Spectrochim. Acta - Part B At. Spectrosc.**56** pp 661-669.
- [26] Sturm V, Erben B, Fleige R, Wirz W. 2019 Opt. Express **27** pp 36855-36863.

Chapter 6 – Conclusions and Future Work

6.1 Introduction

The work reported in this doctoral thesis is an investigation of the different approaches to optimise the limit of detection (LoD) for carbon in steel plasmas using laser induced breakdown spectroscopy (LIBS). It was found that the LoD for trace amounts of carbon in steel, obtained via time integrated and space resolved (TI-SR) VUV LIBS, could be improved (up to a factor of six or so), by employing a line plasma source by substituting a point plasma source by a line plasma. It was also found that time resolved VUV detection (using single channel detection) resulted in an improvement in LoD by up to a factor of four over multichannel TI-SR VUV LIBS. The main findings and conclusions of the thesis are summarised in this final chapter. A few suggestions on potential future work are also outlined.

6.2 Summary and Conclusions

The main objective of this research was to develop a robust technique for the quantitative determination of trace amounts of carbon in steel using a VUV LIBS system [1,2,3]. Carbon has a large and mostly desirable effect on the material characteristics of steel with most steel making processes ideally having a specific C concentration along with other light elements (N, P, O, S) to determine mechanical and physical properties e.g., stiffness and ductility [4-6]. A slight variation in the quantity of these elements has a significant impact on the material traits of the steel, therefore the precise quantification of carbon in steel is highly desirable [6]. To this end, a large number of research studies have been carried out using optical emission spectroscopy (OES) to improve the emission signal from carbon ions using LIBS [7-9,11-17].

This technique has been widely used for the visible and UV regions, although a few experiments were also performed in the VUV region, however optimization of the limit of detection (LoD) is still a challenge. Therefore, in order to address this challenge, the current work is an effort towards the further improvement of the ability of LIBS for the quantification of light elements in metals, specifically here, carbon in steel. In this project the main emphasis was on the use of the C^{2+} line at 97.7 nm for classification/detection and also quantification. Two new variations on the VUV LIBS technique were investigated and further developed to improve the limit of detection of C in steel over single pulse VUV LIBS with time integrated detection, namely focusing the laser to a line for TI-SR VUV LIBS and time resolved or TR VUV LIBS. For these experiments the steel samples with a carbon content ranging from 0.05% to 0.9% (wt/wt %) were explored, which maps quite well onto the concentration range of interest in various types of industrial and technological steel products.

Chapters 1 and 2 are mainly concerned with setting out some of the fundamental properties of laser produced plasmas and the basic principles of LIBS. Chapter 3 describes the various experimental setup used along with the design of the basic single channel VUV detector built for the work reported in chapter 4 on TR VUV LIBS.

Chapter 4 describes a comparison of time integrated space resolved (TISR) and time resolved (TR) VUV LIBS. For time resolved experiments a single element detector comprising the combination of a scintillator and photomultiplier tube (PMT) was used. The limit of detection (LoD) results derived from this (single channel) time resolved VUV LIBS system were compared with the time integrated (multichannel) system at two distinct target positions, namely 2 mm and 4 mm from the optic axis. It was observed, as previously established, that the position of the target surface with respect to optic axis of the spectrometer plays an important role in optimising the signal to background ratio (SBR) in time integrated space resolved (TISR) VUV LIBS experiments [7,16]. Specifically, here, for time integrated

multichannel measurements, it was found that both the signal to background ratio (SBR) and the limit of detection (LoD) were improved when the target surface was placed at a distance of 4 mm from the optic axis of spectrometer compared to a 2 mm displacement from the spectrometer's optic axis (compare rows 1 and 2 in table 6.1). Although, when the target was placed at 2 mm away from optic axis of the spectrometer the limit of detection is low (table 6.1) but the calibration curve is not very smooth (figure 4.19) and coefficient of determination is also relatively lower than achieved by placing the target at 4 mm. Therefore, the limit of detection obtained at 2 mm position is less reliable. Coming to time resolved (TR) VUV LIBS an improved limit of detection and better signal to noise ratio was observed compared to both TISR VUV LIBS cases (compare row 3 with rows 1 and 2 in table 6.1). The improvement in LoD was a factor of 4 compared to the best point plasma VUV LIBS case.

Table 6. 1 Comparison of limit of detection and signal to background ratio of TISR (point plasma, line plasma) and TR (point plasma) for VUV LIBS

Row No.	Method (VUV) LIBS	R ²	LoD	Signal to Background Ratio
1	TISR at 2 mm (point plasma)	0.988	224 ppm	2.4
2	TISR at 4 mm (point plasma)	0.9998	316 ppm	2.8
3	Time resolved (point plasma)	0.9998	56 ppm	3.3
4	TISR (Line Plasma)	0.9998	50 ppm	4.4

In chapter 5, results on VUV LIBS with line focus plasmas were presented. The experiments were performed in time integrated-space resolved (TI-SR) mode, with multichannel (CCD) detection, using a vertically oriented cylindrical lens with the focal length

of 130 mm. The optimum optical emission was obtained when the target was displaced by a distance of 1 mm from the optic axis of the spectrometer. The limit of detection achieved using a line plasma is compared with other two techniques in table 6.1 where it can be seen that it is competitive with TR VUV LIBS achieving a limit of detection at the 50 ppm level.

In summary, for both point and line plasma sources, the experiments were spatially resolved which is a simple and effective method to exploit the space dependence of the laser produced plasma to ensure (at least close to) continuum free atomic and ionic emission line signals. The best results obtained for point plasmas were obtained when the target was placed at 4 mm from the optic axis of the spectrometer whereas for the line plasma the best results were obtained when the target was placed at 1 mm from the spectrometer optic axis. For line plasmas, aligned with the entrance slit of the spectrometer, the detected spectral signal to noise ratio improved and this led to a significant improvement in the limit of detection. Whereas, in the case of time resolved VUV LIBS it was possible to select time windows for both CIII (C^{2+} 97.7nm) line emission and nearby background emission (at ca. 104.4 nm), in the time interval of 0 to 230 ns, which optimised the signal to background ratio (SBR) and the limit of detection (LoD).

Two more studies are also included in the Appendices of this thesis, one, a preliminary depth profiling of aluminium thin films deposited on a silicon substrate and a second one, based on experiments performed in Padua at the Università di Padova, on UV-Vis LIBS of metals and semiconductors, to which a multivariate analysis was applied for the purposes of classification by element type.

In the depth profile study, aluminium thin films of different thicknesses, ranging from 0.0015 mm (1.5 μm) to 1 mm were used. The laser ablation rates for both high ($1.3 \times 10^{10} \text{ Wcm}^{-2}$) and low ($1.6 \times 10^9 \text{ Wcm}^{-2}$) intensity (irradiance) values on each Al thin film were

determined. By calibrating the system, the depth or thickness of unknown thickness of metallic thin films could be determined.

The second study was based on the application of multivariate data analysis for elemental classification in recycling of scrap metals and semiconductors. UV-Vis LIBS spectra for nine types of metals and semiconductors were obtained to which principal component analysis was applied. It was found that, using a very basic UV-Vis LIBS system combined with PCA classification, worked well for separating out the many metals studied and looks very promising for application to the metals industry as an economical separator.

6.3 Future Work

Focusing just on carbon in steel quantification there are many further experiments that can be done. Had time allowed further measurements on the effect defocusing below the target surface for line plasmas in TI-SR VUV LIBS mode could have been undertaken to confirm that focusing above the target provides the best SBR and LoD values (as it does in the point plasma case [7,16]. Further experiments on the effect of target surface location with respect to the optic axis of the VM521 spectrometer in time resolved (TR) VUV LIBS mode along with a lens defocus study are warranted.

The most obvious is to combine the advantages of single channel TR-VUV-LIBS with line focus plasmas. A more challenging experiment would be to extend the work to multichannel TR-VUV-LIBS by gating a VUV sensitive microchannel plate similar to the one used by Khater et al. [3] or by imaging the down converted image (spectrum) from a scintillator sheet onto a gated ICCD. Based on experience already at the laboratory, the former is likely to be the more sensitive detection approach, but both experiments would need to be carried out to confirm this.

Having determined the best combination of plasma focus and time/space resolved detection configuration it is clear that double pulse VUV LIBS could be explored for further LoD improvement. Although already studied for point focus plasmas in TI-SR-VUV-LIBS it remains to be explored for line focus plasmas combined with time resolved detection. To this authors' knowledge, there have been no studies of VUV LIBS using ultrafast (femtosecond pulsed) lasers in any mode (single/double pulse and with/without nanosecond pre-plasma or reheating pulses). In addition, for long wavelength VUV LIBS, the addition of e.g., a He or other gas, with an ionization potential larger than the photon energy of interest, can have the effect of improving both the emission intensity and limit of detection [3,8]. For DCU specifically, it has been clear that the performance of the key optical elements such as the grating has deteriorated over the decades and hence the best absolute values of the limits of detection can no longer be obtained. So new optics would benefit future experiments on VUV LIBS. Given the high sensitivity of VUV LIBS for low-Z elements it might also be worth extending LIBS for depth profiling applications studies in Appendix A to the VUV region by placing the samples in vacuum.

In relation to data analysis the application of chemometric-statistical techniques such as Principal Component Analysis, although mature in UV-Vis-NIR LIBS, should be applied in VUV LIBS. It was investigated in the work performed during the mobility period in Padova, and included in Appendix B. The PLS regression method, support vector machines, artificial neural networks and other machine learning techniques can also be used to train the system and use it for the identification and classification of unknown samples and also for the purpose of validation.

References

- [1] Hahn D.W, Omenetto N. 2012. Appl. Spectrosc.**66** 347-419.
- [2] Hahn D.W, Omenetto N. 2010. Appl. Spectrosc.**64** 335A-66A.
- [3] Khater M.A, Costello J.T, Kennedy E.T. 2002. Appl. Spectrosc. **56** pp 970-983.
- [4] Inagaki H. 1994. ISIJ int.**34** 313-321.
- [5] Park K.T, Kim Y.S, Lee J.G, Shin D.H. 2000. Mater. Sci. Eng. A. **293** 165-172.
- [6] Kim H, Suh D.W, Kim N.J. 2013. Sci. Tech. Adv. Mater. **12** Art. No. 014205.
- [7] Jiang X, Hayden P, Laasch R, Costello J.T, Kennedy E.T. 2013. Spectrochim. Acta Part B At. Spectrosc.**86** 66-74.
- [8] Khater M.A, Van Kampen P, Costello J.T, Mosnier J.P, Kennedy E.T. 2000. J. Phys. D. Appl. Phys. **33** pp 2252-2262.
- [9] Aguilera J.A, Aragon C, Campos J.1992. Appl. Spectrosc.**46** pp 1382-1387.
- [10] Shrivastava A, Gupta V.B. 2011. Chronicles of young scientists **2** pp 21-25.
- [11] Aragon C, Aguilera J.A, Campos J. 1993. Appl. Spectrosc. **47** pp 606-608.
- [12] Aragon C, Aguilera J.A, Penalba F. 1999. Appl. Spectrosc. **53** pp 1259-1267.
- [13] Sturm V, Peter L, Noll R. 2000. Appl. Spectrosc. **54** pp 1275-1278.
- [14] Noll R, Bette H, Brysch A, Kraushaar M, Mönch I, Peter L, Sturm V. 2001. Spectrochim. Acta Part B At. Spectrosc.**56** pp 637-649.
- [15] Hemmerlin M, Meilland R, Falk H, Wintjens P, Paulard L. 2001. Spectrochim. Acta Part B At. Spectrosc.**56** pp 661-669.
- [16] Jiang X, Hayden P, Costello J.T, Kennedy E.T. 2014. Spectrochim. Acta Part B At. Spectrosc.**101** pp 106-113.
- [17] Sturm V, Erben B, Fleige R, Wirz W. 2019. Opt. Express. **27** pp 36855-36863

Appendices

Appendix A

LIBS Application for Thin Metallic Films

A1. Introduction

Technological advancements in the last few decades have resulted in widespread use of thin films in various industrial sectors [1-4]. Thin films are commercially used as coatings for optical components [5], as sensing materials in the chemical industry [6,7] and insulating/conductive coatings for electrical devices [8]. The efficiency of thin films in any application depends upon the uniform deposition on the substrate. Several analytical techniques are used by industry and research groups for characterisation of thin film deposition. Depth profiling is an important parameter that provides meaningful information about the uniformity of material deposited on a substrate.

In this work Vis-NIR LIBS was explored for the depth profiling of aluminium on silicon thin films. Thin aluminium films were irradiated at high and low laser irradiances to ablate aluminium in air. This technique is useful for onsite applications as there is a very simple setup used. This appendix includes a description of the equipment used in this experiment along with the outcome of the laser ablation and crater formation. Crater size was determined by optical microscope and 3d microscope. The results arising from depth profiling by recording emission spectra in the visible and near infrared regions of the spectrum are also presented along with some comments.

A2. Experimental Procedure

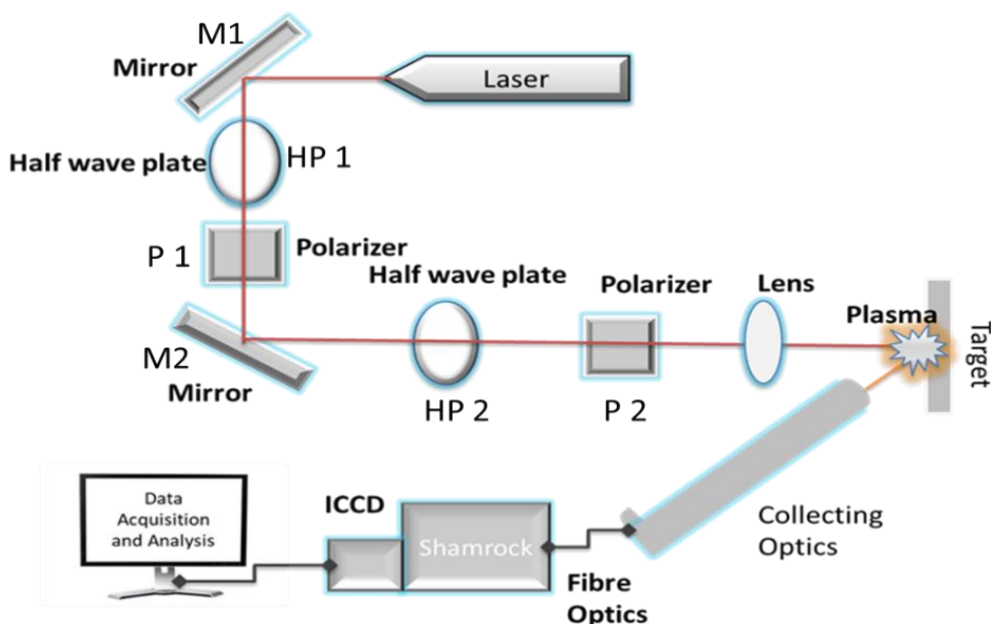


Figure A 1 LIBS setup for the aluminium thin film experiments.

The experiments on depth profiling of metal targets were performed using a simple UV-Vis LIBS system. Figure A1 shows a schematic of the experimental setup where thin aluminium metallic films were irradiated with focused laser pulses in air. A commercially available Nd:YAG laser (Continuum Surelite III-10, pulse width 6.0 ns, wavelength 1064 nm, linear polarisation and energy up to 650 mJ) was used. The laser pulses were focused to a small spot, $<100\ \mu\text{m}$ in diameter, on the metal target using a specially designed optical system. This optical system is composed of plane mirrors, half wave plates, polarizers, and a focusing lens. The first mirror M1, set at an angle of 45 degrees, is used to transport the laser beam to the halfwave plate and polarizer (HP1 and P1). This combination is used to provide gross control over the laser energy, ensure maximum linear polarization and provide a good beam profile. The second mirror M2 was again set at an angle of 45 degrees to direct the laser beam to the second half wave plate (HP 2) and polarizer (P2). This combination is used to give fine control

of the pulse energy while ensuring a continued high degree of linear polarisation. A plano-convex lens with a diameter of 2.5 cm and 100 mm focal length was used to focus the laser pulse down a spot size of $\approx 40 \mu\text{m}$ diameter. Two different power density levels were used namely $1.3 \times 10^{10} \text{ Wcm}^{-2}$ and $1.6 \times 10^9 \text{ Wcm}^{-2}$ with corresponding pulse energies measured as 1.46 mJ and 0.2 mJ on power meter.

The laser was used in single shot mode. Each laser pulse irradiated the aluminum thin film metallic target surface which resulted in the formation of a plasma plume. The plasma radiation was collected using simple collection optics, which was comprised of two spherical plano-convex lenses, each with a diameter of 5 cm. The collected plasma radiation was delivered to a compact Czerny-Turner spectrometer (Andor Shamrock SR-163) using an optical fiber. The spectrometer featured a 163 mm focal length and f/3.6 numerical aperture. The spectrometer was equipped with an Andor Technology model DV434 ICCD Camera with 1024×1024 pixels. Each pixel has an area of $13 \mu\text{m} \times 13 \mu\text{m}$. The spectrometer was operated at a slit width of $50 \mu\text{m}$ and provided a spectral resolution of 0.46 nm. Wavelength drive is operated using manual micrometer screw gauge which is calibrated at 1200 lines/mm to read 1 nm for a conversion of $10 \mu\text{m}$ on the gauge. A wavelength range of $\sim 60 \text{ nm}$ could be captured for a fixed centered wavelength or (micrometer screw gauge) position. The intensified CCD camera has a very fast gate times as low as 3 ns.

The aluminium thin films were deposited with different thicknesses on the silicon substrates to form sample targets for the LIBS measurements. In the first experiment, a single laser pulse irradiated an aluminium coated silicon substrate that was placed in the target holder. The thickness of the film was $15 \mu\text{m}$ which was measured through micrometer screwgauge. The laser irradiance was $1. \text{ Wcm}^{-2}$. Radiation from the resultant laser produced plasma was dispersed by the spectrometer, recorded by the ICCD and the spectrum was analysed using a simple MATLAB code. Figure A2 shows the spectrum of an aluminium thin film on a silicon

substrate in the spectral region between 385 nm and 405 nm. At 390.55 nm, the spectral line for Si (I) corresponding to the transition between two excited states, namely $3s^23p4s$ (1P_1) at 5.08 eV and $3s^23p^2$ (1S_0) at 1.91 eV was observed. The spectral lines of Al (I) appeared at 394.40 and 396.15 nm arising from transitions between the $3s^24s$ ($^2S_{1/2}$) [3.14 eV] and $3s^23p$ ($^2P_{0.5,1.5}$) [0, 0.1 eV] states, respectively.

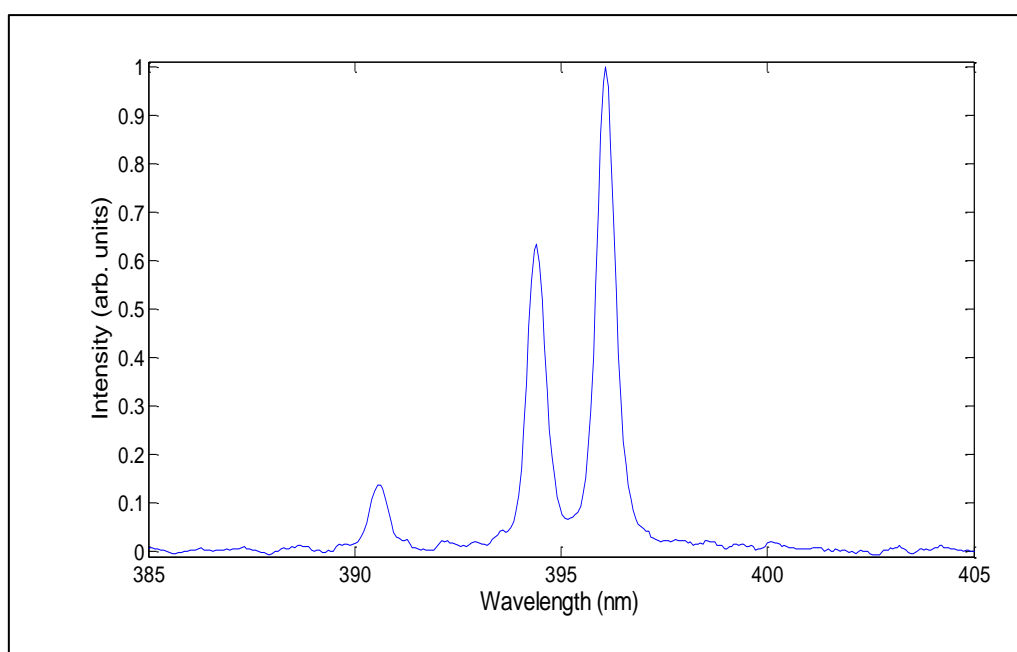


Figure A 2 LIBS spectrum recorded for a thin Al film on Si. The lines observed for Al lie at wavelengths of 394.4 and 396.15 nm, while a Si line is present at 390.55 nm. All three lines arise from the neutral (atomic) species.

A3. Laser Ablation at Low Power Density

The same experiment was performed using a lower laser power density of $1.6 \times 10^9 \text{ Wcm}^{-2}$. In this case there was very little continuum emission, so a time integrated measurement could be used for simplicity. Figure A3 shows the Al line intensities (integrated over both lines) for Al thin films with different thicknesses. In the case of the low power density, the 1 mm film did

not show complete ablation even after the 160 shots and an increase in the intensity was observed (red line figure A3). This behaviour has been observed in the past [9] and is the result of plasma plume confinement by the crater formed after multiple laser shots are fired on a single position of the target surface. The increase in intensity depends on the geometry of the crater or hole formed and a number of systematic studies of such confinement have been made [10 and references within]. In summary it is believed that the confinement results in an increased collision rate amongst the plasma constituents (compared to free expansion of the plasma plume) which leads in turn to an increased optical emission rate and intensity. In the case of 45 μm thick film, after closer to 80 laser shots, the aluminium intensity of both lines dropped to almost zero. The 30 μm thin film aluminium was completely ablated after around 60 laser shots and the 15 μm thick film after about 30 laser shots. In the case of the 1.5 μm thin film, the aluminium appeared to have been completely ablated after 3 shots. The ablation rate calculated for the low power density case, using the results obtained from the experiments, was found to be in the range 0.51 - 0.66 $\mu\text{m}/\text{shot}$. It should be noted that due to the higher excitation energy required to produce the Si I line emission the silicon line intensity was difficult to acquire at the lower power density (figure A4). The ablation data are summarised in Table A1.

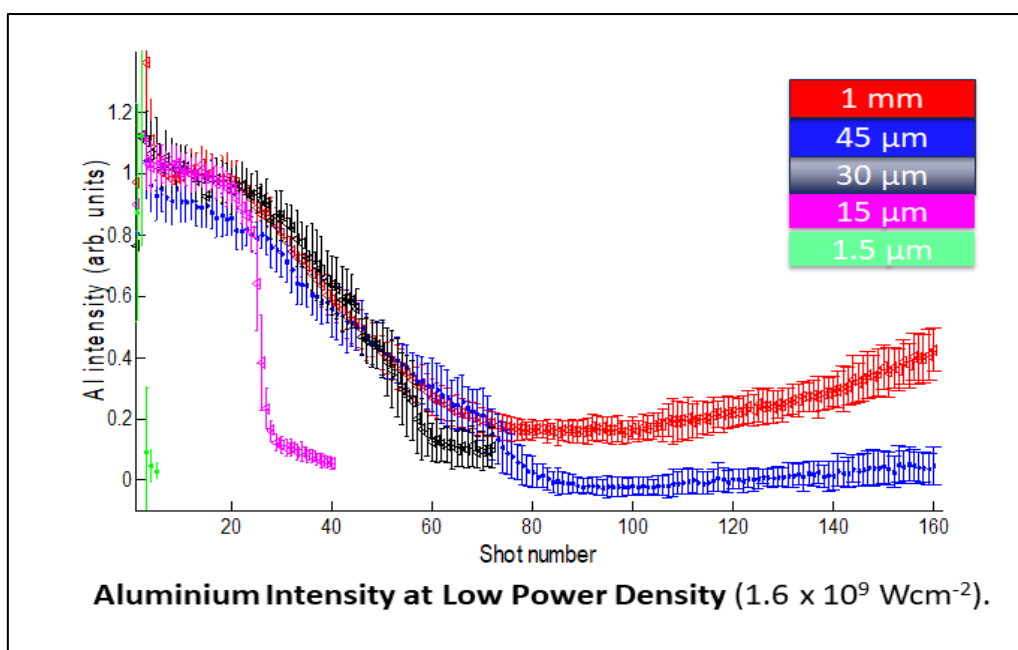


Figure A 3 Aluminium line intensity (integrated over both lines at 304 nm and 396 nm) measured at a low power density ($1.6 \times 10^9 \text{ Wcm}^{-2}$) for different film thicknesses.

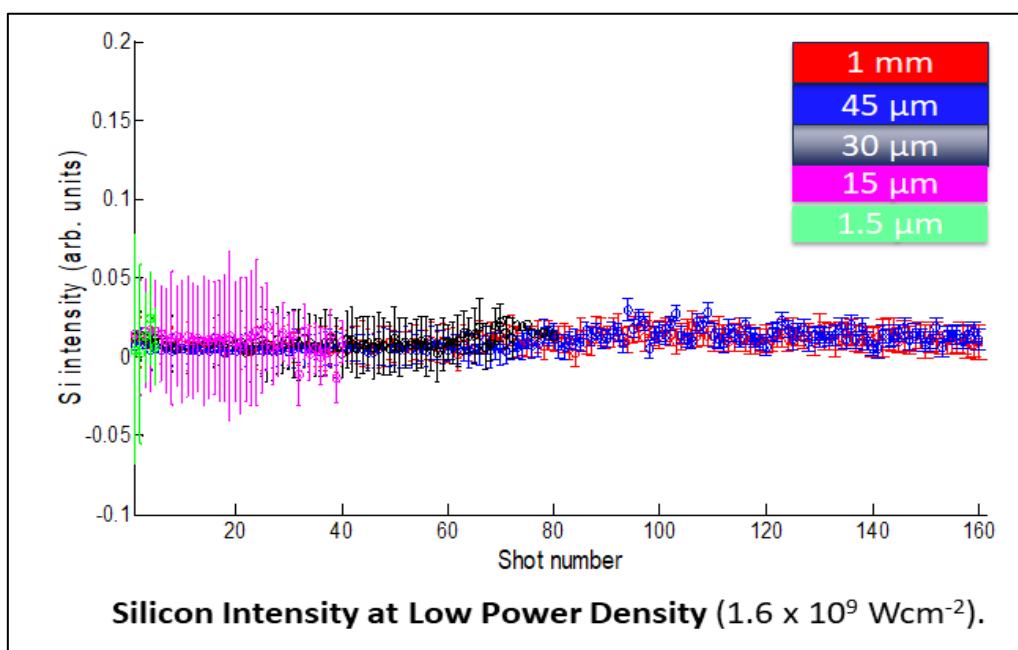


Figure A 4 Silicon line intensity measured at a low power density ($1.6 \times 10^9 \text{ Wcm}^{-2}$) for different film thicknesses.

Table A1 Number of laser pulses required for complete ablation of aluminium thin films from a silicon substrate using a low laser power density.

Target Thickness	Ablation Counts (No of shots)
1 mm (Red)	Above 160 shots
45 μm(Blue)	80 shots
30 μm(black)	60 shots
15 μm (Magenta)	30 shots
1.5 μm(Green)	3 shots

A4. Laser Ablation at a High-Power Density

Al films with thicknesses of 1.5 μm , 15 μm , 30 μm , 45 μm , and 1 mm were also irradiated with high power density laser pulses ($1.3 \times 10^{10} \text{ Wcm}^{-2}$) until the deposited Al was totally ablated from the silicon substrate (except in the 1 mm thick case where material remained after > 160 shots). At this power density there was significant continuum emission for the early stages of the plasma lifetime. Hence a gate delay of 50 ns and a gate width of 130 ns was required for the ICCD detector to obtain line emission with a low background. Figure A5 presents the aluminium doublet line intensity recorded for different thicknesses at the higher power density as a function of the number of laser pulses incident on to the target. The intensity of the both Al lines for the 1.5 μm thick film dropped to zero after the first shot and remained at this value for the rest of the ten shots used.

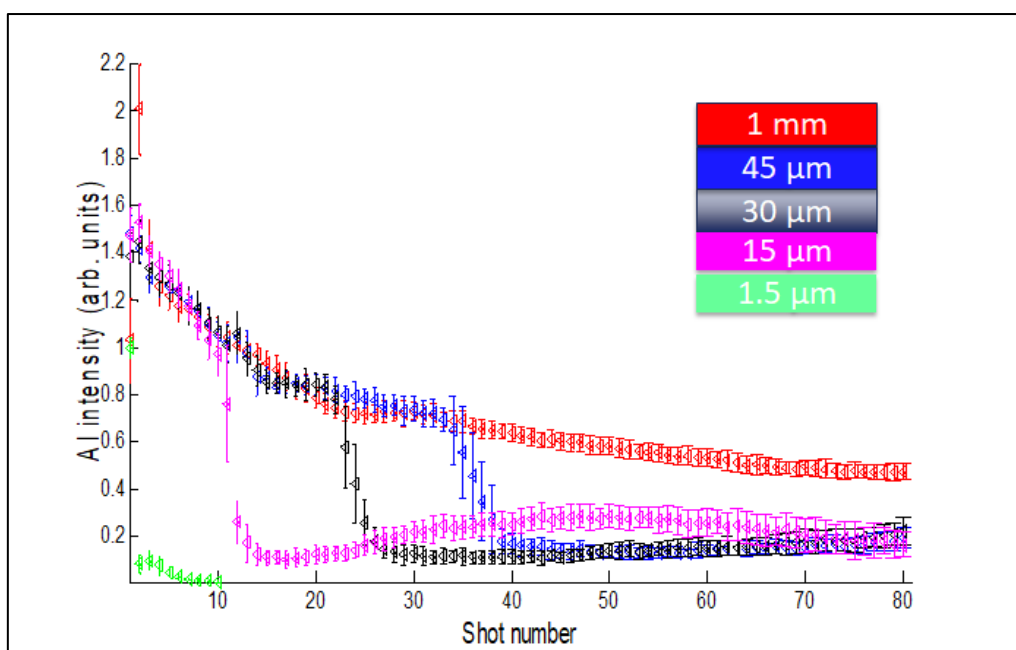


Figure A 5 Aluminium intensity measured at higher power density ($1.3 \times 10^{10} \text{ Wcm}^{-2}$) for different film thicknesses.

For the next sample with an Al film thickness of $15 \mu\text{m}$, complete ablation of the deposited material was observed after about 15 laser pulses. For the sample, with a thickness of $30 \mu\text{m}$, after about 30 laser pulses the deposited material was completely ablated. The sample with $45 \mu\text{m}$ Al was completely ablated after 40 laser pulses. The Al intensity of both lines measured by first laser pulse for the last sample with 1 mm thickness was higher compared to other samples. The Al intensity of both lines dropped to 50% after irradiation with 80 laser pulses, the maximum number used.

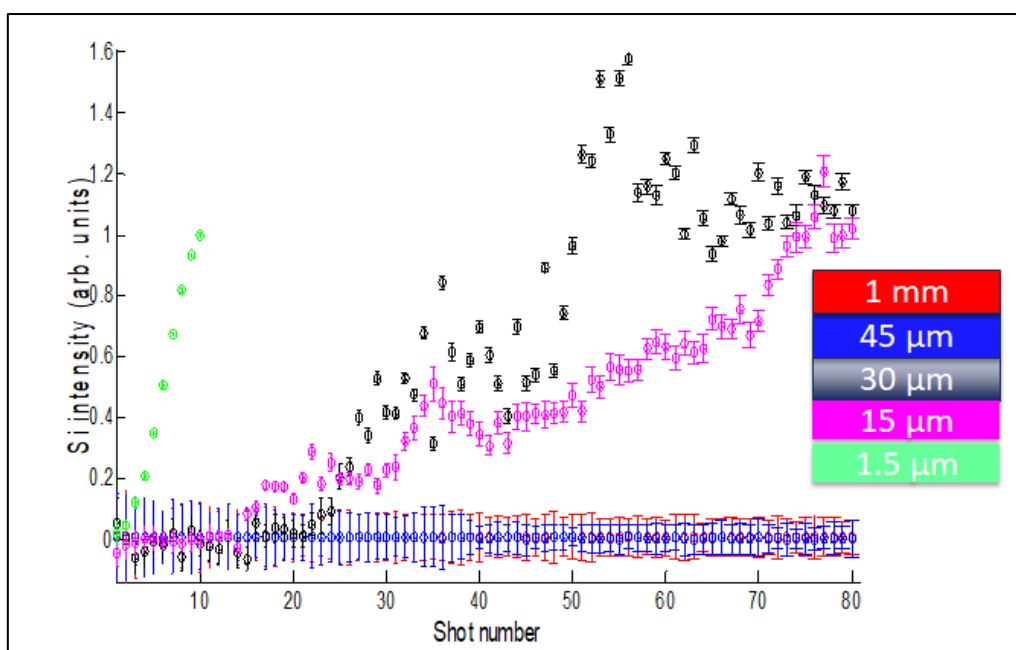


Figure A 6 Silicon substrate intensities measured at higher power density ($1.3 \times 10^{10} \text{ Wcm}^{-2}$) for different film thicknesses.

Figure A.6 shows the intensity of emission from the silicon substrates. The appearance of the silicon just after the complete ablation of the aluminium films verifies the observation made above. For the thickest aluminium layers (1 mm and 45 μm samples) the silicon line was not observed, after 80 laser shots in succession (albeit the Al I emission started to be disappeared after ca. 45 shots in 45 μm). However, in case of the 30 μm Al thin film sample, the silicon appeared just after 23rd scan and its intensity increased thereafter. For the 15 μm thick film, after 13 laser shots the intensity of Si I line began to increase whereas for the 1.5 μm film the silicon line was observed after the first shot and its intensity increased after that.

Table 2 shows the summarised results obtained for different thin films and relative number of laser pulses for complete ablation of the films. The ablation rate was calculated by using the ratio between the number of shots at the point of complete ablation and the thickness of the target film. Using the results obtained from the experiments, the ablation rate for Al thin

films using the higher laser power density was calculated and found to lie in the range of 1.15 – 1.70 $\mu\text{m}/\text{shot}$.

Table A 2 Number of laser pulses required for complete ablation of aluminium thin films from silicon substrates obtained from Al I spectral emission measurements.

Target Thickness	Ablation Counts (No of shots)
1 mm (Red)	Above 80 shots
45 μm (Blue)	40 shots
30 μm (black)	30 shots
15 μm (Magenta)	15 shots
1.5 μm (Green)	1 shot

A5 Depth Profiling

A5.1 Crater Analysis using Optical Microscopy

A crater was observed on the surface of the thin films after the first shot at $1.3 \times 10^{10} \text{ Wcm}^{-2}$. The crater size was measured using an optical microscope (Olympus IX81). It had a resolution of 0.2 microns.

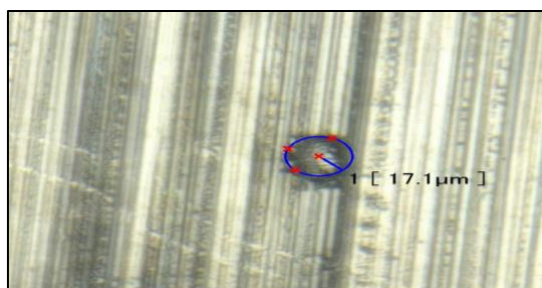


Figure A 7 Crater size after the 1st shot on the 15 μm Al film.

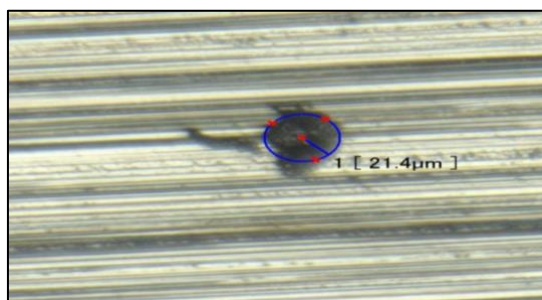


Figure A 8 Crater size after 20 shots on the 15 μm Al film.

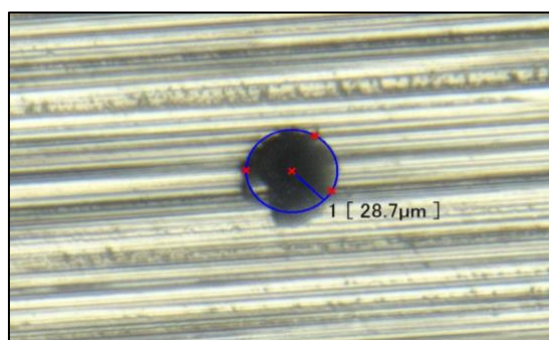


Figure A 9 Crater size after 30 shots on the 15 μm Al film.

The above figures (A9 - A11) show the images of the crater formed as a result of irradiation with different numbers of laser pulses on the 15 μm aluminium film, at the higher pulse power density. The crater diameters for each case are given in Table A3 below. The diameter of the crater is measured to be 17.1 μm after the 1st shot and then it is increased to 21.4 μm after 20 shots where it shows further increment upto 28.7 μm after 30 shots. Hence the crater diameter is increased slowly after 1st 20 shots from 17.1 μm to 21.4 μm which is an increment of 4.3 μm in total. Or diameter is increased 0.215 μm per shot in 1st 20 shots. After 21st to 30 shot there is a rapid increment of diameter of 7.3 μm which shows increment of 0.73 μm per shot.

Table A 3 Crater size with respect to number of shots on 15 μm Al film

Number of Shots	Crater Size
1 st	17.1 μm
20	21.4 μm
30	28.7 μm

A5.2 Crater Analysis Using a Light Tight Test

To verify the complete ablation of aluminium thin films a light tight test was conducted. Each irradiated film was back illuminated, and images were taken to check if transmitted light could be observed. Three consecutive shots were taken on the 1.5 μm thin film, at the higher pulse power density. In figure A12 the leftmost position represents a vertical line with 3 single shot

exposures; the middle position shows two shots per exposure; the holes in the rightmost position are the result of 3 shot exposures. Here it is evident that light cannot pass after 1st shot and the aluminium was not completely ablated.



Figure A 10 Light test conducted after the accumulation of 1 to 3 shots for the 1.5 μm thin Al film.

Summary

In this chapter the ablation rate of aluminium thin films at high and low radiances was determined and discussed. Crater morphology was also studied using an optical microscope. This study confirms that LIBS is useful for the determination of ablation rate and depth profiling of the metallic thin films.

References

- [1] Acquaviva S, D'Anna E, De Giorgi M.L, Moro F.2006. Spectrochim. Acta - Part B At. Spectrosc.**61** pp 810-816.
- [2] Caneve L, Colao F, Sarto F, Spizzichino V, Vadrucchi M. 2005. Spectrochim. Acta - Part B At. Spectrosc.**60** pp 1098-1102.
- [3] Davari SA, Hu S, Pamu R, Mukherjee D. 2017. J. Anal. At. Spectrom. **32** pp 1378-1387.
- [4] Aragon C, Madurga V, Aguilera J.A. 2002. Appl. Surf. Sci. **197** pp 217-223.

- [5] Piegari A, Flory F 2018. Optical Thin Films and Coatings: From Materials to Applications. Woodhead Publishing (ISBN 9780081020999).
- [6] Yang M, Sun Y, Zhang D, Jiang D. 2010. Sensor Actuat B-Chem **143** pp 750-753.
- [7] Olvera M.D, Asomoza R. 1997. Sensor Actuat B-Chem **45** pp 49-53.
- [8] Hecht D S, Hu L, Irvin G. 2011. Adv. Mater. **23** pp 1482-513.
- [9] Corsi M, Cristoforetti G, Hidalgo M, Iriarte D , Legnaioli S, Palleschi V, Salvetti A and Tognoni E. Appl. Spectrosc. **59** pp 853–860 (2005).
- [10] Su X, Zhou W and Qian H. Optics Express **22** pp 28437-28442 (2014).

Appendix B

Multivariate Analysis of UV LIBS Spectra of Scrap Metals and Non-Metals

B1. Introduction

This chapter is focused on the application of Laser Induced Breakdown Spectroscopy (LIBS) to the metal recycling industry as a tool for identification and classification of scrap metals. LIBS is a robust technique which has been widely used for the analysis of metals for decades. In case of quantitative analysis sometimes calibration curve become difficult to interpret and understand, mainly due to the matrix effects. [1] These can include issues like line overlapping or blending and opacity. Multivariate analysis is used to remove these affects from the spectra and to classify and quantify the component matrix in more comprehensive way [2-7].

In this chapter scrap samples of metals and semiconductors are studied using a PCA classifier and also the identification of unknown matrices becomes possible. The experimental setup, methodology and details of equipment used to perform these experiments is described. The experiments are performed in ultraviolet-visible-near infrared (UV-Vis-NIR) region, in the spectral range from 200 nm to 850 nm. There are seven different metals which were explored using LIBS, followed by classification and identification of alloys of those metals based on Principal Component Analysis (PCA). This appendix also includes an analysis of silicon, carbon and silicon carbide LIBS spectra using PCA.

B2. Experimental Procedure

A very simple LIBS setup was used as shown in figure B2.1. A compact Brilliant B Nd:YAG laser was used with a pulse energy of 0.13 Joules and 0.75 Joules. The corresponding peak power densities were ca. $4.8 \times 10^9 \text{ W.cm}^{-2}$ and $4.6 \times 10^{10} \text{ W.cm}^{-2}$. The laser beam was guided via a mirror (M1) to a convex spherical Lens (L1) with 100 mm focal length to the target holder where the sample was placed and ablated. Radiation from the resulting plume was then focused onto the spectrometer slit via a simple 50mm convex spherical lens which acted as the collecting optic. The compact spectrometer (Ocean Optics, Model USB 2000+) was used to record spectra. The details of the experimental setup are given in a little greater detail below.

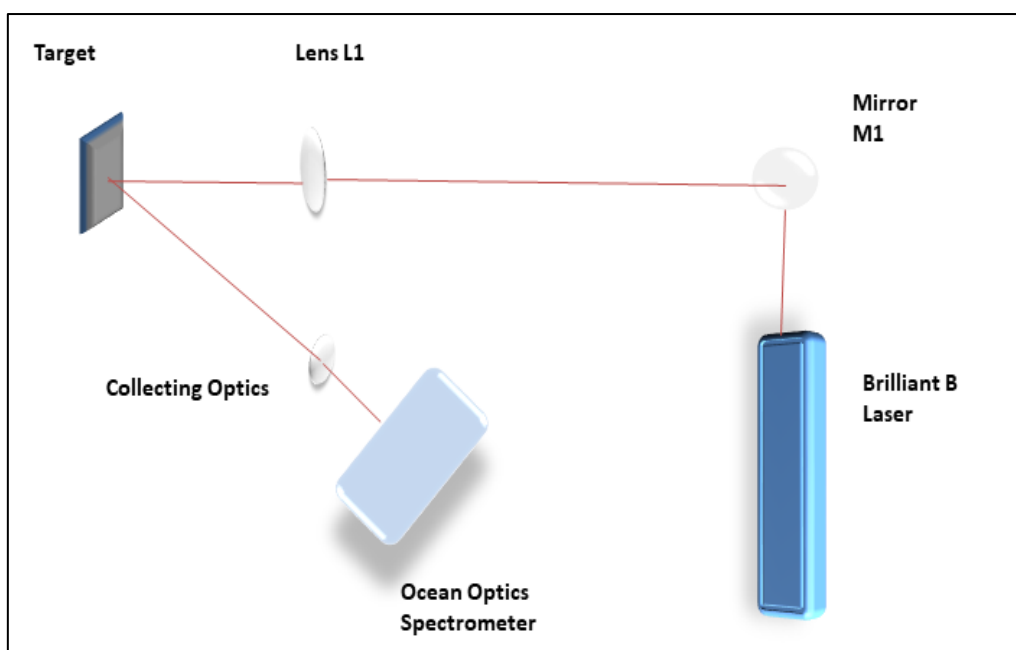


Figure B 1 Schematic Diagram showing the Time Integrated UV Vis LIBS setup.

B 2.1 Quantel ‘Brilliant b’ Laser

For these set of experiments a Quantel Brilliant b laser was used, a high power, but compact, Q switched Nd:YAG oscillator with a super gaussian resonator. It has a beam diameter of 9 mm. The Nd:YAG laser rod is pumped by two flashlamps cooled by an air or water/water heat exchanger. It has the possibility to add a harmonic generator for operation at 532 nm or 355 nm. A photograph of the laser head is shown in figure B2 mounted on an optical table with the beam steering mirror M1 visible. Its basic parameters are included in Table B1.



Figure B 2 Quantel ‘Brilliant b’Nd:YAG laser used in the Padova experiments.

Table B 1 Basic parameters of the Q switched Laser system.

Wavelength (nm)	1064
Energy(mJ)	900 mJ (max)
FWMH (ns)	6
Repetition Rate (Hz)	10/single shot
External Trigger Jitter(ns)	≤ 0.5

B2.2 Spectrometer and Detector

For these experiments an Ocean Optics USB2000+ asymmetric crossed Czerny Turner spectrometer was used. Light from the plasma plume was guided to the spectrometer via an optical fiber. It is a miniature spectrometer pre-configured for UV-VIS measurements with optical resolution of 1.5 nm FWHM. It covers a wide range of wavelength from 200 to 850 nm. Its integration time can be varied via the control software from 1 millisecond to 65 seconds and it can be synchronized to other devices by means of external triggering functions. A Sony ILX511B (2048-element linear silicon CCD array) is used to detect the dispersed radiation in the spectrometer which has a diffraction grating with a groove density of 600 lines/mm and is operated with a slit of width 25 μ m.

B2.3 Samples

Seven metallic samples and three non-metallic samples were included in the study. LIBS spectra obtained by these experiments were then further subjected to Principal Component Analysis. These spectra were used for the classification of different scrap metals and also as training sets for PCA to help with the identification of different alloys containing these metals.

Table B 2 Samples used for LIBS analysis and PCA.

Zinc (Zn)	Ag (Silver)	SiC (Silicon Carbide)
Ta (Tantalum)	Lead (Pb)	Silicon (Si)

W (Tungsten)	Carbon (C)	Mo (Molybdenum)
--------------	------------	--------------------

B3. Methodology

For these experiments each sample was ablated with the laser energy of 130 mJ with pulse width of 6ns and a power density or irradiance of ca. $0.5 \times 10^{10} \text{ W/cm}^2$. Each sample was moved slightly after 5 shots to reduce cratering and to ensure representative results for the whole sample. The spectrometer was set to record emission spectra within the UV-VIS-NIR range from 200 to 850 nm. The spherical convex lens was positioned to ensure that the laser focus was set at 10 mm behind the ablation (sample) surface. All the samples were irradiated with the focused laser pulses in air as shown in figure B1, 14 shots were taken for every sample at different positions by randomly moving the sample. The output spectrum was stored and displayed by the Ocean Optics ‘Ocean View’ software package. The average of 14 spectra was taken and all spectra were subjected to multivariate analysis, in this case Principal Component Analysis (PCA).

Before performing PCA, the first step is to normalise all experimental spectra to lie within the same intensity range which was chosen to be between 0 and 1. It is critical to perform this step because PCA is very sensitive to the ranges of the intensity values in the data sets (i.e., spectra).

Every spectrum contains 2048 pixels with the x axis (pixel number) defining the wavelength and the y axis (pixel value in counts) representing intensity. The normalization was performed on every spectrum pixel by pixel by dividing each pixel count (intensity) by the maximum intensity value in that spectrum, so that all pixel (spectral) intensity value lay between 0 and 1. For this purpose, a MATLAB code was written and the resulting normalised spectra (amounting to 126 in total for all nine samples) were saved. Following data normalization, the second step is the computation of the covariance matrix.

The covariance matrix is a $p \times p$ symmetric matrix of the (where p is the number of dimensions) with the covariances associated with all possible pairs of initial variables as entries. For example, for a 3-dimensional dataset with three variables (x, y, z), the covariance matrix is expressed as follows:

$$\begin{bmatrix} Cov(x, x) & Cov(x, y) & Cov(x, z) \\ Cov(y, x) & Cov(y, y) & Cov(y, z) \\ Cov(z, x) & Cov(z, y) & Cov(z, z) \end{bmatrix}$$

As the covariance of a variable with itself is its variance ($Cov(x, x) = Var(x)$), the variances of the initial variables lie along the main diagonal. Also, due to the commutative property of covariance ($Cov(x, y) = Cov(y, x)$), the corresponding entries in the covariance matrix are symmetric with respect to the main diagonal. It should be noted that the signs of covariances matter, a positive value indicates positively correlated variables while a negative sign indicates an anti-correlation. Hence the covariance matrix is a table that summarises the correlations (positive and negative) between all the possible pairs of variables.

In the first set of results shown in section B 5.1 (Fig. B 12) using 42 spectra, i.e., 14 each for Mo, Ag and Ta, is used a covariance matrix was formed. The next step is then to calculate the eigenvectors and eigenvalues of the covariance matrix to determine principal components (PC) of the data. The principal components are the set of new variables that are created by making linear combinations of the initial variables. These new variables are formed in combinations that they are largely uncorrelated and most of the information is compressed into the first component. So, a 'm-dimensional' dataset gives 'm' principal components, but the PCA methodology tries to force as much information as possible into the first component, then maximum remaining information into the second and then into the third and so on. Therefore, the distribution of information this way will allow to reduce dimensions of the data

while minimising the information lost. This is done by discarding the principal components with the lowest information content.

In these experiments, three dimensional PCA was used which was obtained by acquiring the eigenvectors and eigenvalues of first three columns of the covariance matrix. In the final step the aim is to calculate the score assigned to each spectrum from the feature vector. The feature corresponds to the eigenvectors of the matrix which is formed by taking the product of the covariance matrix and the transpose of original data matrix. The above is expressed mathematically as follows:

Let A be the input matrix, where each row is a recorded spectrum (i.e., a list of intensity values for each wavelength or pixel). If 'n' spectra are chosen, then A is a 'n x 1024' matrix for a 1024 pixel spectrum. The covariance matrix, M, is generated by computing the transpose of A, (designated A^T , now a '1024 x n' matrix) and multiplying it by A, i.e.,

$$M = A^T \times A$$

V is designated as the set of eigenvectors, sorted by eigenvalue magnitude, of the covariance matrix. T_k is designated as the 'principal component score' and the corresponding values are used as the co-ordinates of points that represent the input spectra, i.e.,

$$T_k = A \times V_k$$

where V_k contains only the first k columns of the matrix V. In the current case the first three principal components are taken, i.e., k=3. For spectra with 1024 pixels, V_k is then a 1024 x 3 matrix.

This step results in the original data being reduced to, or represented by, its three principal components PC1, PC2, PC3 in this case which can then be plotted in three dimensional space. Moreover a Gaussian ellipsoid was also plotted for every sample to form a statistical

boundry based on mean, mid point and standard deviation of the data to find outlier spectra. Each ellipsoid creates a boundry to find any statical outliers for the specific set of data. The elements within the ellipsoid are considered correlated or in other words, they belong to the same 'class'. In this way PCA acts as a classifier for the data, in this case correlating LIBS spectra with the target material giving rise to each spectrum the data set being used to construct the matrix 'A'.

In this preliminary study, three separate analyses were performed. In the first set, scrap metal spectra were classified along with spectra of pure samples of carbon, silicon and silicon carbide (section B 5.1). In a second exercise the focus was on the identification of elements, in this case carbon, silicon and also the material silicon carbide. The PCA classifier was run 14 times using a new single silicon carbide spectrum each time to see if this spectrum is equidistant (each time) from silicon and carbon (section B 5.2). The third study was performed using six different scrap metal samples where 84 spectra were divided into two sets of 60 and 24 spectra. The first set of 60 spectra was divided into 6 subsets, each containing 10 training spectra, one for each metal sample. The subsets were then used to train the PCA classifier while the remaining 24 (4 spectra for each of the 6 samples) were used as test spectra.

B4. LIBS Analysis of Different Materials

B4.1 UV-Vis Spectra for Metallic and Semiconducting Samples

UV-Vis spectra for each scrap sample were obtained under the same experimental conditions from which an average spectrum for each sample could be obtained. In what follows, LIBS spectra are divided into two categories, namely, metals which include metallic conductors along with carbon, and semiconductors including silicon and silicon carbide. The spectra were used to identify elements present in these materials by comparing spectral lines corresponding

to each element present in the sample to previously classified transitions in the NIST ‘Atomic Lines’ database.

Carbon

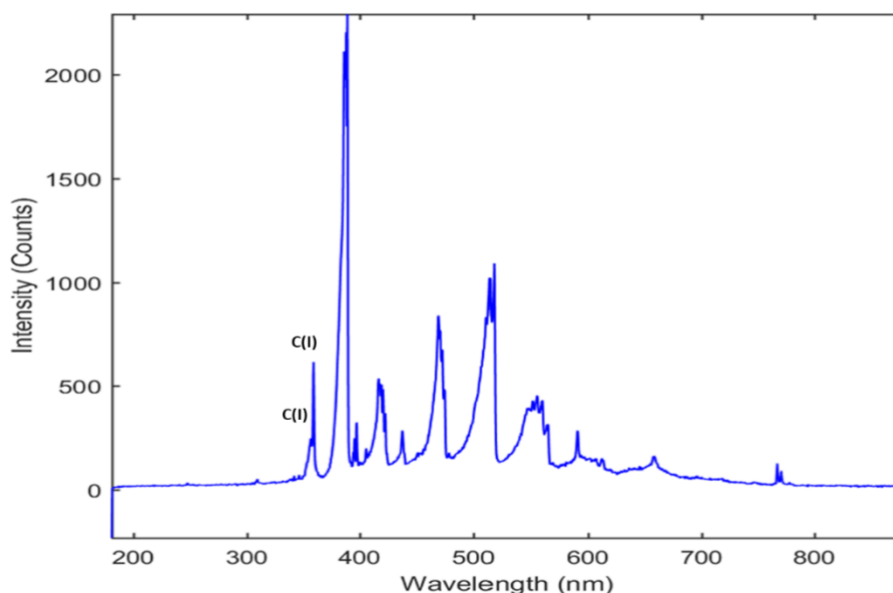


Figure B 3 Carbon (C) spectrum (14-laser shot average).

The average carbon spectrum (figure B3) shows the carbon lines in UV and Visible range from 280 to 800 nm. The C(I) lines at 359.51 nm and 359.55 nm corresponding to transitions $2s^22p3s (^3P_1) - 2s^22p7p (^3P_0)$ and $2s^22p3s (^3P_2) - 2s^22p7p (^3P_2)$ are observed as a single unresolved feature located at a wavelength of ~359 nm in the spectrum. The series of unresolved C (III) lines ranging from 388.38 nm to 388.97 nm (located at 388.7nm on the spectrum) is used for the confirmation of carbon lines in the sample.

The average tantalum spectrum is shown in figure (B4) on the following page. There are some weak tantalum lines sitting on the broad continuum feature. Once again, the strongest features can be identified on the spectrum according to the measured wavelength using the NIST Atomic Lines Database and labelled. As for carbon many of the features are blended and

the measured wavelength corresponds to the peak intensity of the observed feature. The spectra for the remaining samples are all shown in the following pages. Since the idea is to apply PCA to classify elements, lines are not explicitly labelled. The spectra are shown only for information.

Tantalum

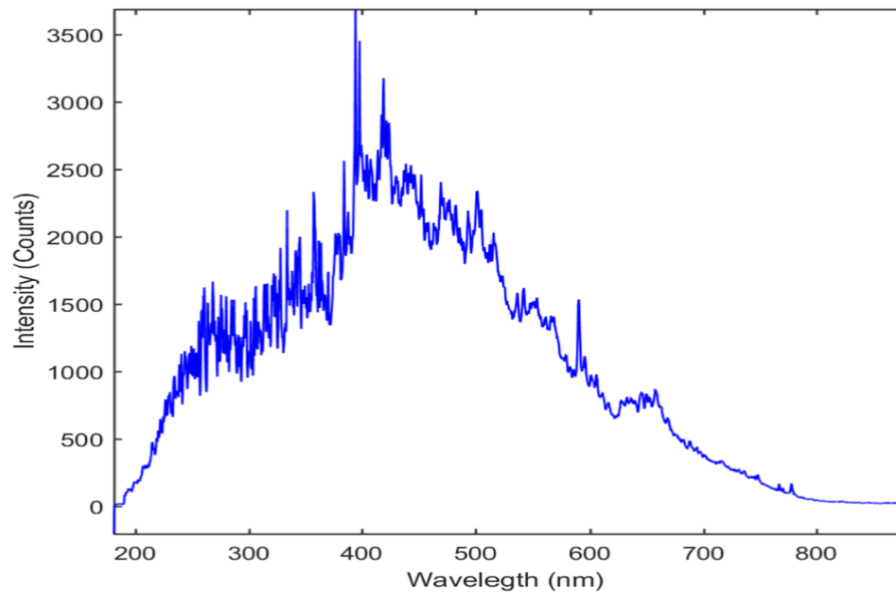


Figure B 4 Tantalum spectrum (14-laser shot average).

Silicon

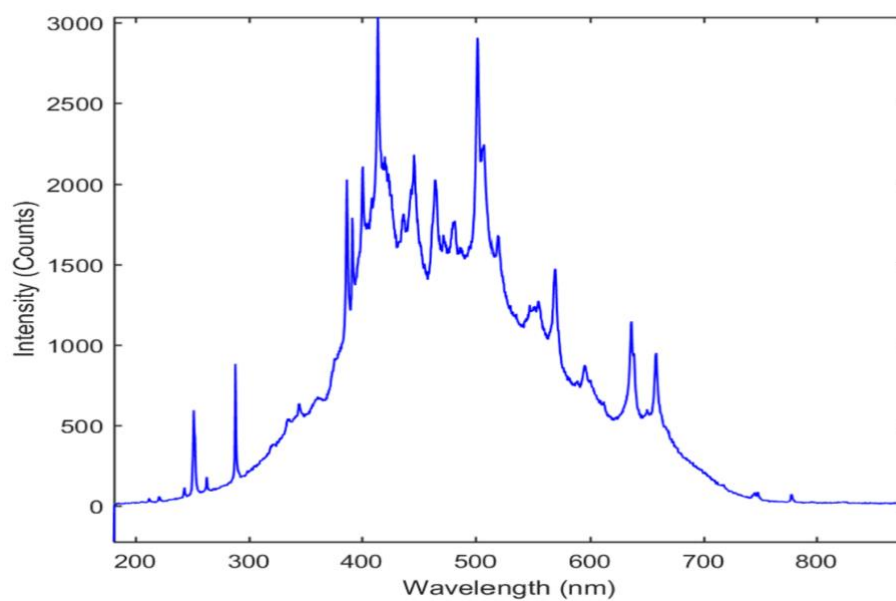


Figure B 5 Silicon spectrum (14-laser shot average).

Silicon Carbide (SiC)

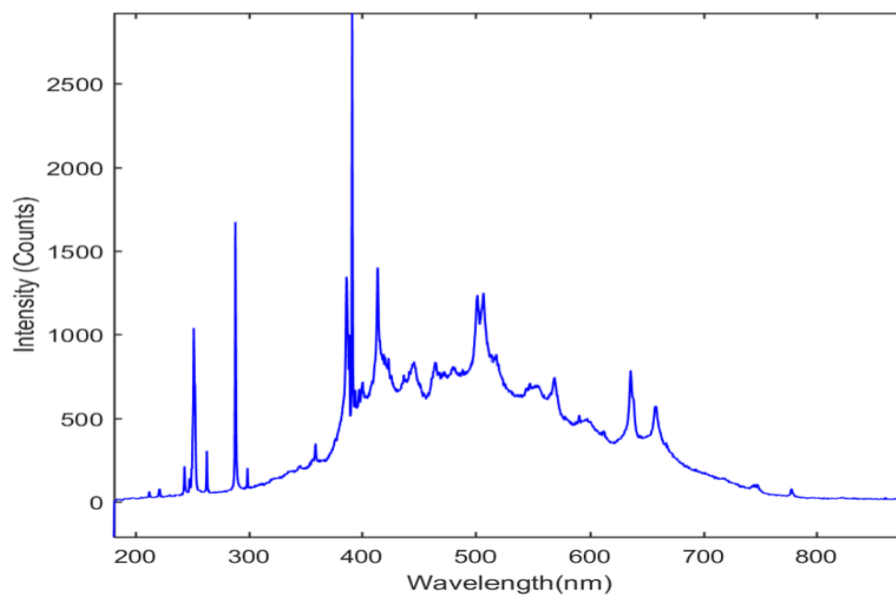


Figure B 6 Silicon Carbide (SiC) spectrum (14-laser shot average).

Lead (Pb)

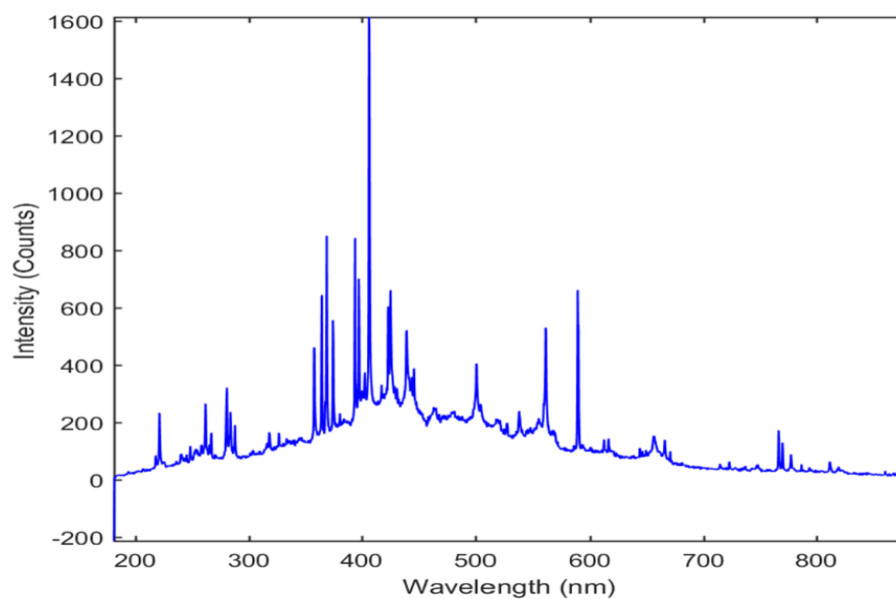


Figure B 7 Lead (Pb) spectrum (14-laser shot average).

Molybdenum

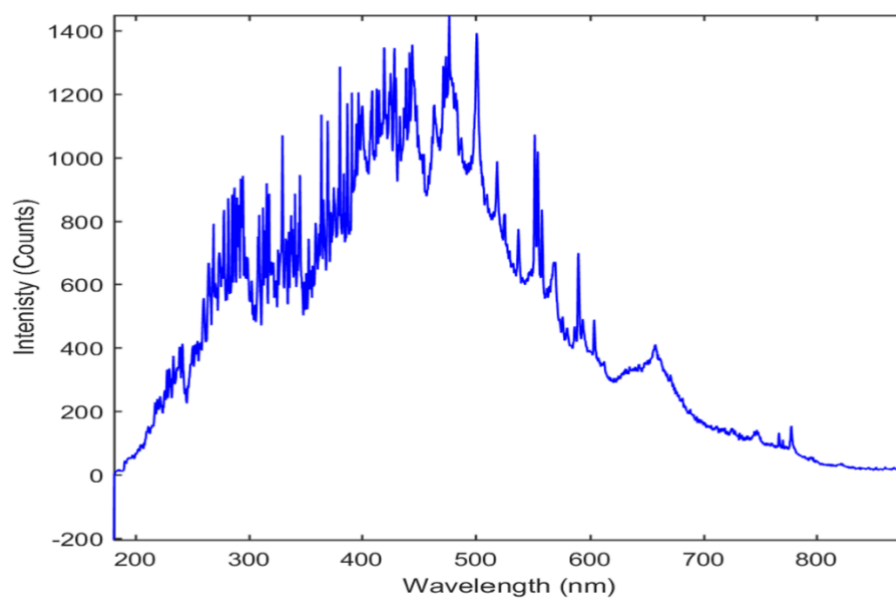


Figure B 8 Molybdenum (Mo) spectrum (14-laser shot average).

Silver (Ag)

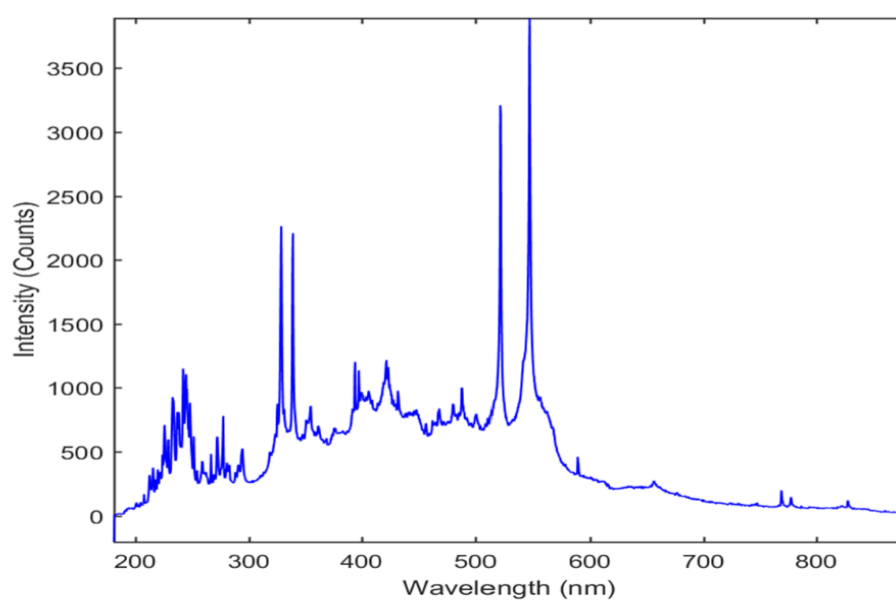


Figure B 9 Silver (Ag) spectrum (14-laser shot average).

Zinc (Zn)

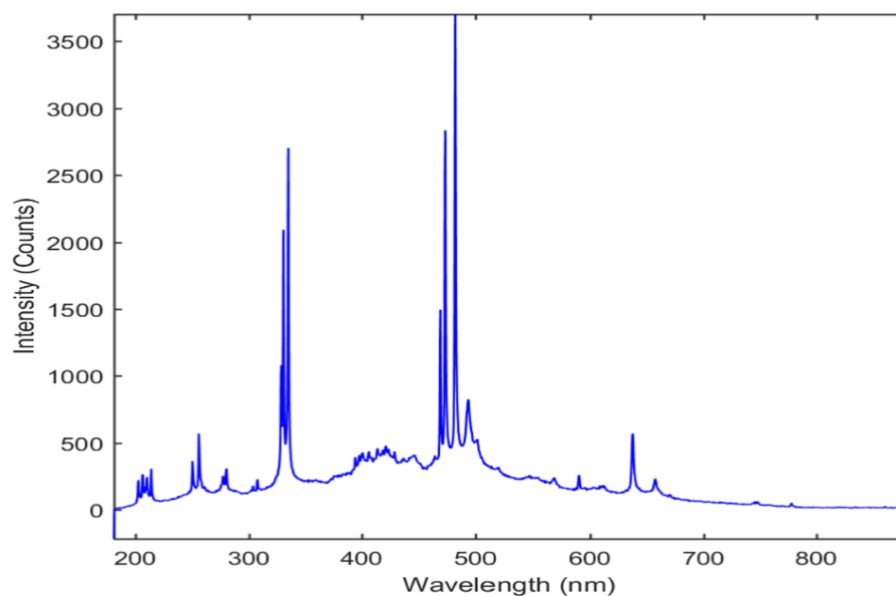


Figure B 10 Zinc (Zn) spectrum (14-laser shot average).

Tungsten (W)

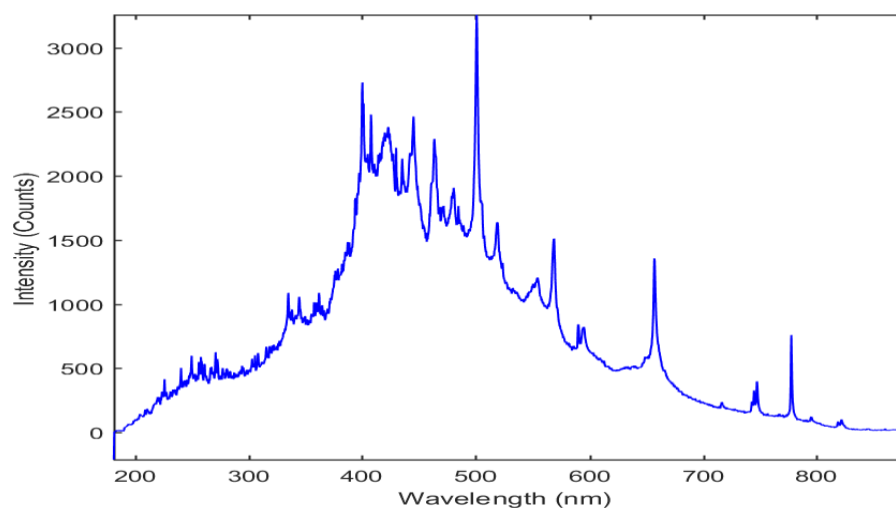


Figure B 11 Tungsten (W) spectrum (14-laser shot average).

The only point worth noting is the differences and similarities in the spectral distributions which will impact on the efficacy of the PCA classifier. Since the spectra are quite distinct one should expect PCA to work well in the current case.

B 5. Classification of Metals and Semiconductors using Multivariate Analysis.

There are various methods which are used for the multivariate analysis to statistically refine the data and to extract information which is not possible through conventional methods of analysing LIBS spectra. There include Principal Component Analysis, Partial Least Square Regression Method, Competitive Learning, etc [5]. In this preliminary study we have explored Principal Component Analysis for the classification of a range of known samples for making a reference for the identification of new samples. In metallurgy and the metal recycling industry there are many samples that are needed to be predicted (analysed) based, usually, on a small number of scrap material spectra.

B 5.1 Principal Component Analysis Applied to Scrap Metal Spectra

In the first set of experiments the PCA is used for the classification of different sets of spectral data obtained from different material samples figure B11 where Mo, Ag and Ta are analysed. This type of classification is useful in case of bulk materials analysis when there can be a large number of spectra generated at a high data rate. The idea is to place all relevant spectra from the NIST database into the PCA classifier and classify them based on clusters formed. Using the PCA classifier we can thus make a database of the known spectra and then we can classify the spectra of unknown materials which will match the cluster of known materials in the PCA space. Initially, 14 spectra obtained from each of three samples, namely Mo Ta and Ag, were studied using the measured spectra for each sample (figure B11) and then PCA was performed. The results are shown in figure B12.

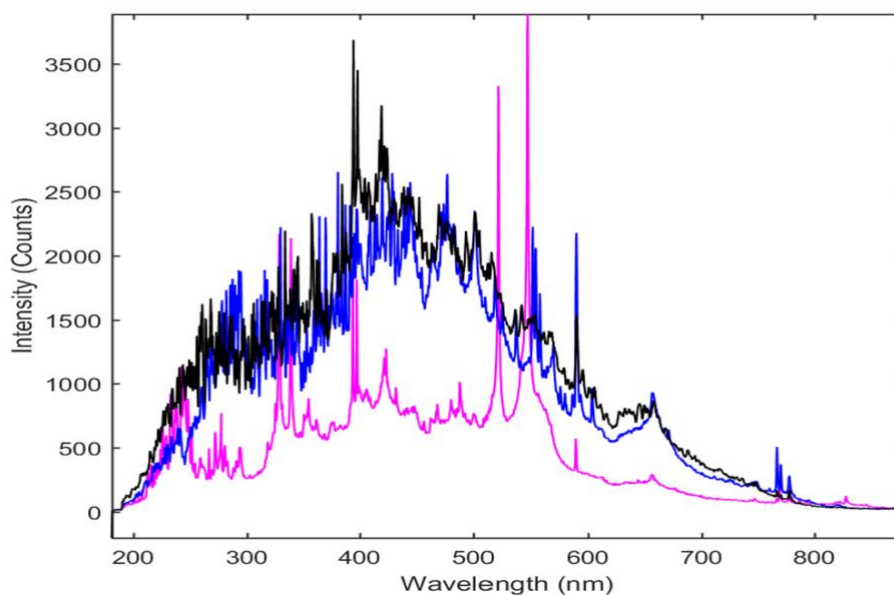


Figure B 12 UV-Vis-NIR spectra of Ag (magenta), Mo (blue) and Ta (black).

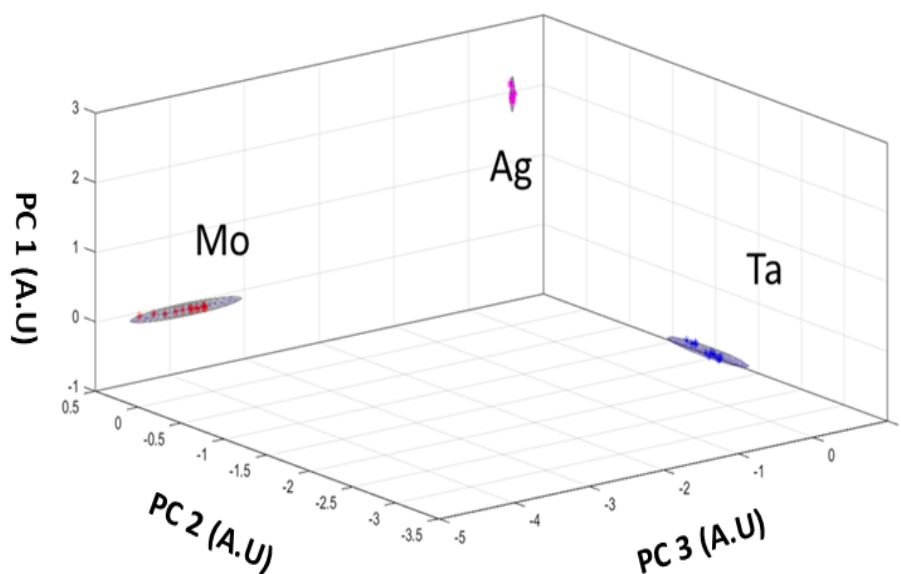


Figure B 13 Elements identified (classified) following PCA analysis.

As expected for scrap metal samples the three elements are well separated in the spectra for each of the three elements are closely packed leading to quite small and tight ellipsoids in the 3D principal component space. The ellipsoid boundary is set at 3 standard deviations from

the mean and so the tight ellipsoids indicate quite small variance. It is clear from the results above that the PCA classifier works well with the LIBS spectra for each metal sample.

In order to confirm this technique for a higher number of samples, 14 spectra for each of the 9 samples (a total of 126 spectra) were subjected to the PCA classifier. It is evident from figure B 14 that the different materials are quite well scattered in the three-dimensional principal component space. It is also clear that all spectra associated with a single material lie within its associated Gaussian ellipsoid boundary. This means of course within the limit of 3 times of standard deviation from the mean spectra of each sample, which shows that the spectra for each display quite small differences from each other (and good signal to noise ratio) but are sufficiently different between samples for PCA to work quite well.

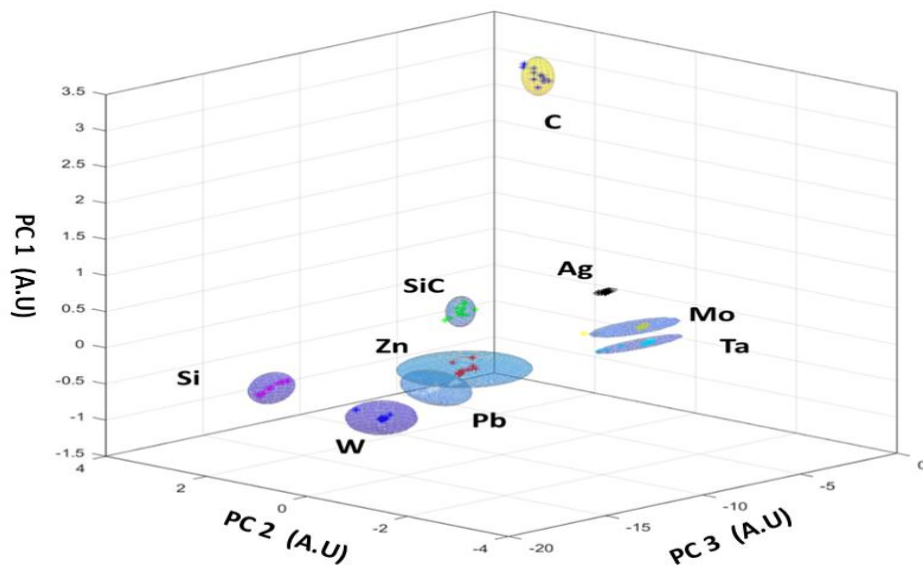


Figure B 14 All nine materials with 14 spectra each (126 spectra) were analysed using PCA. All the spectra are classified in clusters of every element with the ellipsoid of 3 times of standard deviation.

B.5.2 Principal Component Analysis for the Identification of Elements

This preliminary study focuses mainly on the application of LIBS coupled with PCA for the identification of silicon carbide using silicon and carbon as reference elements. For this study, 14 spectra of each of the samples of carbon, silicon and silicon carbide were used. At first, PCA of carbon(C) and silicon (Si) was performed by adding 28 spectra as shown in figure B15 and then PCA was performed 14 times, using a new spectrum of SiC each time. The Euclidean distance between pairs of materials, namely Si to C, Si to C and Si to SiC was calculated and is shown in table B3 below. Here, it is notable that this test was performed using a single silicon carbide spectrum every time. This was done in order to avoid a biased output resulting from the statistical impact of a larger number of silicon carbide spectra or all 14 spectra on the covariance matrix and on distance calculations.

Table B 3 Euclidean distance between the mean points of carbon, silicon and silicon carbide PCA in the three-dimensional space. PCA was performed 14 times using a different silicon carbide spectrum each time.

PCA	Distance Si-C	Si_SiC	C-SiC
1	9.76	11.11	3.12
2	9.76	11.11	3.12
3	9.76	11.09	3.14
4	9.76	11.11	3.11
5	9.76	11.11	3.12
6	9.76	11.10	3.13
7	9.76	11.11	3.10
8	9.76	11.12	3.10
9	9.76	11.11	3.11
10	9.76	11.12	3.11
11	9.76	11.11	3.12
12	9.76	11.13	3.09
13	9.76	11.09	3.14
14	9.76	11.10	3.12

Figure B16 shows the combined PCA for the 14 runs, which includes the PCA of 28 spectra of carbon and silicon (14 each) along with a cluster of 14 silicon carbide spectra which is done to show all the spectra combined on a single plot.

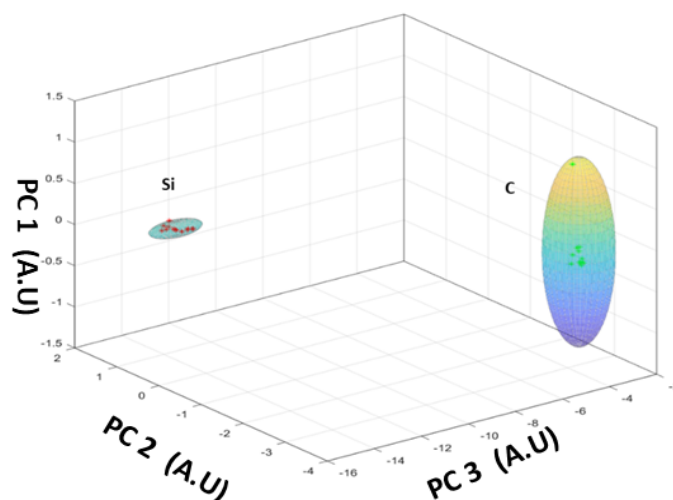


Figure B 15 PCA using 14 spectra of silicon (red) and 14 spectra of carbon (green). Each red dot and green dot represent the PCA score assigned to each spectrum.

It is evident from Table B3 that SiC is equidistant from the silicon and carbon. In this way it is clear that one would be able to identify the unknown sample (i.e., silicon carbide) by using the distance from the reference materials (like carbon and silicon). For example, from Table B3 the distance between C-SiC is ~ 3.1 whereas C-Si is ~ 9.76 and Si is ~ 11.1 .

The six different (scrap) metal samples were also subjected to PCA by combining their 84 spectra into a single dataset. The dataset was then divided into the subset of 60 spectra containing 10 training spectra of every sample and were used to train the PCA classifier while the remaining 24 (4 spectra of each sample) were used as the test spectra. PCA was performed individually for every element and it was observed that the test spectra lay quite well within the ellipsoidal classifier which means within the range of 3 times the standard deviation of the mean spectra of the particular sample. Figure B 17 shows the 3-dimensional

PCA for the training data (60 spectra), while figure B18 shows the combined PCA of all 6 samples.

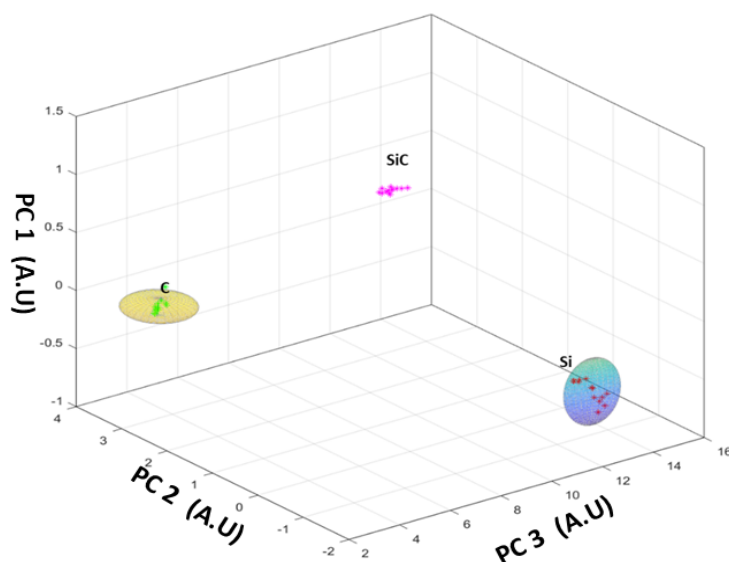


Figure B 16 PCA of C (green), Si (red) and cluster of SiC (magenta). The cluster of magenta points shows the 14 runs of SiC. The PCs of silicon carbide are ~ equidistant from the Si and C samples.

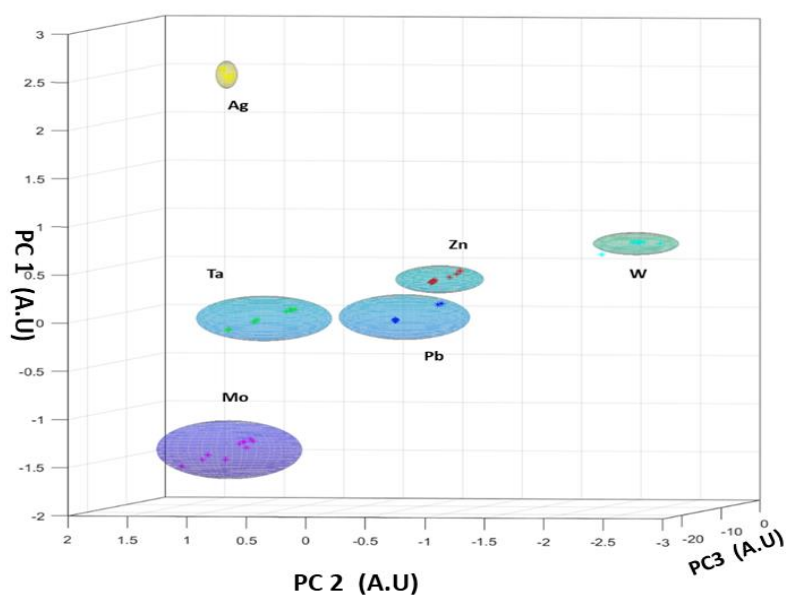


Figure B 17 3-dimensional PCA for metal samples Ag (yellow), Ta (green), Mo (magenta), Pb (blue), Zn (red) and W (cyan). Different colours show the PCA score for each spectrum.

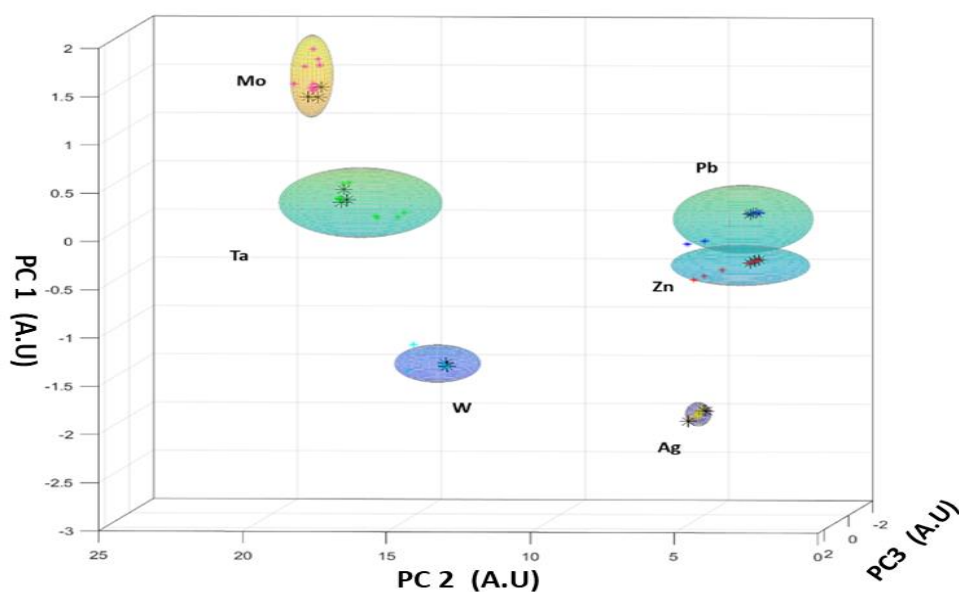


Figure B 18 3-dimensional PCA of metal samples Ag (yellow), Ta (green), Mo (magenta), Pb (blue), Zn (red) and W (cyan). The black * on each ellipsoid represents the test sample of the respective sample.

In order to validate the results every test sample was analysed individually to verify if all the test spectra lay within the ellipsoidal classifier for that same sample. Results show that PCA can be used for the identification of unknown spectra of scrap metals.

Summary

Multivariate analysis is a useful technique to analyse LIBS spectra and it is likely that it can be successfully used to classify and identify different elements expected to be found in scrap metals. PCA was used in this research to analyse the LIBS spectra for nine different samples comprising metals and semiconductors. Three studies were performed. For the first study, a PCA classifier was used for the classification of nine samples. In the second study the Euclidean distance between C and Si to SiC was determined which confirms that every spectra of the single spectrum of SiC was equidistant from the C and Si. Therefore, on the basis of these distances we can identify the unknown samples. For third study, six different scrap metal samples were used. The application of PCA confirmed that each sample could be well

distinguished from any other as evidenced by the fact that the corresponding ellipsoids did not exhibit any overlapping.

References:

- [1] Clegg S.M, Sklute E, Dyar M. D, Barefield J.E, Wiens R. C. 2009. Spectrochim. Acta - Part B At. Spectrosc. **64** pp 79-88.
- [2] Pořízka P, Klus J, Hrdlička A, Vrábel J, Škarková P, Prochazka D, Novotný J, Novotný K, Kaiser J. 2017. J. Anal. At. Spectrom. **32** pp 277-288.
- [3] Awasthi S, Kumar R, Rai G.K, Rai A.K. 2016. Opt. and Las. Eng. **79**, pp 29-38.
- [4] Pořízka P, Klus J, Képeš E, Prochazka D, Hahn D.W, Kaiser J. 2018. Spectrochim. Acta - Part B At. Spectrosc. **148** pp 65-82.
- [5] Pořízka P, Klus J, Mašek J, Rajnoha M, Prochazka D, Modlitbová P, Novotný J, Burget R, Novotný K, Kaiser J. 2017. Sci. Rep pp **7** pp 1-2.

Appendix C

List of Publications and Research Outputs

Manuscripts under preparation

Syedah Sadaf Zehra, Piergiorgio Nicolosi, Paddy Hayden, John Costello, “Line plasma studies for the optimization of parameters for detection of carbon in steel using vacuum ultraviolet laser induced breakdown spectroscopy”.

Syedah Sadaf Zehra, Piergiorgio Nicolosi, John Costello, Paddy Hayden, “ Time resolved VUV LIBS for the detection of light elements in metals: Limit of detection optimization”.

Syedah Sadaf Zehra, Muhammad Bilal Alli, Piergiorgio Nicolosi, John Costello, Paddy Hayden, “Multivariate data analysis of the LIBS spectra for the classification of semiconductors and scrap metals from the waste materials”

Published

Syedah Sadaf Zehra John T. Costello, Piergiorgio Nicolosi, Patrick Hayden “Aluminium Thin Films Depth Profiling Using Laser Induced Breakdown Spectroscopy” Journal of Physics: Conference Series 1289, 012043 (2019)

Syedah Sadaf Zehra, John T. Costello, Piergiorgio Nicolosi, Patrick Hayden “Time-integrated and time-resolved VUV LIBS: a comparative study” SPIE Proceedings, Volume 10674, Quantum Technologies 2018; 106741H (2018)

Zuppella, Paola, Vania Da Deppo, **Syedah Sadaf Zehra**, Paolo Chioetto, Alessandra Slemer, Massimo Fedel, Piergiorgio Nicolosi et al. "FLY-spec prototype: UV-VIS-NIR reflectometry and laser-induced breakdown spectroscopy (Conference Presentation)." In Fiber Lasers and Glass Photonics: Materials through Applications II, vol. 11357, p. 1135719. International Society for Optics and Photonics, 2020.

Abstracts Communications and Poster presentations

S. S. Zehra, John Costello, Piergiorgio Nicolosi, Patrick Hayden, The 9th International Conference on Laser-Induced Breakdown Spectroscopy LIBS 2016, Chamonix, France, 7th – 12th September. 2016 (**Abstract**)

S. S. Zehra, John Costello, Piergiorgio Nicolosi, Patrick Hayden, EXTATIC 2015 Welcome Week Workshop, Southampton, United Kingdom, 7th - 17th January. 2016 (**Oral presentation**)

S. S. Zehra, John Costello, Piergiorgio Nicolosi, Patrick Hayden, EXTATIC 2016 Welcome Week Workshop, Trieste, Italy, 17th - 23rd January, 2017 **(Oral presentation)**

S. S. Zehra, John Costello, Piergiorgio Nicolosi, Patrick Hayden, EXTATIC 2017 Welcome Week Workshop, Prague, Czech Republic, 22nd -24th September 2017 **(Oral presentation)**

S. S. Zehra, John Costello, Piergiorgio Nicolosi, Patrick Hayden, 9th Euro-Mediterranean Symposium on LIBS and Colloquium Spectroscopicum Internationale XL, EMS LIBS 2017, 11th June - 16th June 2017, Pisa, Italy **(Oral presentation)**

S. S. Zehra, John Costello, Piergiorgio Nicolosi, Patrick Hayden, SPIE Photonics Europe 2018, 22-26 April 2018, Strasbourg France. **(Poster presentation)**

S. S. Zehra, John Costello, Piergiorgio Nicolosi, Patrick Hayden, International Conference on Spectral Line Shapes 2018, June 17 - 22, 2018, Dublin, Ireland **(Poster Presentation)**